

STRUCTURES AND REACTIVITY OF TRANSITION-METAL COMPOUNDS
FEATURING METAL-LIGAND MULTIPLE BONDS

A Dissertation

by

ZHENGANG XU

Submitted to the Office of Graduate and Professional Studies of
Texas A&M University
in partial fulfillment of the requirements for the degree of

DOCTOR OF PHILOSOPHY

Chair of Committee,	Michael B. Hall
Committee Members,	Roland E. Allen
	Robert R. Lucchese
	Simon W. North
Head of Department,	David H. Russell

August 2014

Major Subject: Chemistry

Copyright 2014 Zhenggang Xu

ABSTRACT

This dissertation presents the results from density functional theory (DFT) calculations on three major projects I have been working on over the past several years. The first system is focused on the structure and reactivity of a novel osmium silylyne compounds featuring an Os≡Si triple bond. NMR simulation confirmed the existence of this compounds and bonding analysis like NBO and ETS-NOCV proved its triple bond character. The structures of the [2+2] cyclo-addition product from silylyne and other small molecules (PhC≡CPh and P≡C^tBu) were also determined from possible isomers by energetic results and NMR simulations. The cycloaddition reactions were found to be under kinetic control and steric effects should be a major reason for that. Furthermore, the geometric and electronic structures of the osmium silylyne analogues (M≡E, M = Ru and Os; E = Si, Ge and Sn) are studied computationally and their similarities and distinctions are discussed.

Both the second and third systems are related to the formation of transition metal imido compound (M=NR). In the second system a cationic oxorhenium(V) complex reacts with a series of arylazides (N₃Ar) to give cationic *cis*-rhenium(VII) oxo imido complexes. Inductive effect is found in the reaction rates but it leads to different trends for electron-donating and electron-withdrawing substituted phenyl azides. Computations found all the substituted phenyl imido products are formed through the same pathway. The reason for the different trend is due to the competitions between two major energy barriers along the reaction pathway. For the electron-withdrawing substituents, N₂

extrusion is rate determining, while for the electron-donating substituents, the rate-determining step becomes the initial attack of the azide. The barriers for these two steps are inverted in their order with respect to the Hammett σ values; thus, the Hammett plot appears with a break in slope.

In the third system a series of vanadium (III) terminal organoazides were converted to vanadium (V) imido compounds and small quantities of diazenes were found formed in the reactions. Computational studies were conducted to examine several possible pathways and a mechanism in which nitrene radicals released from metal-azide decompositions is supported based on two reasons: 1) The two-electron reduction on vanadium center during decomposition of azide generates two fragments both in their ground states (triplet states), which might drag the activation barrier down; 2) This conversion is spin-allowed since vanadium center and nitrene nitrogen are antiferromagnetically coupled in transition state. The ligand simplification study indicates that the bulky mesityl groups on the supporting ligand prevents the reactions from going through the direct N_2 extrusion pathway.

DEDICATION

I dedicate this dissertation to my beloved and ever-supportive parents.

ACKNOWLEDGEMENTS

I am most grateful to my advisor Dr. Michael B. Hall, who guided me along from the first day I started at Texas A&M University to today. Over the past several years he was always willing to discuss any ideas I have in mind; he answered every single question with great patience; he showed me how to be a real scientist with genuine curiosity; he respected every decision I made about my life... I enjoy working with him and learning from him. I will benefit from this experience throughout my whole life.

I also would like to thank my committee members. Dr. Robert R. Lucchese taught me quantum mechanics and Dr. Simon W. North taught me chemical kinetics. Both courses were the foundations on which I could better understand and appreciate the literatures and the computational tools I used in my research. Although I was not in Dr. Roland H. Allen's statistical mechanics class, I was impressed by his passion in running. I am looking forward to being in the same race with him again, and I hope I can be as energetic as him throughout my entire life.

I owe a special thanks to Dr. Lisa Perez, who was always around to facilitate my research with professional and instant support. I am sure the academic life will be a lot tougher without the help from her.

I also feel lucky to have Monica Gonzales as our administrative secretary. She made all the sophisticated paperwork so simple that I have never had any trouble on those issues.

I am greatly indebted to all the group members with whom I shared a great time: Amanda, Jason, Xinzheng, Caiping, Justin, Ivica, Eszter, Li, Ana, Scott, Stella, Jia, Haixia, Shengda, Sonia, Lukasz and Qian. They are so kind and always willing to help, and I wish every one of them has a wonderful life and career in the future.

I also owe a special thanks to my roommates and the good friends I met in College Station. You made the past five years so enjoyable that I cannot believe I will be leaving so soon. I will always treasure the days we shared together, and I send my best wishes along with you.

At last, I would like to thank one more person. You are the reason I strive.

TABLE OF CONTENTS

	Page
ABSTRACT	ii
DEDICATION	iv
ACKNOWLEDGEMENTS	v
TABLE OF CONTENTS	vii
LIST OF FIGURES	ix
LIST OF TABLES	xiv
CHAPTER I INTRODUCTION	1
1.1 Why transition metal complexes?	1
1.2 Early understanding of transition metal complex and Werner's contributions	2
1.3 How do we understand the nature of transition metal compounds?	3
1.4 Back donation from metal center to the ligand	8
1.5 Multiple bonds between transition metal and ligand: carbene	10
1.6 More on metal ligand multiple bonds	17
CHAPTER II THEORETICAL BACKGROUND	21
2.1 Quantum mechanics and the Schrödinger equation	21
2.2 Born-Oppenheimer approximation	23
2.3 The Hartree-Fock approximation	24
2.4 Basis set approximation	29
2.5 Electron correlation	31
2.6 Density functional theory	33
2.7 Wavefunction analysis	40
CHAPTER III STRUCTURE AND REACTIVITY OF AN OSMIUM SILYLYNE COMPOUND	43
3.1 Introduction	43
3.2 Experimental observations	45
3.3 Computational details	47
3.4 Computational results and discussion	48
3.5 Conclusion	73

CHAPTER IV COMPUTATIONAL PREDICTION OF INDUCTIVE EFFECTS THAT CAUSE A CHANGE IN THE RATE-DETERMINING STEP FOR THE CONVERSION OF RHENIUM AZIDES TO IMIDO COMPLEXES	75
4.1 Introduction	75
4.2 Experimental observations	80
4.3 Computational details.....	82
4.4 Computational results and discussion	84
4.5 Conclusion.....	98
CHAPTER V A NITRENE-RELEASE MECHANISM IN CONVERSION FROM VANADIUM ORGANOAZIDE COMPLEXES TO TERMINAL VANADIUM IMIDES	100
5.1 Introduction	100
5.2 Summary of experimental observations	103
5.3 Computational details.....	104
5.4 Results and discussion.....	105
5.5 Conclusion.....	127
CHAPTER VI CONCLUSION.....	128
REFERENCES.....	131

LIST OF FIGURES

	Page
Figure 1. The proposed structures for transition metal complex $\text{CoCl}_3(\text{NH}_3)_4$. (a). The chain structure suggested by Jørgensen. (b) and (c). The <i>trans</i> and <i>cis</i> isomer of $[\text{Co}(\text{NH}_3)_4\text{Cl}_2]^+$ ion proposed by Werner, respectively.	2
Figure 2. The VB description of the bonding orbitals of $[\text{Co}(\text{NH}_3)_6]^{3+}$ ion. The empty valence orbitals on Co^{3+} cation are mixed first to form the d^2sp^3 hybridized orbitals. Then the lone pair electrons on nitrogen atoms from the six NH_3 ligands were donated to the empty hybridized orbitals to make the complex ion $[\text{Co}(\text{NH}_3)_6]^{3+}$	4
Figure 3. The MO diagram of the cation $[\text{Co}(\text{NH}_3)_6]^{3+}$ with O_h symmetry.	7
Figure 4. The illustration of back-donation in metal carbonyl and side-on metal ethylene complexes. The arrows indicate the directions of electron flow in bond making.	9
Figure 5. The electron occupations in singlet carbene and triplet carbene.	10
Figure 6. (a) The bonding pattern of Fischer carbenes. (b) The resonance structure of a Fischer carbene. (c) An example of Fischer carbene. (d) The bonding pattern of Schrock carbenes. (e) An example of Schrock carbene.	11
Figure 7. MO diagram of Fischer carbene and Schrock carbene. In Schrock carbene, the metal center does not tend to hold the electrons. So the two electrons are transferred to the carbene. The two electrons from metal center are colored red in the figure.	14
Figure 8. (a) An example of olefin metathesis reactions. (b) A brief mechanism of the olefin metathesis reaction shown in (a). The general schemes of several important types of olefin metathesis reactions: (c) ring opening metathesis polymerization (ROMP); (d) ring opening metathesis (ROM) and ring closing metathesis (RCM) and (e) cross metathesis (CM).	15
Figure 9. The structures of the 2 nd generation Grubbs catalyst and the Schrock catalyst.	16
Figure 10. Qualitative molecular orbitals of the <i>d</i> -block of a d^0 metal-oxo compound with octahedral structure.	18
Figure 11. The comparison of Slater function and Gaussian function.	30

Figure 12. The MO diagram of H ₂ molecule.	33
Figure 13. DFT optimized structure of 2 . All the hydrogen atoms are hidden except the hydride on the Os atom.	50
Figure 14. Some selected osmium complexes (1 - e) having the same Cp [*] (iPr ₃ P)Os ⁺ fragment as 2 . 1 , a and b have Os=Si double bonds while c , d and e have Os-Si single bonds.	51
Figure 15. Experimental and computed chemical shift of Si atom in compounds 1 and a ~ e (shown in Figure 14). An excellent linear correlation is found between these chemical shifts for the silicon atoms, which suggests that the calculated silicon chemical shift of 2 , 3 and 4 could be corrected by this trend line to reduce the systematic error in the calculations.	54
Figure 16. Three bonding interactions in compound 2 described by natural bond orbital analysis. <i>1π</i> and <i>2π</i> are back donations from filled osmium <i>d</i> orbitals to empty silicon <i>p</i> orbitals.	56
Figure 17. Three NOCV orbitals contributing the majority of the orbital interaction energies. <i>Nocv1</i> is a clean in-plane <i>π</i> bond, while <i>nocv2</i> and <i>nocv3</i> are mixtures of the <i>σ</i> bond and the out-of-plane <i>π</i> bond.	57
Figure 18. Structural illustrations of the [2+2] cycloaddition products. 3a and 3b , 4a and 4b are two pairs of product isomers. The isomers labeled “a” (3a or 4a), have their C≡C or P≡C fragments connected to the Os≡Si bond from above the <i>trip</i> ring’s plane. Due to steric repulsions, this ring was forced to rotate and bend to a certain extent. Similarly, in isomers labeled “b”, this ring was forced to rotate in the opposite direction since the C≡C or P≡C fragments approached the Os≡Si bond from below the <i>trip</i> ring’s plane. As a consequence the four-member rings formed in the [2+2] cycloaddition are bent in opposite directions in isomers labeled “a” and “b”. All the species shown here are cations with one positive charge. Counter-ions are neglected in the computations, but solvation corrections are reported.	59
Figure 19. Optimized structure of 3a , 3b , 4a and 4b . Important bond lengths (Å) and bond angles (°): 3a) Os-Si: 2.347, Os-C1: 2.248, C1-C2: 1.403, Si-C2: 1.817, Si-C1: 2.126, Os-Si-C3: 140.3; 3b) Os-Si: 2.331 Os-C1: 2.203, C1-C2: 1.412, Si-C2: 1.802, Si-C1: 2.191, Os-Si-C3: 138.6; 4a) Os-Si: 2.390, Os-P1: 2.466, C1-P1: 1.744, Si-C1: 1.844, Si-P1: 2.427, Os-Si-C2: 131.4; 4b) Os-Si: 2.359, Os-P1: 2.426, C1-P1: 1.739, Si-C1: 1.828, Si-P1: 2.498, Os-Si-C2: 132.1.	60
Figure 20. The projection formulas of structures of compound 2 and all the possible isomers of [2+2] cycloaddition products in question. As shown in the	

rectangular box, in such formulas, all the important atoms and functional groups are projected onto a plane parallel to the Cp* rings and the Cp* ring is hidden for a clearer view. Since isomers labeled “a” or “b” (these differences have been illustrated in Figure 18 and described in the text) share the same projection formulas, each projection formula in Figure 20 actually represent two isomers. Two additional types of isomers are illustrated here: 1) whether the PhC-CPh or P-C^tBu fragments are *trans* or *cis* relative to the hydride position (*e.g.* 3a vs 3a_*cis*); 2) Furthermore, two bonding patterns are possible for the P≡C bond’s cycloaddition reaction (Os bonding to P or C, *e.g.* 4a vs 4a_*rev*). It will be easily recognized from the figure that compound 3 and 4 have 4 and 8 isomers, respectively.61

- Figure 21. The Gibbs free energy profile of the [2+2] cycloaddition reaction of 2. Dispersion and solvation correction are included here. 3a and 4a are the kinetic products and 3b and 4b are the thermodynamic products.65
- Figure 22. The optimized structure of critical transition states. Some additional geometric parameters: ts1_3a) Os-C1: 4.288, Os-C2: 4.709, C1-C2: 1.236, Os-Si-C3: 148.3; ts1_3b) Os-C1: 4.235, Os-C2: 4.929, C1-C2: 1.243, Os-Si-C3: 141.1; ts2_3a) Os-C1: 3.601, Os-C2: 3.952, C1-C2: 1.291, Os-Si-C3: 138.3; ts2_3b) Os-C1: 3.622, Os-C2: 4.148, C1-C2: 1.287, Os-Si-C3: 131.9; ts_4a) Os-P1: 3.710, Os-C1: 4.293, C1-P: 1.604, Os-Si-C2: 144.4; ts_4b) Os-P1: 3.783, Os-C1: 4.435, C1-P: 1.610, Os-Si-C2: 136.8.66
- Figure 23. Full models and simplified structures for the 4a and 4b.67
- Figure 24. NOCV orbitals of osmium germylyne compound.73
- Figure 25. Resonance forms of phenyl azide.76
- Figure 26. Coordination modes of organic azides. (a) terminal azide nitrogen (N_γ) complexation, (b) coordination through N_α, (c) η²-adduct analogue of olefin complexation, (d) diazenimido, and (e) bridging μ-imido ligation.78
- Figure 27. Formation of Re(VII) oxo imido complexes. A series of substituted Ar groups (a ~ f) are involved in the reactions.79
- Figure 28. Hammett plot for aryl azides with different substituents. Reaction rates of rhenium imido compounds show linear relationship on the σ value of electron-withdrawing substituents. Reactions involving azides with electron-donating substituents deviate significantly from this trend. Key: ■ *p*-MeO, ● *p*-Me, ▲ H, □ *m*-MeO, ○ *p*-Cl, and Δ *p*-CF₃.81
- Figure 29. The potential energy surface scanning of the Re-N bond length elongated from the intermediate for different substituted azides.83

Figure 30. The crystal structure (left) and computational optimized structure (right) of 2a with H atoms omitted.	84
Figure 31. α - and γ - intermediates of rhenium azide compounds.	87
Figure 32. Structures and some selected bonds lengths of 1_ <i>trans</i> (left) and 1_ <i>cis</i> (right). The ligands lying in the equatorial plane are relatively flat in 1_ <i>trans</i> , while fairly twisted in 1_ <i>cis</i>	88
Figure 33. Different isomers of product 2a-f.	89
Figure 34. The rearrangement between 2_ <i>iso6</i> and 2_ <i>iso3</i>	92
Figure 35. The solvated ΔG (kcal/mol) diagram for the reaction of Rhenium oxo complex with ArN ₃ . (solvent: CH ₃ CN)	94
Figure 36. The computed Hammett plot shows fairly good agreement with experimental plot. Key: ■ <i>p</i> -OMe, ● <i>p</i> -Me, ▲ H, □ <i>m</i> -OMe, ○ <i>p</i> -Cl, and Δ <i>p</i> -CF ₃	97
Figure 37. Qualitative view of the electronic configuration of the triplet nitrene and singlet nitrene.	101
Figure 38. A summary of transformation of nitrene radicals.	102
Figure 39. Synthetic scheme of vanadium azide compounds and vanadium imido compounds.	103
Figure 40. The optimized structures of 2a_ <i>sing</i> (left) and 2a_ <i>trip</i> (right).	106
Figure 41. Natural bonding orbitals of 2a_ <i>singlet</i> clearly show one V-N σ bond and two V-N π bond.	108
Figure 42. The formation of 2a_ <i>sing</i>	110
Figure 43. Potential energy surface scan during the formation of 2a.	110
Figure 44. Potential energy surface of free azide decomposition.	113
Figure 45. Possible pathways of conversions from metal azide to metal imide.	114
Figure 46. The computed energetic data of PATH1. The energies shown in the figure are in the format of ΔE_{elec} / ΔG_{gas} / ΔG_{sol} and the values are in kcal/mol.	116
Figure 47. Structures of 2a and corresponding transition states ts_2a in both open-shell singlet and triplet states.	117

Figure 48. The spin density of direct dissociation transition states of 2a_sing (left) and 2a_trip (right).	118
Figure 49. Computed Hammett plot for thermolysis of the vanadium azide compounds, $(\text{tpa}^{\text{Mes}})\text{V}[\eta^1\text{-N}_3(p\text{-C}_6\text{H}_4\text{R})]$. R= ■ $\text{N}(\text{CH}_3)_2$ (2d); ◆ OCH_3 (2a); ● CH_3 (2c); ▲ H (2b).	120
Figure 50. The optimized structure of 4a and the decomposition transition state ts_4a.	122
Figure 51. Energetics of the dissociation of 4a. The energies shown in the figure is in the format of $\Delta E_{elec} / \Delta E_{gas} / \Delta E_{sol}$ relative to 2a_sing and the values are in kcal/mol.	122
Figure 52. The optimized structures/energetics of 5a and ts_5a and the Mulliken spin density of this open-shell transition state. Energies are in kcal/mol relative to 2a_sing.	123

LIST OF TABLES

	Page
Table 1. Selected bond lengths (Å), bond angle (°) and solvated free energies (kcal/mol).....	49
Table 2. The optimized bond lengths for the Os–Si bonds in several osmium species. ...	51
Table 3. Silicon chemical shift values in 1 calculated by different functionals and basis sets.	53
Table 4. NBO analysis of the Os-Si π bond in compound 2	56
Table 5. ETS-NOCV results for compound 2	57
Table 6. ^{29}Si and ^{31}P chemical shift values (ppm) for different isomers of 2 , 3 and 4	58
Table 7. Energetic data for all isomers of cycloaddition products ^a	62
Table 8. Gas phase electronic energies of full model and simplified model for 4	68
Table 9. EDA analysis on the isomers of transition states and the final products of 4	70
Table 10. Computed M≡E bond lengths.....	71
Table 11. ETS-NOCV analysis of M≡E triple bonds (M = Os and Ru, E = Si, Ge, Sn).....	72
Table 12. The gas phase free energy differences between double bond species (M=EH) and their triple bond isomers (HM≡E). ($\Delta\Delta G = \Delta G(\text{M=EH}) - \Delta G(\text{HM}\equiv\text{E})$).	73
Table 13. Comparison between crystal structure and computed structure for selected bond lengths (Å) and angles (degree) for 2a	85
Table 14. Selected structural data of 2a obtained from X-ray and computed by different functionals.	86
Table 15. Reaction energies for different isomers of 2c relative to 1_{trans} + PhN ₃ (kcal/mol).....	90
Table 16. Comparisons of energy between iso3 and iso6 for 2a-f (kcal/mol).	91
Table 17. Results of energies differences ^a between 2c_{iso6} and 2c_{iso3}	92

Table 18. Selected structural parameters of 2a from computations and experiments. (Bond length in Å, bond angle in degree.).....	107
Table 19. Comparisons of energetics, critical geometric parameters and S^2 values among 2a_sing, 2a_trip and the MECP.	111
Table 20. Important parameters of MECP and singlet transition state during the free azide decomposition process.	113
Table 21. Comparison of electronic energies (kcal/mol) between full model and simplified model of some critical species in the proposed mechanism.	126
Table 22. Single point energies (kcal/mol) calculated for some critical species with and without dispersion corrections.	126

CHAPTER I

INTRODUCTION

This chapter provides a very broad overview of our understanding of the geometric and electronic structures of transition metal compounds via valence bond (VB) and molecular orbital (MO) languages. Structures and reactivity of compounds featuring transition metal-ligand multiple bonds, especially metal carbene complexes are discussed. Each chapter will review the specific background for the systems studied therein.

1.1 Why transition metal complexes?

Coordination compounds containing transition metal centers have evoked a range of interest from fundamental research to industrial applications.¹ There are many reasons why these compounds are so fascinating. Firstly, transition metal compounds have complicated geometric and electronic structures, which have led to numerous novel synthetic methods and theories to interpret their spectra (eg. crystal and ligand field theories (CF and LF), valence bond theory (VB), molecular orbital theory (MO), *etc.*). Secondly, in catalytic processes, both synthetic and biological, unsaturated metal centers not only bring substrates into close proximity, but also tune their electronic structures to reduce the reaction barrier. Thirdly, the structures of the transition metal catalysts sometimes control the structures of the major products, enabling unsymmetrical synthesis of many compounds with excellent selectivity. Based on these merits, the

structures and reactivity of transition metal compounds have attracted extensive research interests in the past century.

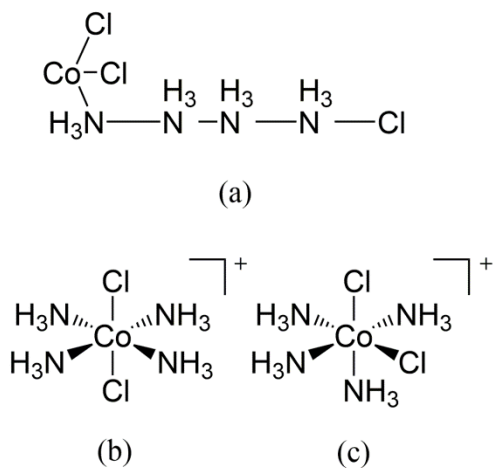


Figure 1. The proposed structures for transition metal complex $\text{CoCl}_3(\text{NH}_3)_4$. (a). The chain structure suggested by Jørgensen. (b) and (c). The *trans* and *cis* isomer of $[\text{Co}(\text{NH}_3)_4\text{Cl}_2]^+$ ion proposed by Werner, respectively.

1.2 Early understanding of transition metal complex and Werner's contributions

Actually, transition metal complexes were known from the beginning of chemistry, but their nature was barely understood until the first correct structural description was given by Alfred Werner in 1893.² At that time cobalt was known to form a compound in composition of $\text{CoCl}_3(\text{NH}_3)_4$. The widely accepted interpretation of its structure at that time was Jørgensen's chain theory, in which the ligands were bound to one another in $-\text{NH}_3-$ chains (**Figure 1(a)**). Werner proposed this compound was made up by a complicated cation $[\text{Co}(\text{NH}_3)_4\text{Cl}_2]^+$ and a Cl^- anion; in $[\text{Co}(\text{NH}_3)_4\text{Cl}_2]^+$ the Co^{3+}

cation was surrounded by two Cl^- anions and four NH_3 molecules at the vertices of octahedron. This model successfully explained the two different isomers of $[\text{Co}(\text{NH}_3)_4\text{Cl}_2]\text{Cl}$: the green isomer had two Cl^- anions opposite to each other (*trans* isomer, **Figure 1(b)**) while the blue isomer had two Cl^- at adjacent positions (*cis* isomer, **Figure 1(c)**). In addition to the proposal of novel structures now known as Werner compounds, Werner also developed new concepts like primary and secondary valence, which correspond to oxidation state and coordination number, respectively, in modern terminology. Werner's theory not only set the foundation of coordination chemistry, but also earned him the Noble prize in Chemistry in 1913.

1.3 How do we understand the nature of transition metal compounds?

In modern chemistry, a typical transition metal complex contains one or more metal centers binding several ligands (molecules or ions) in a certain spatial arrangement. Two most popular models, valence bond (VB) theory³ and molecular orbital (MO) theory,⁴ can be used to describe the electronic structures of transition metal compounds. In the VB model, the bonding between metal center and ligands can be viewed as Lewis acid-base interaction. The ligands (serve as Lewis base) donate their lone pair electrons to the empty orbitals on the metal atom (serve as Lewis acid) and this donor-acceptor interaction is known as dative bond or coordinate bond, a special case of covalent bond. Furthermore, the empty *d* orbitals on the metal were incorporated in the orbital hybridization. For example, in $\text{Co}(\text{NH}_3)_6^{3+}$ ion, six empty valence orbitals on the Co^{3+} center (two *3d* orbitals, one *4s* and three *4p* orbitals) are mixed to form the d^2sp^3 hybridization (**Figure 2**). These 6 equivalent hybrid orbitals point to the vertices of an

The qualitative MO diagram of $[\text{Co}(\text{NH}_3)_6]^{3+}$ (**Figure 3**) is used to illustrate some important concepts of the MO approach. In general, we only need to consider MO's constructed by the valence orbitals of each atom because the inner or core orbitals are seldom involved in chemical reactions. In this complex, the $3d$, $4s$ and $4p$ orbitals on the metal center and the σ donor orbitals on the six ligands on the ligands are used to construct the MO's, and they are drawn on the left and right hand side of the MO diagram, respectively.

If there are no ligands around the metal ion, the five $3d$ orbitals are degenerate, as are the three $4p$ orbitals. If there are ligands, the ligand orbitals will mix with the central-metal orbitals to generate bonding, non-bonding and anti-bonding orbitals. As a result, the orbital energies of metal get changed and the degeneracy of orbitals is broken according to the specific spatial arrangement of ligands. If the ligands are arranged in a special symmetry, the σ donor orbitals can be linearly combined into group orbitals according to this specific symmetry, which is known as symmetry adapted linear combination (SALC) of orbitals. This operation has great merit in simplifying the molecular orbitals and reducing the computation cost. The six NH_3 ligands stay in the vertices of an octahedron, so $[\text{Co}(\text{NH}_3)_6]^{3+}$ belongs to O_h point group. As a result, the σ donor orbitals on the six ligands can be combined into three sets of group orbitals which have a_{1g} , e_g and t_{1u} symmetry, respectively. Under the influence of the O_h symmetry, the five $3d$ orbitals on Co^{3+} split into two sets of orbitals which have e_g and t_{2g} symmetry, and the $4s$ and $4p$ are assigned a_{1g} and t_{1u} symmetry. The constructed MOs of $[\text{Co}(\text{NH}_3)_6]^{3+}$ are shown in **Figure 3**, six bonding and six anti-bonding orbitals are formed with appropriate

symmetry. The three $3d$ orbitals with t_{2g} symmetry have no match with the ligand orbitals, so it become the non-bonding orbital in the final set of MO.

After the MOs are constructed, the electrons from metal center and the ligand donor orbitals fill the lowest ones. The t_{2g} non-bonding orbitals are the highest occupied molecular orbitals (HOMO) while the e_g anti-bonding orbitals (e_g^*) are the lowest unoccupied molecular orbitals (LUMO). If more electrons are added into this system, they will be placed on the e_g^* orbitals, which will weaken the stabilization brought by filled bonding orbital e_g and ultimately cause dissociation of the ligands. So for a transition metal complex with O_h symmetry, the bonding and non-bonding orbitals can at most accommodate 18 electrons, which is known as the 18 electron rule. For compounds with different geometry, different rules may be applied (16 electron rule for some square-planar compounds). However, the key idea always holds: placing electrons in anti-bonding orbitals are not energetically favorable.

Many properties can be rationalized in the framework of MO: an electron moving from an occupied MO to an unoccupied MO gives rise to excited states. So the spectra of transition metal complexes can be interpreted by electron transitions between these different orbitals. If some orbitals are singly occupied and the total spin is not zero, the compound will be paramagnetic. The distorted structures of some d^9 complexes like $[\text{Cu}(\text{H}_2\text{O})_6]^{2+}$ are related to the fact that one of the degenerate orbitals are singly occupied. Moreover, most of the modern quantum chemistry codes are based on eigenvalue calculations on molecular orbitals, which enable relatively fast and accurate electronic structure calculations.

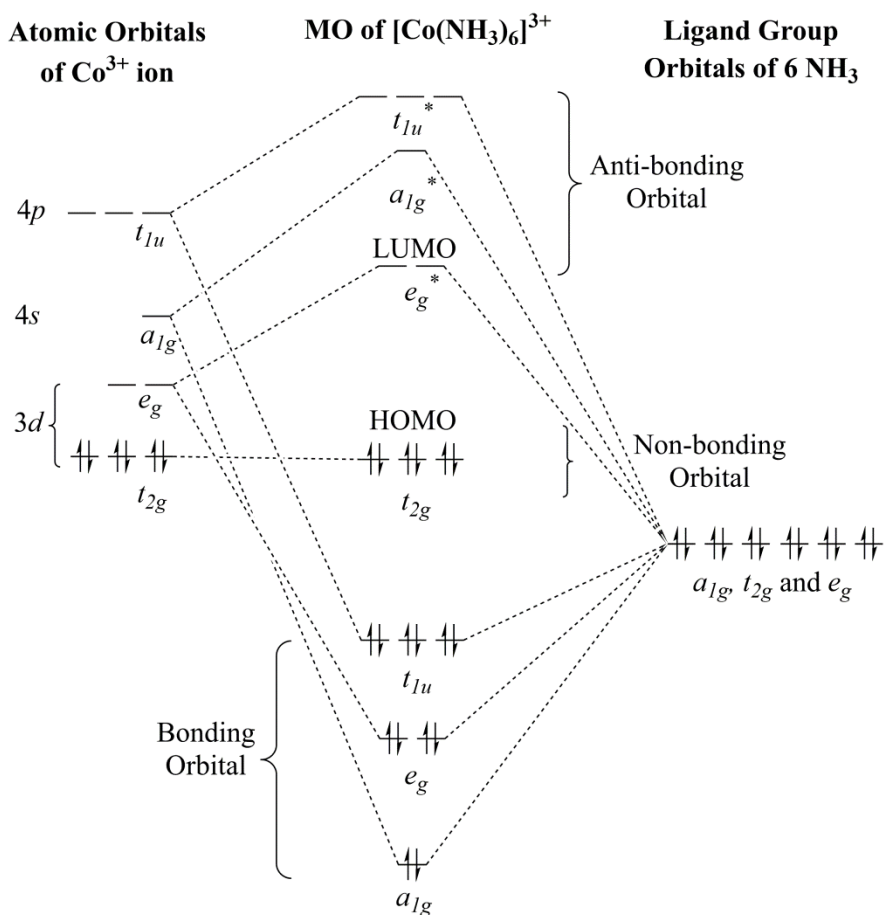


Figure 3. The MO diagram of the cation $[\text{Co}(\text{NH}_3)_6]^{3+}$ with O_h symmetry.

The previous overview of VB theory and MO theory demonstrates how they interpret the properties of transition metal complexes. In general, valence bond theory uses localized orbitals while ligand field theory uses delocalized orbitals. In many cases, these descriptions of the bonding are quite similar. As shown in **Figure 3**, the σ donor orbitals on ligands are lower in energy than the metal valence orbitals. So the component of the six bonding orbitals must be mainly from ligand orbitals. Also the electron density on these orbitals must be mainly contributed by nitrogen atoms. This description is

similar to the VB view in which the six ligands donate their lone pairs to the empty orbitals on the metal center. Furthermore, in the MO descriptions, the metal center contribute six empty orbitals (two $3d$, one $4s$ and three $4p$) to form the bonding MO, which is also approximately consistent with the d^2sp^3 hybridization proposed by the VB model. The above discussion shows that the chemistry drawn from the same system by the two different models is very similar, only in different ways. In general, MO theory is good at interpreting properties like spectra and magnetism, while VB often provides easier descriptions of bonds and reactions since it has a localized frame of references. So chemists often freely switch between the two models when necessary. Both VB and MO models will be applied in the later discussion on specific systems.

1.4 Back donation from metal center to the ligand

In the bonding pattern reviewed so far, we focused on donations of σ lone pairs electrons from the ligands to the empty orbitals on metal center. However, the metal center may also donates its electrons back to the ligand via π interactions, known as back-donation. Three features can be found from the compounds including effective back-donation: 1) the ligand should have empty orbitals which have π symmetry; 2) these orbitals should be close in energy to the d_{xy} , d_{yz} or d_{xz} orbitals on the metal and 3) the metal center should be electron rich, otherwise there will be no electron density to donate.

Carbonyl and ethylene are two typical ligands often used in demonstrations of back-donation. For the carbonyl, the carbon end donates electron density to the empty orbital on the metal center via σ interaction. Since the π bonding orbital in CO has larger

oxygen component, the π^* has larger carbon component, which makes it easier to accept electron density from filled d orbitals (**Figure 4**). The side-on metal ethylene complex has similar situation. The donation and back donation also has σ and π symmetry, respectively.

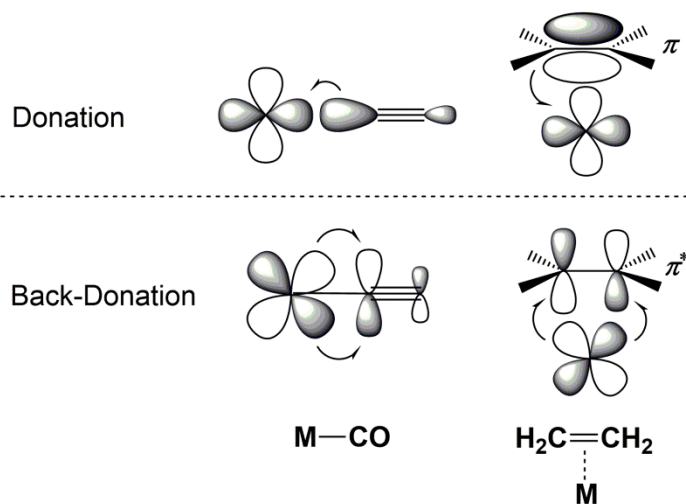


Figure 4. The illustration of back-donation in metal carbonyl and side-on metal ethylene complexes. The arrows indicate the directions of electron flow in bond making.

The existence of back-donation usually has several consequences. On the one hand, back-donation strengthens the metal-ligand bond by forming extra interactions, which leads to shorter metal ligand bond lengths. From the MO perspective, the mixing of the ligand π^* orbital and non-bonding metal orbital stabilize the occupied orbitals on metal center, providing some bonding characteristics to those orbitals. So the interactions between ligand and the metal center become stronger. On the other hand, the electron density donated into the π^* orbital on the ligand weakens the overall bonding

interactions in the ligands, which causes the bond length in the ligand (the C-O bond in carbonyl and C-C bond in ethylene) to lengthen. Weaker C-O bond has lower stretching frequencies, which can be detected by infrared spectroscopy and used to determine how electron-rich the metal center is.

1.5 Multiple bonds between transition metal and ligand: carbene

Multiple bonds are very common in organic compounds like $\text{CH}_2=\text{CH}_2$ and $\text{CH}\equiv\text{CH}$. Actually, carbon atoms can also form double bonds and triple bonds with transition metal atoms, which are known as metal-carbene complexes and metal-carbyne complex, respectively.⁵

A free carbene CR_2 has two spin states, singlet and triplet. Singlet carbene has a lone pair in sp^2 orbital, while triplet carbene has its sp^2 orbital and p orbital singly occupied (**Figure 5**). Generally speaking, free carbene is very reactive and short-lived. Great effort has been placed on synthesizing stable carbene and a number of examples (in either singlet or triplet) are developed over the past several decades.

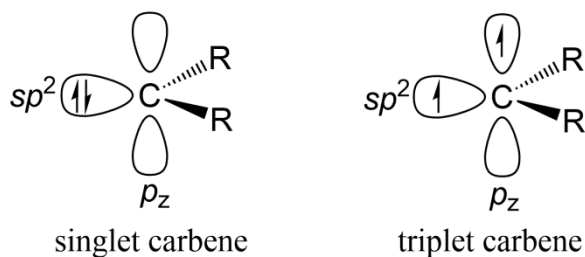


Figure 5. The electron occupations in singlet carbene and triplet carbene.

Acting as ligand, the unstable carbene fragment forms a strong bond with the metal atom because the dissociation is highly disfavored. Metal carbene complexes are often classified into two types: Fischer carbenes and Schrock carbenes.^{1,2} Fischer carbenes are complexes of carbenes that have one π -donor substituent with a middle-to-late metal center. The metal center should be a π -base, but not a very strong one. Schrock carbenes are complexes of carbenes that have only H or hydrocarbyl substituents with an early metal center (often d^2 , d^0 if the two electrons are thought to be transferred from metal to carbene fragment). These two well-known carbene complexes differ in several aspects of their electronic structure and reactivity.

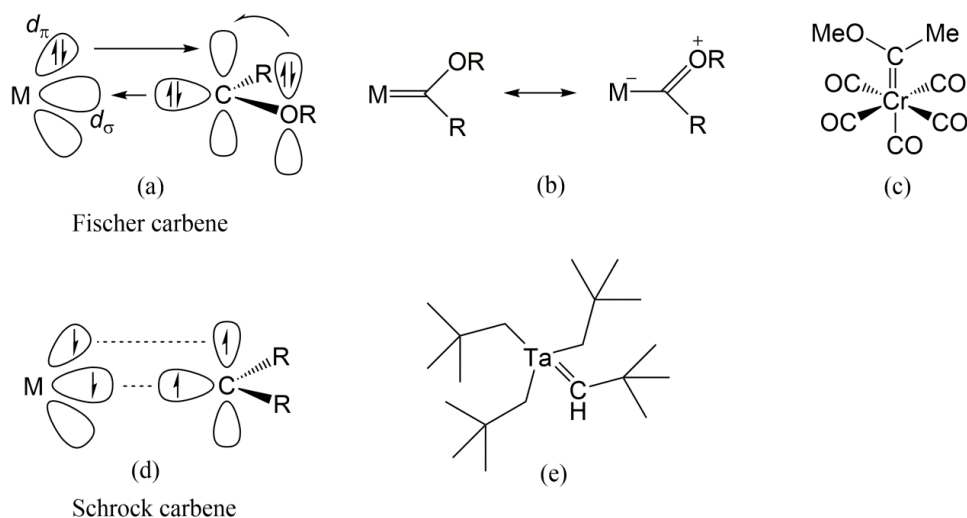


Figure 6. (a) The bonding pattern of Fischer carbenes. (b) The resonance structure of a Fischer carbene. (c) An example of Fischer carbene. (d) The bonding pattern of Schrock carbenes. (e) An example of Schrock carbene.

From the VB view, the free Fischer carbene fragment is typically a singlet carbene with a filled sp^2 orbital and an empty p orbital on the carbon. It can donate its σ lone pair to the metal center as well as accept electrons from the metal center and its π -donor substituent, OR in **Figure 6** (a). **Figure 6** (c) is an example of Fischer carbene. The five carbonyl ligands withdraw significant amount of electron density from the chromium, greatly decreasing the basicity of the metal center. Moreover, because the empty p orbital on the carbon is a weak π acceptor, the σ donation is only partly compensated by the metal back-donation, which gives rise to an electrophilic carbon atom. The π -donor substituent (OR) on carbon also contributes electron densities to stabilize the electron-deficient carbon, making the Fischer carbene complex as a resonance between the two extremes shown in **Figure 6** (b). As a result, the real structures characterized by X-ray studies often show longer M-C bonds and shorter C-O bonds. In this regard, Fischer carbene can be viewed as a two-electron donor σ ligand with π base character, which is similar to carbonyl.

A Schrock carbene (triplet ground state) forms two covalent bonds with a triplet metal center (**Figure 6** (d)). Because the electronegativity of carbon is always lower than early metals, the M=C bond is polarized toward the carbon atom, which leads to a nucleophilic carbon on the carbene. Unlike the Fischer carbene, which does not change the oxidation state of the metal center, Schrock carbene increases the oxidation state of the metal center by 2 units, so it is often view as an anion with two more electrons grabbed from the metal center. Schrock carbenes usually contain early transition metal

center since they are more prone to lose electrons. **Figure 6** (e) is an example of Schrock carbene which has a d^0 (Ta(V)) center.

The differences between Fischer and Schrock carbenes can also be illustrated by MO language. As shown in **Figure 7**, for Fischer carbene complex, the large energy gap between σ orbital and π orbital leads to a singlet ground state for the free carbene fragment. The energies of metal d orbitals are lower than that of the π orbital on the carbene ligand, so the HOMO has more metal character and the LUMO has more ligand character. Therefore the Fischer carbene is electrophilic at the carbene ligand and nucleophilic at the metal center. A typical Schrock carbene has an early metal center, which is higher in energy than the orbitals on the ligands. Since the ligand fragment has triplet ground state, the σ and π orbitals are close in energy. The HOMO has more metal character and the LUMO has more ligand character. So Schrock carbene is nucleophilic at the carbene ligand and electrophilic at the metal center.

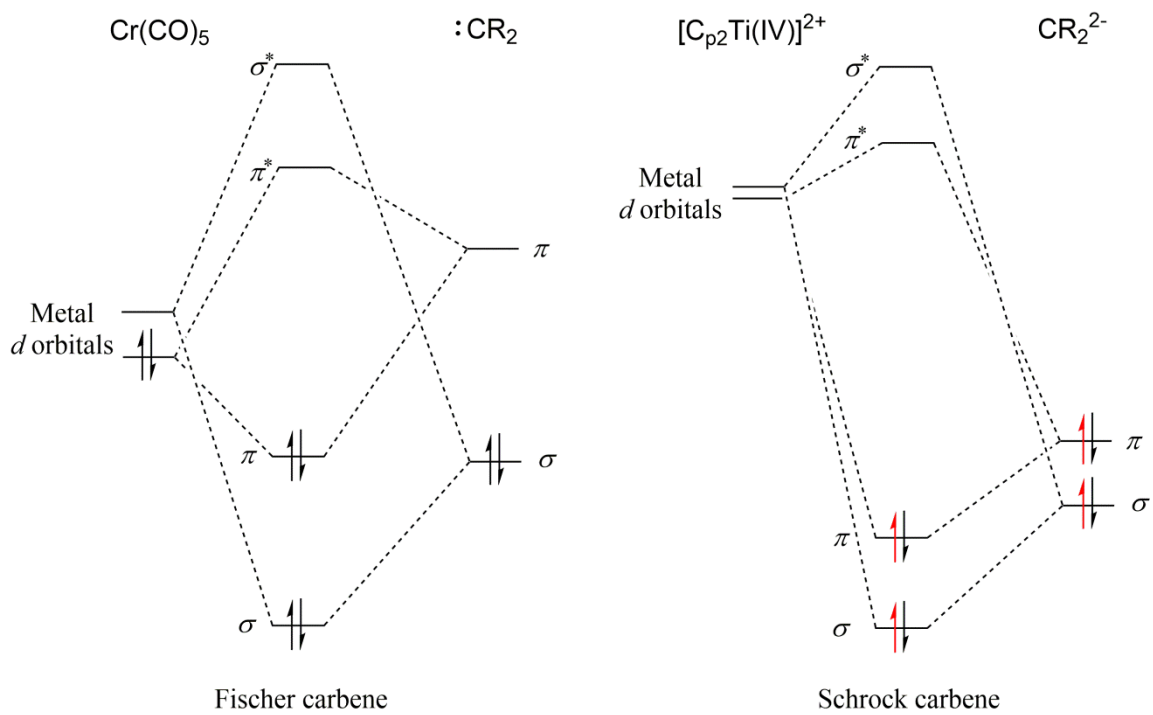


Figure 7. MO diagram of Fischer carbene and Schrock carbene. In Schrock carbene, the metal center does not tend to hold the electrons. So the two electrons are transferred to the carbene. The two electrons from metal center are colored red in the figure.

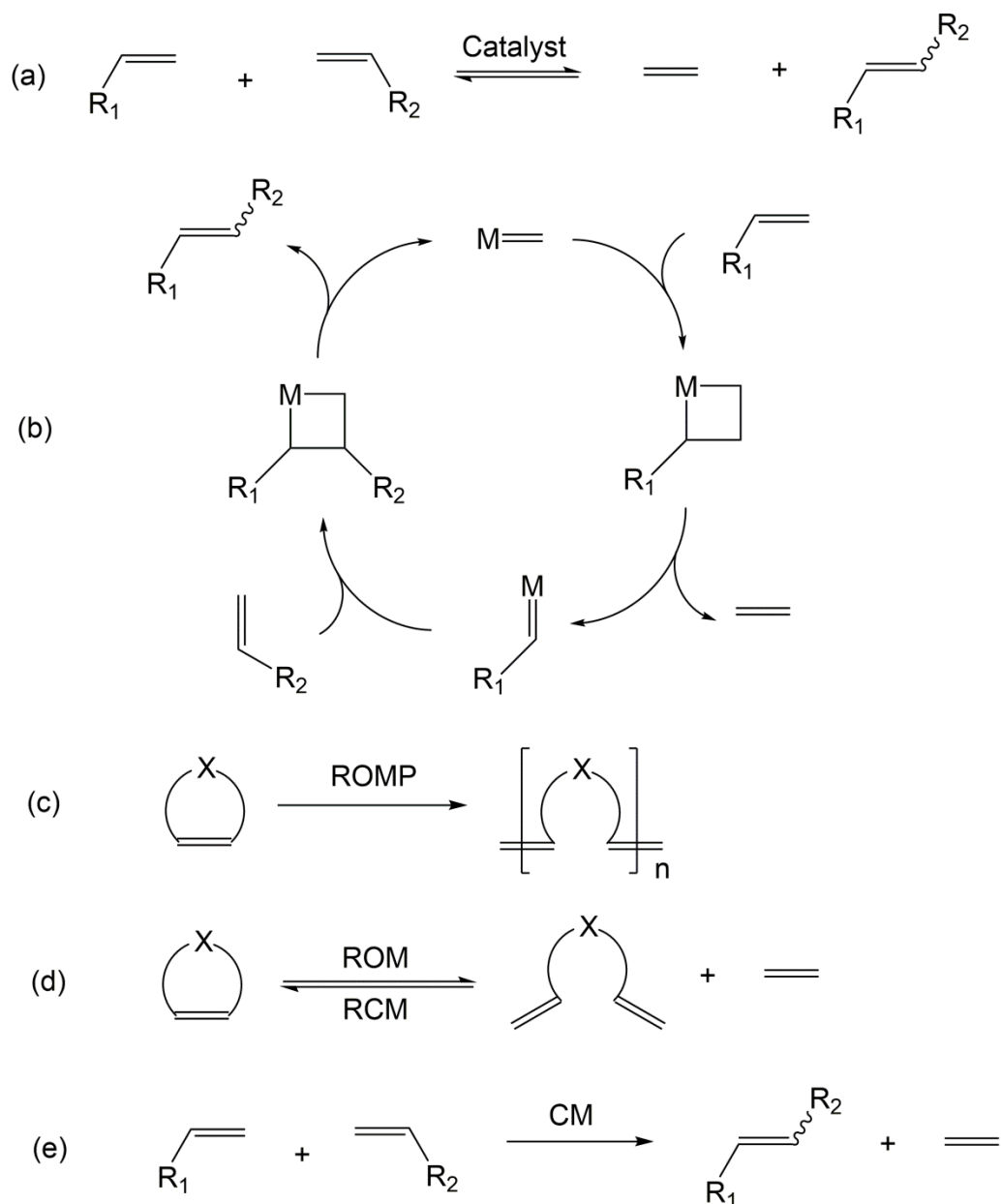


Figure 8. (a) An example of olefin metathesis reactions. (b) A brief mechanism of the olefin metathesis reaction shown in (a). The general schemes of several important types of olefin metathesis reactions: (c) ring opening metathesis polymerization (ROMP); (d) ring opening metathesis (ROM) and ring closing metathesis (RCM) and (e) cross metathesis (CM).

Reactivity wise, both the electrophilic Fischer carbenes and the nucleophilic Schrock carbenes have very rich chemistry. One of the signature reactivity of them is forming metallocycles with alkenes, and the metallocycle can break down to another pair of carbene and alkene. This process is able to exchange the ends of double bonds in olefins (**Figure 8** (a) (b)), thus, appearing as a metathesis reactions: $AB + CD \rightarrow AC + BD$. So this reaction is known as olefin metathesis, which has remarkably wide applications in both organic and polymer chemistry (**Figure 8** (c), (d) and (e)). Metal carbene compounds can serve as catalyst for olefin metathesis reactions. The Grubbs catalysts and Schrock catalysts (**Figure 9** shows one example for each group.) are the best catalysts so far for alkene metathesis and many of them are commercially available.

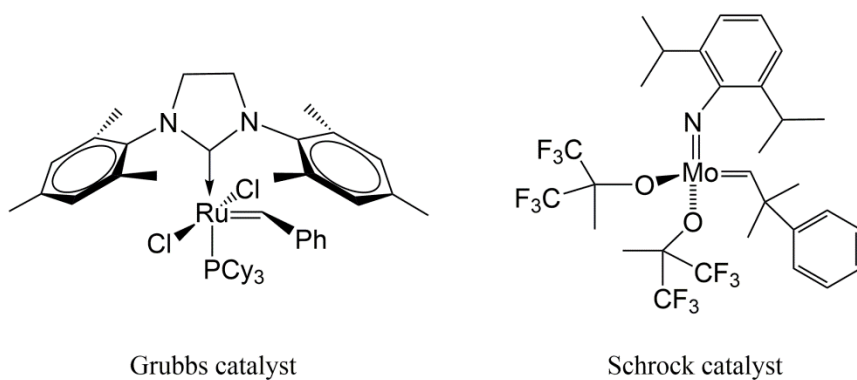


Figure 9. The structures of the 2nd generation Grubbs catalyst and the Schrock catalyst.

A metal carbyne complex features a metal-carbon triple bond. In general, metal carbyne complexes are less common than metal carbene complexes, and metal carbyne compounds are more common for 5*d* metals. Often it is not easy to assign definite oxidation states to carbyne complexes. RC fragment can be treated as an X₃ ligand (RC³⁻,

which is similar to Schrock carbene case), an LX ligand (RC^-) or an L ligand (RC^+ , similar to CO ligand). Similar to carbene complexes, carbyne complex feature alkyne metathesis reactions, which are useful in alkyne synthesis.

1.6 More on metal ligand multiple bonds

In addition to carbon, transition metals form multiple bonds with many other main group elements. The most common ones are terminal oxo $M=O$, nitride $M\equiv N$ and imido $M=NR$. Due to the high electronegativity of O and N, they can be viewed as “Schrock type” ligands, O^{2-} , N^{3-} and NR^{2-} .²

“Oxo wall” is a well-known observation on oxo metal compounds.⁶ It states that no molecular terminal-oxo complex is known for octahedral metal centers with d -electron counts beyond 4. Otherwise, the compound will be highly unstable due to the strong electron repulsion. Thus, there seems to be a wall between iron triads and cobalt triads. The controversial exceptions beyond this wall, which were synthesized by Craig Hill’s group (eg. d^6 Pt(IV) oxo compound) were voluntarily retracted. So far the “oxo wall” still stands.⁷

The existence of “oxo-wall” can be rationalized by **Figure 10**. In a typical d^0 L_5M -oxo compound, when the metal-oxo π interactions are turned on, the previous nonbonding d_{xz} and d_{yz} orbitals on metal will be pushed up in energy since they are the major component of the π^* orbital. The bonding orbitals are occupied by the three pairs of electrons coming from the oxo ligand O^{2-} . All the electrons from metal will be placed on the nonbonding orbital d_{xy} or the π^* orbitals. If the electron count of the metal is 2, there is a triple bond; at 4 electrons the bond is reduced to double. Further occupation of

the π^* orbital makes the M-O bond too weak to be stable. At electron count of $5d$ or higher, the σ bond cannot hold the oxo ligand and the metal center together due to the strong repulsion between the two electron rich fragments, making the molecule highly unstable. Similar ideas hold for metal nitrido and metal imido compounds.

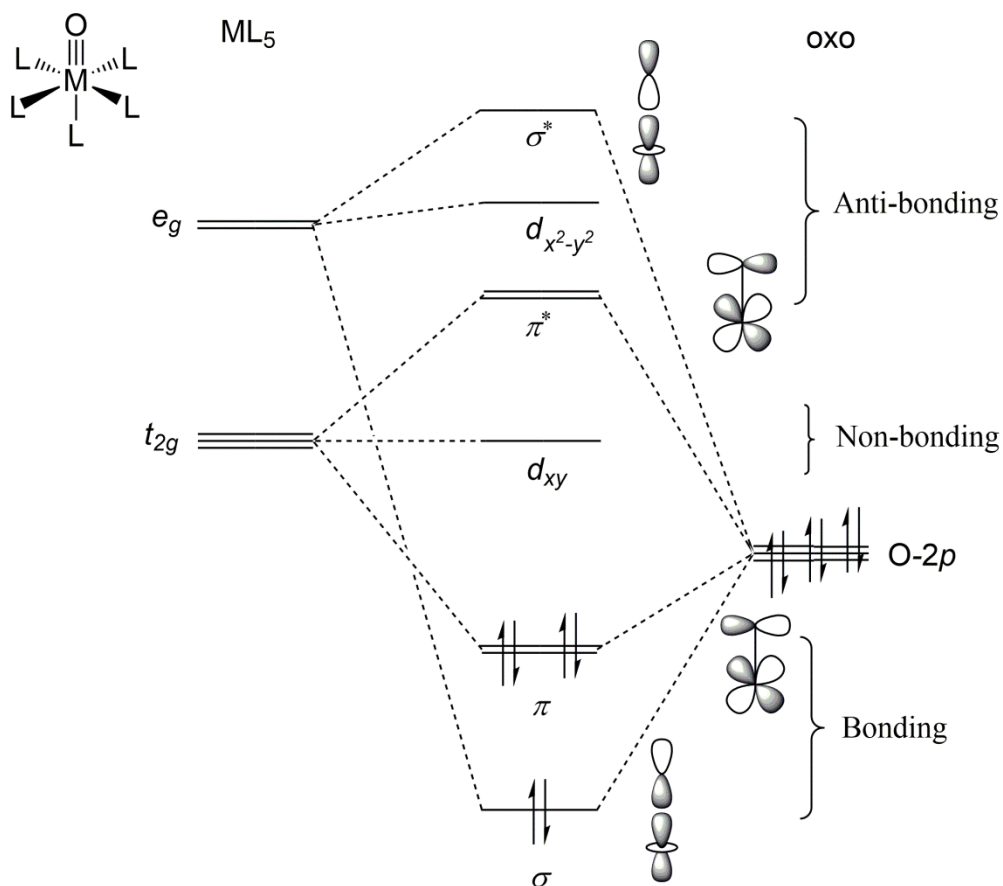


Figure 10. Qualitative molecular orbitals of the d -block of a d^0 metal-oxo compound with octahedral structure.

Besides oxo, transition metal can also form multiple bond with imido,⁸ sulfide,⁹ phosphinidine,¹⁰ and borylene¹¹ ligands. Imido, sulfide and phosphinidine ligands can

often donate their lone pair electrons to empty transition metal *d* orbitals to form dative π bonds. On the contrary, borylene ligand is less electronegative and electron deficient and it can accept π donations from metal center to form multiple bond. Beyond these examples, heavier group 14 elements, Si, Ge, Sn, Pb, can form transition metal multiple bond. The detailed structures and reactivity will be discussed in Chapter III.

In chapter II, the theoretical background of the computational methods used in my research projects will be briefly reviewed. It covers essential basics in quantum mechanics, *ab initio* molecular orbital methods, density functional theory and wavefunction analysis. Chapter III focuses the structure and cycloaddition reactivity of a novel osmium silylyne compounds featuring an Os \equiv Si triple bond. Furthermore, the structure and energetics of the osmium silylyne analogues (M \equiv E, M = Ru and Os; E = Si, Ge and Sn) are studied computationally. Chapter IV and V focuses the formation of transition metal imido compound (M=NR). Chapter IV deals with a system in which a cationic oxorhenium(V) complex reacting with a series of arylazides (N₃Ar) to give cationic *cis*-rhenium(VII) oxo imido complexes. Different trends were found in the experiments for electron-donating versus electron-withdrawing substituted phenyl azides. Computations found all the metal imido products are formed through the same pathway and change in trends in Hammett plot is because the rate determine step switches from metal-azide association to N₂ dissociation. In the system introduced in Chapter V, a series of vanadium (III) terminal organoazides were converted to vanadium (V) imido compounds and they found small quantities of diazenes formed in the reactions. Computational studies were conducted to scrutinize all the possible pathways

and a free nitrene release mechanism is supported based on two reasons: 1) The two-electron reduction on vanadium center during decomposition of azide generates two fragments both in their ground states (triplet states), which might drag the activation barrier down; 2) This conversion is spin-allowed since vanadium center and nitrene nitrogen are antiferromagnetically coupled in transition state.

CHAPTER II

THEORETICAL BACKGROUND

This chapter provides a brief review of the theoretical background of the computational tools I applied in this dissertation. It covers essential basics in quantum mechanics, *ab initio* molecular orbital methods, density functional theory and wavefunction analysis.

2.1 Quantum mechanics and the Schrödinger equation

Classical mechanics has had remarkable success in explaining the motions in macroscopic world. However, in the early 20th century, some physicists started to realize that classical mechanics could not explain the behaviors of objects in the sub-microscopic world like molecules, atoms and electrons. Therefore, quantum mechanics (QM) was formulated, and it is the foundation of theories and methods in computational chemistry today.

Although there are several equivalent mathematical formulations of QM, the wavefunction description is used more often in the chemistry community. The whole QM framework is built on some important postulates dealing with wavefunction, operator, eigenvalue/eigenstate and so on.¹²

A wavefunction is a core concept in QM, which completely describe the states of a QM system. It is related to the probability of finding a particle at position “ x_0 ” and at time “ t_0 ” through Eq. 1. Because of the probabilistic interpretation, a well-behaved wavefunction is required to be normalization, single-valued and continuous.

$$P(x_0, t_0) = \psi^*(x_0, t_0)\psi(x_0, t_0) = |\psi(x_0, t_0)|^2 \quad (\text{Eq. 1})$$

In all the QM systems, each physical observable q is associated to a Hermitian operator Q , which yields real numbers when operating upon the wavefunction of the specific system. If the operation results in the relationship shown in Eq. 2, we call the definite number q_n as an eigenvalue of the eigen-state or eigen-function Ψ_n . It describes that the value of a specific physical observable can be measured as q_n in the corresponding state Ψ_n .

$$\hat{Q}\psi_n(x) = q_n\psi_n(x) \quad (n = 0, 1, 2, \dots) \quad (\text{Eq. 2})$$

If the potential energy of a system does not evolve over time, the system could be described by the time independent Schrödinger equation. This central equation of quantum mechanics is an eigenvalue equation:

$$\hat{H}\psi_n(x) = E_n\psi_n(x) \quad (n = 0, 1, 2, \dots) \quad (\text{Eq. 3})$$

H is Hamiltonian, which is an operator corresponding to the total energy of the specific system. For a QM system that is under certain boundary conditions, the energy can only take some discrete values, which are called energy levels. E_0 normally denotes the energy of the ground state and E_n denotes the energy of the n^{th} excited state of the

system. For any atom or molecule, its total energy contains the kinetic energies of all the nuclei and electrons, as well as the potential energy arising from 1) the Coulombic nuclei-electron attraction 2) the Coulombic nuclei-nuclei repulsion and 3) the Coulombic electron-electron repulsion. So the Hamiltonian could be written as a summation of all kinetic and potential energy operators corresponding to these energies.

$$H = - \sum_i^{\text{electrons}} \frac{\hbar^2}{2m_e} \nabla_i^2 - \sum_K^{\text{nuclei}} \frac{\hbar^2}{2m_N} \nabla_K^2 - \sum_i \sum_K \frac{e^2 Z_K}{r_{iK}} + \sum_{i < j} \frac{e^2}{r_{ij}} + \sum_{K < L} \frac{e^2 Z_K Z_L}{R_{KL}} \quad (\text{Eq. 4})$$

2.2 Born-Oppenheimer approximation

Although the Schrödinger equation provides the theoretical background to calculate the energy and the corresponding wavefunction for any molecule, in reality no exact analytical solution to this equation can be found for any system having more than one electron. Even the numerical solution of a typical molecule is a formidable task. So some reasonable approximations must be made to the Hamiltonian so that solving the equation will be practical. The Born-Oppenheimer (BO) approximation is a fundamental one of them.

If we can recall the mass of an electron is just 1/1836 of a proton, the movement of a proton is far slower than that of an electron. When the nuclei move, the electrons will relax to the optimal density almost instantaneously. So it is convenient and reasonable to decouple the motion of protons and electrons and calculate the electronic energy for fixed nuclear positions. This is the major idea of the BO approximation.

When it is applied to the Hamiltonian, the nuclear kinetic energy term becomes independent of electrons; the correlation term in the attractive electron-nuclear interaction vanishes and the nuclear-nuclear repulsion potential term becomes constant for a given geometry. The energy obtained for this simplified Hamiltonian is called electronic energy which only depends upon the nuclear positions but not their motions. Based on this dependence, one can imagine a multi-dimensional surface with nuclear positions as variables, on which molecules can move with various geometries and energies. This surface is known as potential energy surface. One can locate local minima, transition states on this surface to help describe and understand chemical reactions.

Of course, there are certain cases in which the BO approximation breaks down. For example, when two potential energy surfaces are degenerate at some geometry points, the coupling of electronic and nuclear vibrational motions are non-vanishing. These points are called conical intersection and BO approximation breaks down at these points.

In general, the BO approximation is extremely mild but it effectively removes the complexity caused by nuclei-electron correlation. However, the remaining problem regarding electronic interactions is still far beyond solvable.

2.3 The Hartree-Fock approximation

As mentioned above, the inter-electronic repulsions in the molecule are quite complicated since they are pairwise and inseparable. Further approximation is necessary to make it possible to perform quantum computations on average-size molecules.¹³ The

simplest way is to begin by ignoring all of the electron-electron repulsions. Then the full Hamiltonian can be divided into N (the number of electrons) one-electron Hamiltonian h_i .

$$h_i = -\frac{1}{2}\nabla_i^2 - \sum_K \frac{Z_K}{r_{iK}} \quad (\text{Eq. 5})$$

all these h_i simply add up to the full N-electron Hamiltonian. Each individual electron only feels attractions from all the nuclei therefore its energy and wavefunction can be easily calculated via this eigenvalue equation.

$$h_i \psi_i = \varepsilon_i \psi_i \quad (\text{Eq. 6})$$

The total electronic energy is the summation of energies of all the electrons. The overall wavefunction is the product of all the one-electron wavefunction, which is called Hartree-product wavefunction. However, this approximation is too crude because the electron-electron repulsion is very important to the system.

One way to correct this is adding the repulsion term from the other electrons into the one-electron Hamiltonian.

$$h_i = \frac{1}{2}\nabla_i^2 - \sum_k \frac{Z_k}{r_{ik}} + \sum_{j \neq i} \int \frac{\rho_j}{r_{ij}} dr \quad (\text{Eq. 7})$$

Since the electrons are treated as wavefunction, charge density is used here and an integral over the whole space is necessary. It might seem that all the interactions are considered in this equation. However, the charge density is calculated as the square of the wavefunction (Eq. 1) and we cannot carry out the calculation of Eq. 7 when the wavefunction is unknown.

To solve this problem, Hartree proposed an iterative ‘self-consistent field’ (SCF) method.¹⁴ In the first step, one generates a set of guessed wavefunctions for all the occupied orbitals and uses them to construct the one-electron Hamiltonian h_i . Solving Eq. 6 for each electron for a new set of wavefunctions, which should be more accurate than the previous ones. Having the new set of wavefunctions in hand, one can update the h_i 's by calculating charge density from the them. Repeating this process until the wavefunction is close enough to the previous produces a converged wavefunction and the electronic energy of the system. A converged wavefunction and electronic energy is the foundation of computations of almost all properties of any molecule.¹⁵

At the beginning of any SCF process, one needs an approximated wavefunction although the Hartree product seems to be a good candidate, it has a fundamental flaw. According to the one of the basic postulates of quantum mechanics, the electronic wavefunction should be anti-symmetric due to the Fermion nature of electrons. John Slater proposed a scheme to construct the wavefunction, which is named as Slater determinant. For an N -electron system, the slater determinant is defined as

$$\Psi(x_1, x_2, \dots, x_N) = \frac{1}{\sqrt{N!}} \begin{vmatrix} \chi_1(x_1) & \chi_2(x_1) & \dots & \chi_N(x_1) \\ \chi_1(x_2) & \chi_2(x_2) & \dots & \chi_N(x_2) \\ \vdots & \vdots & \ddots & \vdots \\ \chi_1(x_N) & \chi_2(x_N) & \dots & \chi_N(x_N) \end{vmatrix} \quad (\text{Eq. 8})$$

where $\chi_a(x_b)$ refers to orbital χ_a of electron x_b . Two important properties are built into this form of wavefunction. If two electrons have exactly the same spin-orbital function, two columns in this determinant will be the same, which makes it vanish. If any two electrons are exchanged, two corresponding rows in the determinant switch, which, according to the properties of determinants, reverses its sign.

For a close shell system with $2n$ electrons, the total energy of Slater determinants is calculated as

$$E_{tot}^{HF} = 2 \sum_{i=1}^n \varepsilon_{ii} - \sum_{i=1}^n \sum_{j=1}^n (2J_{ij} - K_{ij}) \quad (\text{Eq. 9})$$

Hartree SCF procedure is also applied in determining the optimal wavefunction and its total energy. J_{ij} and K_{ij} are known as Coulomb integral and exchange integral. Coulomb integral represent the Coulomb interactions between an electron in orbital i and an electron in orbital j .

$$J_{ij} = \iint \chi_i^2(1) \frac{1}{r_{12}} \chi_j^2(1) dr_1 dr_2 \quad (\text{Eq. 10})$$

Unlike the Coulomb integral, the exchange integral does not have an immediate classic interpretation. It is a result of Pauli principle.

$$K_{ij} = \iint \chi_i(1)\chi_j(2)\frac{1}{r_{12}}\chi_j(1)\chi_i(2)dr_1dr_2 \quad (\text{Eq. 11})$$

In Hartree Fock framework the system having parallel spin is lower in energy than the one with opposite spin by K_{ij} . This is because the Slater determinant reduces the probability of finding two electrons of the same spin close to one another, which lowers the energy of the entire system. This effect can also be described as a so-called ‘Fermi hole’ around each electron. Unfortunately, the correlation between electrons with opposite spin is not built into Slater determinant.

In HF framework, the electron correlation is approximated as calculating each electron’s interaction with an average electrostatic repulsion of all the other electrons in the system. Although Fermi hole is considered in the calculation to reduce the total energy, Coulomb hole, which avoids opposite-spin electrons getting too close, is not included. So the total energy from HF approximation is always higher than the real energy of the system.

Before any practical computations on most molecules, the molecular orbitals are unknown. So basis set are introduced to construct the molecular orbitals in the wavefunction.

2.4 Basis set approximation

According to mathematic principles, any type of basis functions can be used to construct the MOs of the system.¹³ Slater and Gaussian functions are two most common choices. Slater functions are defined as

$$\chi_{\zeta,n,l,m}(r, \theta, \varphi) = NY_{l,m}(\theta, \varphi)r^{n-1}e^{-\zeta r},$$

and Gaussian functions are defined as

$$\chi_{\zeta,n,l,m}(r, \theta, \varphi) = NY_{l,m}(\theta, \varphi)r^{2n-2-l}e^{-\zeta r^2}.$$

The major difference between them is in the radial part. The Gaussian function decays faster than Slater function as the radius increases. Gaussian function also behaves differently from Slater function in the near-core region (**Figure 11**).

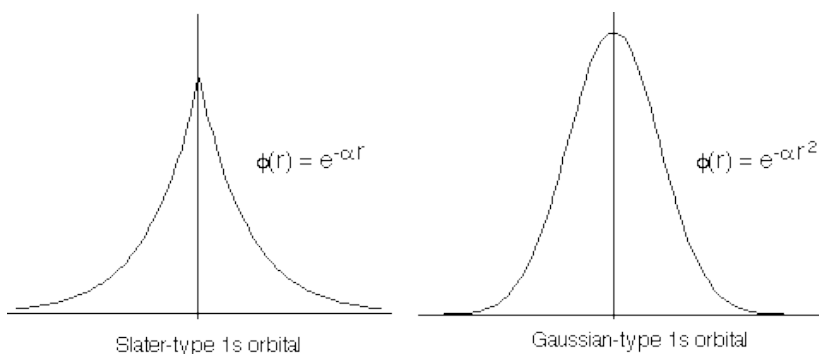


Figure 11. The comparison of Slater function and Gaussian function.

Generally, Slater functions provide more accurate descriptions of the radial part of the atomic orbitals than Gaussian functions. However, usage of Gaussian functions instead of Slater functions saves significant amount of time in the two-electron integrations, which is the most intensive part in quantum computations. As a compromise between efficiency and accuracy, a scheme in which a Slater function is replaced by a linear combination of several Gaussian functions was proposed. To maximize the flexibility of the electron density, polarization functions corresponding to higher angular momentum functions and diffused functions having very expanded tails from their small exponent can be added to the basis set. More basis functions bring about more accurate computational results, but with higher expense.

Basis sets discussed above work fine for light atoms, but have poor performances for heavier elements. On the one hand, considering each electron explicitly in the calculation produces additional cost and is usually not necessary for the core electrons. On the other hand, relativistic effects play more important roles in heavier elements and their full considerations bring additional effort. In order to solve this problem, effective

core potentials (ECP) have been developed to replace the core electrons. Since generally only valence electrons are important to chemical reactions, the effects that core electrons have on the valence electrons are simplified by using ECP fitted to experimental data. The valence electrons are still represented by basis set which can be altered to allow the necessary flexibility. In this way, the computation time is greatly saved and the results are usually satisfying. Currently, Stuttgart/Dresden ECP, (SDD, using triple- ζ basis set for valence electrons) and LANL2DZ ECP (developed in Los Alamos national lab, using triple- ζ basis set for valence electrons) basis sets are the most popular choices.

2.5 Electron correlation

Hartree-Fock approximation and basis set approximation give rise to errors in the computational results. If the molecular orbitals are expanded with infinite number of basis functions, the errors from basis set approximation will be removed, and the remaining errors just come from the simplified way HF deals with electron correlation. So an important concept, correlation energy, is defined as the difference between the Hartree-Fock limit (HF energy on infinite basis set) and the exact non-relativistic energy of the system.¹⁵

$$E_{corr} = E_{exac} - E_{HF} \quad (\text{Equ.12})$$

To recover the correlation energy as much as possible, many methods are available with various accuracy and expenses and they are divided into two major categories. First category is post-HF methods, which take excited state configurations

into account in the overall wavefunctions. These methods are usually referred to as explicit correlation. Another category is density functional theory (DFT), which tries to incorporate electron correlation in the functional. I will give a brief introduction to post-HF methods here, and leave DFT for next section.

The major idea of post-HF methods is that the inclusion of excited (double and higher) determinants in the wavefunction helps reduce the overall energy of a system. Let us take di-hydrogen molecule as an example. If we just consider the $1s$ orbitals on each hydrogen atom, they form one bonding orbital and one anti-bonding orbital as shown in **Figure 12**. The ground state of H_2 molecule is σ^2 , which has two electrons occupying the bonding orbital. Although it might seem that the inclusion of excited σ^{*2} determinants will raise the total energy of the system since the anti-bonding orbital has higher energy than bonding orbital, adding contributions from these determinants to the wavefunction increases the probability that the electrons are on either side of the node, which reduces the probability of instantaneous interactions. Additional doubly excited determinants can provide radical correlations from more diffused orbitals and angular correlation from determinants made from polarization functions. When excited states are considered, the overall consequence is that electrons can move in a larger space, and the probability of getting too close is reduced. These factors contribute in less electronic repulsion and a lower total energy.

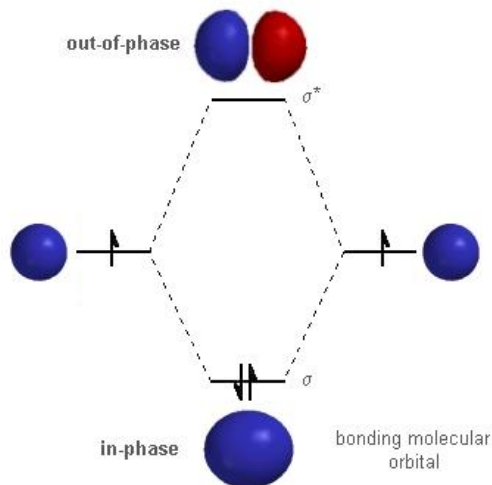


Figure 12. The MO diagram of H_2 molecule.

2.6 Density functional theory

DFT¹⁶ accounts for electron correlation in the electronic structure calculations by including it in the parameterization of the functional. Thus, it is an implicit approach in that it would produce an energy as if the electrons were correlated but it does not have a wavefunction with correlating electrons. In most cases it provides satisfyingly accurate results at a fairly affordable cost. This feature has made it increasingly popular in chemical research in the past several decades.

The theoretical framework of DFT is based on two Hohenberg-Kohn theorems.¹⁷ The first one states that the ground-state properties of a many-electron system are uniquely determined by an electron density that depends on only 3 spatial coordinates. The second one defines an energy functional for the system and proves that the correct ground-state electron density minimizes this energy functional. Although those two

theorems prove the existence of an energy functional which would produce the accurate ground-state energy from the electron density, they does not tell us how to determine this functional.

The key breakthrough came from Kohn-Sham density functional theory,¹⁸ which brought back orbitals into the calculations. The electron density can be calculated from Kohn-Sham orbitals by

$$\rho = \sum_{i=1}^{N_{elec}} |\phi_i|^2 .$$

Kohn-Sham proposed a fictitious system of non-interacting electrons having the same electron density as a system in which the electrons do interact. The energy functional can thus be divided into several parts.

$$E[\rho(r)] = T_{ni}[\rho(r)] + V_{ne}[\rho(r)] + V_{ee}[\rho(r)] + \Delta T[\rho(r)] + \Delta V_{ee}[\rho(r)] \quad (\text{Equ. 13})$$

The terms on the right hand side of Equ 13 represent the kinetic energy of the non-interacting electrons, the nuclear-electron interactions, the classic electron-electron interactions, the corrections to the electron kinetic energy due to the all electron interactions, and the corrections to all the non-classical electron-electron interactions. The first three non-interacting terms are exactly the same as the terms in HF theory, and the last two terms add up to exchange-correlation energy functional, $E_{xc}[\rho]$. The first

three terms can be exactly evaluated while the exchange correlation part is where all approximations are applied. Normally, the $E_{xc}[\rho]$ term is represented as an interaction between the electron density and the ‘energy density’, ε_{xc} , which is dependent on the electron density,

$$E_{xc}[\rho(r)] = \int \rho(r) \varepsilon_{xc}[\rho(r)] dr,$$

and $E_{xc}[\rho]$ is often separated into exchange and correlation energy. Normally, exchange energy is the major part of E_{xc} thus more important. Density functionals are divided into several categories.

The first category is Local Density Approximation (LDA) functional. It assumes the value of ε_{xc} at position r is only related to the local electron density at this position. The exchange energy is calculated as

$$E_x^{LDA}[\rho(r)] = -C_x \int \rho^{4/3}(r) dr \quad (\text{Equ. 14})$$

For more general cases, the electron density with different spin will be considered separately. This scheme is known as Local Spin Density Approximation (LSDA)^{17, 18, 19} and the formula is

$$E_x^{LSDA}[\rho(r)] = -2^{1/3} C_x \int (\rho_\alpha^{4/3}(r) + \rho_\beta^{4/3}(r)) dr \quad (\text{Equ. 15})$$

For correlation energy density, no analytical derivation even for uniform electron gas has been proved possible so far. Only the zero- and infinite-density limits have analytical representations while the cases with intermediate densities are simulated by quantum Monte Carlo techniques. These results are used in construction of analytical interpolation formula for calculating correlation energies in high precision. An example correlation formulation developed by Vosko, Wilk and Nusair (VWN)²⁰ is shown below.

$$\varepsilon_{xc}^{VWN}(r_s,0) = \varepsilon_c(r_s,0) + \varepsilon_a(r_s) \left[\frac{f_2(\zeta)}{f_2'(0)} \right] (1 - \zeta^4) + [\varepsilon_c(r_s,1) - \varepsilon_c(r_s,0)] f_2(\zeta) \zeta^4 \quad (\text{Equ. 16})$$

LDA or LSDA is almost exact for uniform electron gas where the electron density is treated as slowly varying functions. They perform rather poorly for molecular systems, especially in the descriptions of bond making and breaking in which the electron density changes dramatically. In these cases, the gradient of electron density becomes very important.

The next category of density functionals is known as Generalized Gradient Approximation (GGA). In GGA functionals, the exchange correlation energy is a functional of both the density and the first order derivative of density. With the gradient correction, GGA functionals usually have better performance than LDA functionals in chemical systems. One of the earliest and most popular GGA exchange functional was developed by A. D. Becke (B or B88).²¹ This functional corrects the LSDA exchange energy by an extra term (Equ. 17).

$$\begin{aligned}\epsilon_x^{B88} &= \epsilon_x^{LDA} + \Delta\epsilon_x^{B88} \\ \Delta\epsilon_x^{B88} &= -\beta\rho^{1/3} \frac{x^2}{1 + 6\beta x \sinh^{-1} x} \\ x &= \frac{|\nabla\rho|}{\rho^{4/3}}\end{aligned}\tag{Equ. 17}$$

The most popular GGA correlation functional is proposed by Lee, Yang and Parr (LYP)²² and it is often combined with B88 (BLYP) in computations.

In addition to the first order derivative, some GGA functional take the second order derivative of electron density into consideration. This type of functionals is known as meta-GGA. The most popular examples are TPSS²³ and M06L.²⁴

In some GGA or meta-GGA functionals, the local exchange functional might not be able to provide enough exchange energy for some specific systems. Adding a certain fraction of Hartree-Fock exchange energy will improve the results. This type of functional is hybrid-GGA or hybrid-meta-GGA functional. The most successful and popular functional, B3LYP^{25, 22} is hybrid-GGA.

$$E_{xc}^{B3LYP} = (1-a)E_x^{LSDA} + aE_x^{HF} + b\Delta E_{xc}^{B88} + (1-c)E_c^{LSDA} + cE_c^{LYP}\tag{Equ. 18}$$

The ‘3’ in the B3LYP means there are three empirical parameters in this functional, which are determined by fitting to experimental data. This functional works magically well for many systems including organic, inorganic and organometallic compounds and reactions and it is the favorite of many computational chemists. Following the similar

scheme, theoretical chemists proposed other hybrid-GGA functionals like B3P86,²⁶ O3LYP,²⁷ B3PW91²⁸ and several others. There are also examples of hybrid-meta-GGA like TPSSh,²³ M06²⁹ and M06-2X.

Based on including HF exchange or not, functionals can also be divided into two types: hybrid functionals and pure functionals (no HF exchange included). Generally hybrid functionals tend to favor high spin state over low spin state of open-shell molecules because the HF exchange component stabilizes parallel spin by providing larger exchange energy. Therefore, the selection of appropriate functional becomes extremely important for some open-shell systems or in systems that have several close lying states.

For some systems in which dispersion interactions are important, some dispersion corrections must be included to obtain accurate results. The B97-D³⁰ ('D' stands for dispersion) functional developed by Grimme was the first GGA that incorporated dispersion terms from the very beginning. Now the latest version of dispersion correction is D3, which is parameterized for many density functionals.

The DFT-D3 scheme adds a dispersion correction term to the regular Kohn-Sham DFT energy,

$$E_{DFT-D3} = E_{KS-DFT} + E_{disp}, \quad (\text{Equ. 19})$$

in which the dispersion energy is a sum of the two- and three-body contribution to the dispersion energy. The two-body term is more important and it is given at long range by

$$E_{disp}^{(2)} = -\frac{1}{2} \sum_{A \neq B}^{atompairs} \sum_{n=6,8} s_n \frac{C_n^{AB}}{r_{AB}^n}. \quad (\text{Equ. 20})$$

In general, a damping function needs to be added because the dispersion contribution needs to be damped at short distances. One available damping function is proposed by Becke and Johnson (BJ).³¹

$$E_{disp}^{(2)} = -\frac{1}{2} \sum_{A \neq B}^{atompairs} \sum_{n=6,8} s_n \frac{C_n^{AB}}{r_{AB}^n} f_{d,n}(r_{AB})$$

with

$$f_{d,n}(r_{AB}) = \frac{1}{1 + 6(r_{AB}/(s_{r,n}R_0^{AB}))^{-\alpha}} \quad (\text{Equ. 21})$$

The dispersion corrected DFT-D3 yield satisfactory results for non-bonded interactions like these in the benzene dimer. Some regular functionals like B3LYP normally cannot reproduce the attractive dispersion interaction at long distance. So it is important to use their dispersion corrected version. Some functionals in Minnesota family, like M06 and M06-2X can capture the dispersion interaction to some extent because they are parameterized with training sets which contain larger number of examples with dispersion interactions.

2.7 Wavefunction analysis

In HF and KS-DFT, a set of MOs are produced, from which a wavefunction can be written as a single determinant of this set of orthonormal MOs. The MOs can also produce the electron density. It is convenient and efficient to work with canonical MOs since they are easy to deal with mathematically. However, many chemists think in terms of two-center, two-electron chemical bond. The canonical molecular orbitals are often delocalized over the whole molecule and such bonding information is not readily obtained. Because a unitary transformation of a set of SCF-converged canonical MOs does not change the total wave function or the observables, one can create a set of localized orbitals from linear combinations of MOs which are more easily implemented chemically. There are several orbital localization schemes available in modern computational software: Boys,³² Edmiston-Ruedenberg³³ and Pipek-Merzley.³⁴ They have different considerations and standards to localize the orbitals thus their results are usually slightly different from each other.¹³

Natural bond orbital (NBO)³⁵ analysis is a more sophisticated and powerful orbital localization method. The NBO are one of a sequence of natural localized orbital sets that include natural atomic orbitals (NAO), natural hybrid orbitals (NHO), natural bonding orbitals (NBO) and natural localized molecular orbitals (NLMO). Those sets of orbitals can be obtained by diagonalizing the specific blocks in the density matrix, and this procedure generates single Lewis structure to best fit the electron density.

NBO analysis is valuable because it can translate accurate calculation into chemical insights. So one can understand the computational results in terms of

commonly understood bonding concepts: atomic charge (natural charge), bond type (covalent vs. dative vs. ionic; σ vs. π), hybridization, bond order, resonance weights, *etc.* Another great advantage is that the NBO results are less sensitive to basis sets chosen in the calculation, which makes it more justified and trustable.

NBO normally provides qualitative analysis on chemical bonds. If we want to analyze some chemical bond in a quantitative way, Extend Transition State combined with Natural Orbital Chemical Valence (ETS-NOCV)³⁶ is a great choice. ETS-NOCV method is based on fragment molecular orbital (FMO) concepts and closely related to other energy decomposition analysis (EDA) schemes.

In general, this method is used to analyze the interactions between distorted fragments in the molecule of interest. ΔE_{int} is the energy differences between the energy of the whole molecule and the total energy of distorted fragments building this molecule. It accounts for all the interactions needed for the fragments to build a molecule so that it could be partitioned into several components:

$$\Delta E_{int} = \Delta E_{elecstat} + \Delta E_{Pauli} + \Delta E_{orb}$$

These three components could be understood by stepwise process in building the whole molecule with distorted fragments. Firstly, when all the distorted fragments are brought together to their positions in the original molecule from infinite separation without density changes, the system is stabilized by gaining classical Coulomb interaction energy $\Delta E_{elecstat}$. At second step, the total wavefunction of the whole molecule is only

anti-symmetric product of the wavefunctions of fragments, which gives rise to a destabilizing factor: exchange repulsion energy, or ΔE_{Pauli} . (Normally, the sum of $\Delta E_{elecstat}$ and ΔE_{Pauli} is called steric interaction energy, ΔE_{steric} .) At the final step, when the total wavefunction is fully relaxed, the system is further stabilized by orbital energy ΔE_{orb} .

In other energy decomposition analysis,³⁷ the total orbital interaction energy can only be broken apart by different irreducible representations of the specific symmetry of the molecule. It does not work for molecules with low or no symmetries. In NOCV approach, the deformation density could be partitioned into the different components (σ , π , δ) of the chemical bond. At the same time, the total bond energies could also split into different contributions of specific orbital interactions between fragments. This method enables us to get some quantitative information about the chemical bond.

CHAPTER III

STRUCTURE AND REACTIVITY OF AN OSMIUM SILYLYNE COMPOUND*

3.1 Introduction

Carbyne (or alkylidyne) complexes with formal metal-carbon triple bonds have been the focus of considerable fundamental research on structure, bonding and reactivity, especially given the utility of such species in catalysis.³⁸ These investigations have inspired and encouraged the interest in transition metal-group 14 congeners, which are expected to exhibit new and interesting reactivity patterns. Although it was widely accepted that chemical elements with a principal quantum number greater than 2 (e.g. Period 3 elements and lower) do not form stable multiple bonds due to the weak orbital overlap (known as ‘double bond rule’),³⁹ the synthetic effort in pursuing novel transition metal-ylide ($M\equiv E$) compounds never stopped and it has led to several interesting accomplishments. Power and coworkers reported the first successful examples along these lines, with preparation of the terminal germylyne complexes $Cp(CO)_nM\equiv Ge[2,6-Ar_2-C_6H_3]$ ($n = 2, 3$; $M = Cr, Mo, W$; $Ar = Trip, 2,4,6-iPr_3C_6H_2$; $Mes, 2,4,6-Me_3C_6H_2$), by direct reaction of anionic $[Cp(CO)_3M]^-$ complexes with stable $ClGe[2,6-Ar_2-C_6H_3]$ species.⁴⁰ Filippou *et al.* also used halogermylene species to make the germylyne complexes $X(P-P)_2M\equiv Ge(^1-Cp^*)$ ($X = Cl, Br, I$; $M = Mo, W$; $P-P = Ph_2PCH_2CH_2PPh_2, Et_2PCH_2CH_2PEt_2$), and $X(PMe_3)_4Mo\equiv Ge(2,6-C_6H_3-Trip_2)$ *via*

*Reprinted (adapted) with permission from Hayes, P. G.; Xu, Z.; Beddie, C.; Keith, J. M.; Hall, M. B.; Tilley, T. D. *J. Am. Chem. Soc.* **2013**, *135*, 11780. Copyright 2013 American Chemical Society.

oxidative additions of a Ge–X bond.⁴¹ Similar approaches have been used to generate analogous stannylyne complexes.⁴² The first silylyne complex, $[\text{Cp}^*(\text{dmpe})(\text{H})\text{Mo}\equiv\text{SiMes}][\text{B}(\text{C}_6\text{F}_5)_4]$, was obtained in Tilley's laboratory by abstraction of chloride from the corresponding silylene complex $\text{Cp}^*(\text{dmpe})(\text{H})\text{Mo}=\text{Si}(\text{Cl})\text{Mes}$.⁴³ This complex features a linear Mo–Si–C arrangement and a weak Si···H interaction ($^2J_{\text{SiH}}$ 15 Hz). In 2010, Filippou and coworkers have reported the neutral silylyne $\text{Cp}(\text{CO})_3\text{MoSi}(2,6\text{-Trip}_2\text{-C}_6\text{H}_3)$ from a base-stabilized halosilylene adduct.⁴⁴

Despite recent progress in the isolation and characterization, including recent computational studies on metal-ylide complexes of the heavier group 14 elements,⁴⁵ synthetic control of structure and bonding in such compounds is still quite challenging. This is demonstrated by the facts that the known complexes of this type generally require an extremely bulky substituent, and all of them feature a group 6 metal (Cr, Mo, or W). Recently, the first ylide complex of a non-group 6 metal, $[\text{Cp}^*(\text{iPr}_3\text{P})(\text{H})\text{Os}\equiv\text{Si}(\text{Trip})][\text{HB}(\text{C}_6\text{F}_5)_3]$, was synthesized in Tilley's group.⁴⁶ It was prepared from the readily available primary silane $(\text{Trip})\text{SiH}_3$ as the silicon-based starting material. Moreover, this complex is the first $\text{L}_n\text{M}\equiv\text{ER}$ species which features alkyne cyclization reactivity, similar to that observed for carbyne species. In this work, we employed several computational tools to investigate the bonding nature of this osmium silylyne compound and its cycloaddition reactivity. Further computations were also conducted to compare the geometric and electronic structures of the $\text{L}_n\text{M}\equiv\text{ER}$

compounds (M = Ru and Os, E = Si, Ge, Sn) which have the same coordination sphere as the osmium silylyne compound.

3.2 Experimental observations

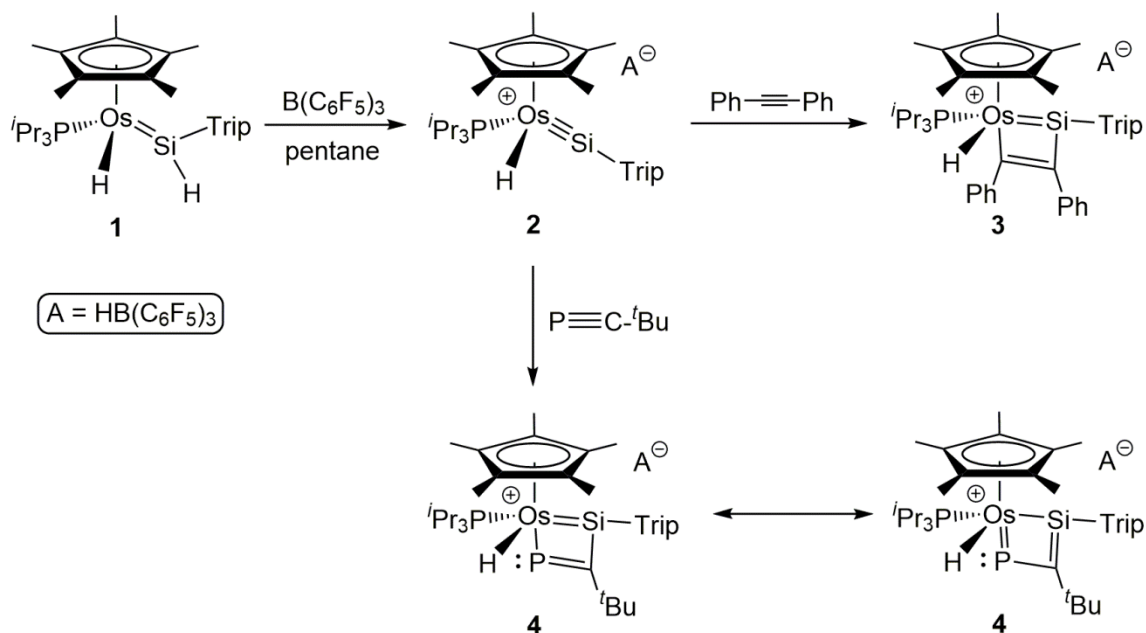
Osmium silylyne compound **2** was synthesized in Tilley's group. They used Lewis acid $B(C_6F_5)_3$ to abstract one hydride⁴⁷ from $Cp^*(iPr_3P)(H)Os=SiH(Trip)$ (**1**). An immediately color change from bright orange to ruby red was observed and they proposed that $[Cp^*(iPr_3P)(H)Os\equiv Si(Trip)][HB(C_6F_5)_3]$ (**2**) was generated in the solution (**Scheme 1**).

2 was isolated but could not be crystalized due to its thermal sensitivity. So it was characterized by a series of solution NMR measurements. The experimental evidences of its existence are: 1) It exhibits a ^{29}Si NMR resonance at δ 321 that is shifted downfield by 92 ppm relative to the resonance for silylene **1**; 2) The conversion of **1** to **2** is accompanied by disappearance of the Os–H and Si–H 1H NMR resonances for **1**, and appearance of a characteristic, hydridic doublet at δ –14.5 (1H, $^2J_{HP} = 29$ Hz) and a broad signal at δ 4.39 (1H) attributed to Os–H and B–H signals, respectively, for silylyne **2**; 3) The attempts to measure the $^2J_{SiH}$ value using variable temperature one- and two-dimensional NMR experiments were unsuccessful, indicating extremely weak OsH \cdots Si interactions; 4) Spectroscopic features of the $HB(C_6F_5)_3^-$ anion show that this anion is only weakly coordinated to the cation part. Furthermore, low temperature NMR studies failed to reveal evidence for Si–H or Si–F contacts.

Since no crystal structure was obtained for compound **2**, reactivity studies were undertaken to provide further evidence of its existence (**Scheme 1**). 1) Treatment of a

bromobenzene solution of silylyne **2** with diphenylacetylene afforded cycloaddition product, $[\text{Cp}^*(i\text{Pr}_3\text{P})(\text{H})\text{Os}=\text{Si}(\text{Trip})(\text{PhC}=\text{CPh})][\text{HB}(\text{C}_6\text{F}_5)_3]$ (**3**). The ^{29}Si chemical shift of Complex **3** is δ 110; 2) Reaction between compound **2** and one equiv of the phosphalkyne $t\text{BuCP}$ produces another cycloaddition product, $[\text{Cp}^*(i\text{Pr}_3\text{P})(\text{H})\text{Os}=\text{Si}(\text{Trip})(\text{P}=\text{C}^t\text{Bu})][\text{HB}(\text{C}_6\text{F}_5)_3]$ (**4**). The ^{29}Si , ^{31}P and ^{13}C chemical shift of Complex **3** are measured to be δ 82, 516 and 278, respectively.

Scheme 1. Generation of **2** and cycloaddition products **3** and **4**.



3.3 Computational details

The computations were accomplished by density functional theory (DFT) as implemented in the Gaussian 09 program.⁴⁸ The NBO 5.9 program⁴⁹ was employed to study the nature of the Os–Si bond, and the ETS-NOCV³⁶ method as implemented in the Amsterdam Density Functional 2012 program (ADF)⁵⁰ was used to study the bonding interaction energies.

The reported geometry, NBO analysis and NMR data in the text were produced with the TPSS⁵¹ functional. Two basis sets were used in this work. In BS1, the energy-consistent relativistic pseudopotential of the Stuttgart/Cologne group (ECP60MWF)⁵² was applied to the osmium atom to represent the 60 inner shell electrons. Valence electrons of osmium were represented by the [8s7p6d/6s5p3d] basis set. The atoms connected directly to the osmium center and those composing the four-member ring in the products have 6-311G(d,p) basis sets.⁵³ All the other atoms have 6-31G(d) basis sets.⁵⁴ In BS2, ECP60MDF core pseudopotential was applied on the osmium atom, the valence electrons have a larger basis set named ECP60MDF_VDZ⁵⁵ ([25s22p13d1f/4s4p3d1f], which is similar to cc-pVDZ-PP basis set), and all the other atoms are represented by 6-311++G(2d, p) basis sets.⁵⁶ All geometry optimizations, NBO analysis and solvation energy calculations were conducted at BS1 level, while all of the NMR data were obtained at BS2 level. For all of the optimized structures, analytical frequencies were computed to obtain the thermal corrections and to confirm their character as local minima. For the accurate calculation of the free energy profile, Grimme's DFT-D3 corrections were used to account for the dispersion interactions.⁵⁷

The solvation corrections to gas-phase free energies were computed by the PCM model⁵⁸ for the solvent used in experiments. All the NMR⁵⁹ results were obtained by the PCM model, also in the corresponding solvent. Tetramethylsilane (TMS) and phosphoric acid were used as reference for the calculations of δ (²⁹Si), δ (¹³C) and δ (³¹P) values of the complexes. The ETS-NOCV calculations were based on the structures optimized by TPSS and BS1 on Gaussian 09. In addition, the ADF calculations were performed with the PBE functional,⁶⁰ which is similar to the TPSS functional, with the TZ2P basis sets without frozen core approximation.

3.4 Computational results and discussion

3.4.1 Geometry of **2**

Because of the difficulties with the crystallization, DFT calculations at the TPSS level were employed to examine the proposed structures of **2**. Only one hydride was abstracted in the conversion of **1** to **2**, both hydrides on osmium and silicon are possible to be removed. Therefore, the two extreme structures **2** and **2'** with the hydrogen located at the osmium and silicon atoms, respectively, as well as the transition state having a bridging hydrogen atom (**TS**) were examined (**Scheme 2**). Results in **Table 1** show that **2'** is 14.8 kcal mol⁻¹ higher in energy (ΔG) than **2** and that it can easily transform to **2** through the bridging hydride transition state (**TS**), with a free-energy barrier of only 5.5 kcal mol⁻¹. Furthermore, the computed ²⁹Si NMR resonance of **2'** (δ 282) does not match the experimental value. Thus, **2** is the exclusive product formed in the hydride abstraction reaction.

Scheme 2. Structural models for 2.

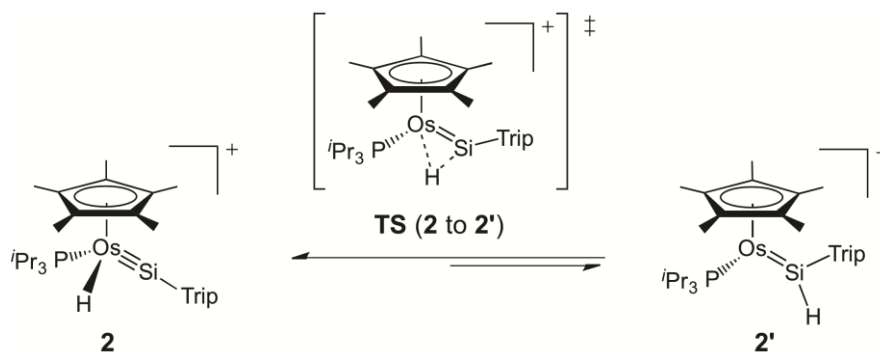


Table 1. Selected bond lengths (Å), bond angle (°) and solvated free energies (kcal/mol).

	ΔG	Os-Si	Os-H	Si-H	Os-Si-C
2	0.0	2.176	1.635	2.760	168.0
TS	20.3	2.254	2.487	1.550	165.0
2'	14.8	2.303	3.298	1.499	135.4

The optimized structure of **2** has some noteworthy characteristics (**Figure 13**). The Os-Si-C bond angle is 168.0°, a value which suggests that the Si atom has nearly sp hybridization. This angle is much larger than the computed value of 135.4° in **2'** (**Table 1**), where sp^2 hybridization would be expected. Furthermore, the computed Os-Si bond length in **2** is 2.176 Å, which is extremely short, contracting by 0.127 Å in the conversion from **2'** to **2**. This predicted contraction is even larger than the observed difference between the Mo-Si bond lengths in $\text{Cp}^*(\text{dmpe})(\text{H})\text{Mo}=\text{Si}(\text{Cl})\text{Mes}$ (2.288 (2))

Å) and $[\text{Cp}^*(\text{dmpe})(\text{H})\text{Mo}\equiv\text{SiMes}][\text{B}(\text{C}_6\text{F}_5)_4]$ (2.219(2)Å).⁴³ Structures of several known compounds that share the same $\text{Cp}^*(\text{iPr}_3\text{P})\text{Os}^+$ fragment (**Figure 14**) were optimized to compare Os-Si bond lengths. The average optimized Os-Si bond lengths contract significantly from the osmium silyl species (**c**, **d** and **e**) to osmium silylene species (**1**, **a** and **b**), and bond order also increased from single to double. Similar contraction can also be found when we compare the Os-Si bond length in compound **2** to those in silylene complexes (**Table 2**). These results also suggest a bond order higher than double for the Os-Si bond in compound **2**.

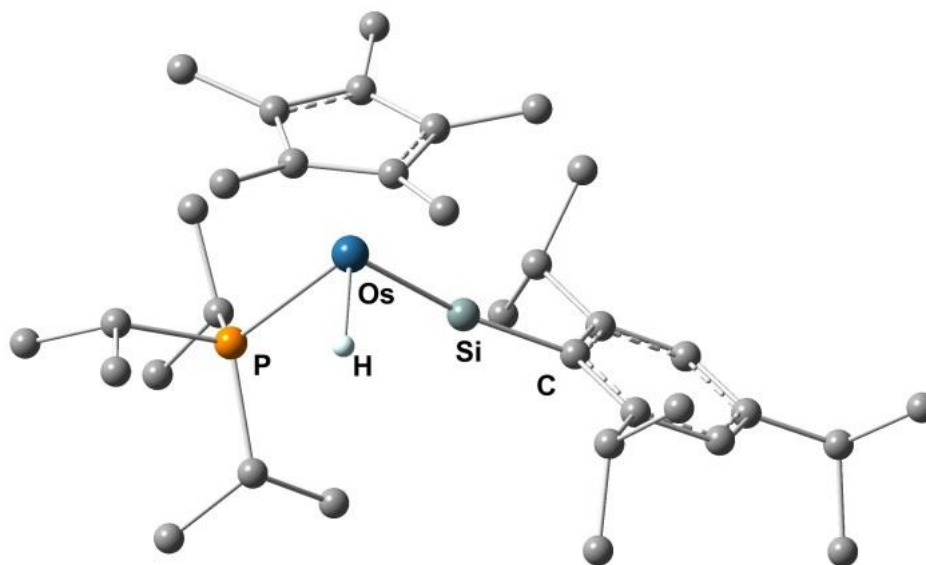


Figure 13. DFT optimized structure of **2**. All the hydrogen atoms are hidden except the hydride on the Os atom.

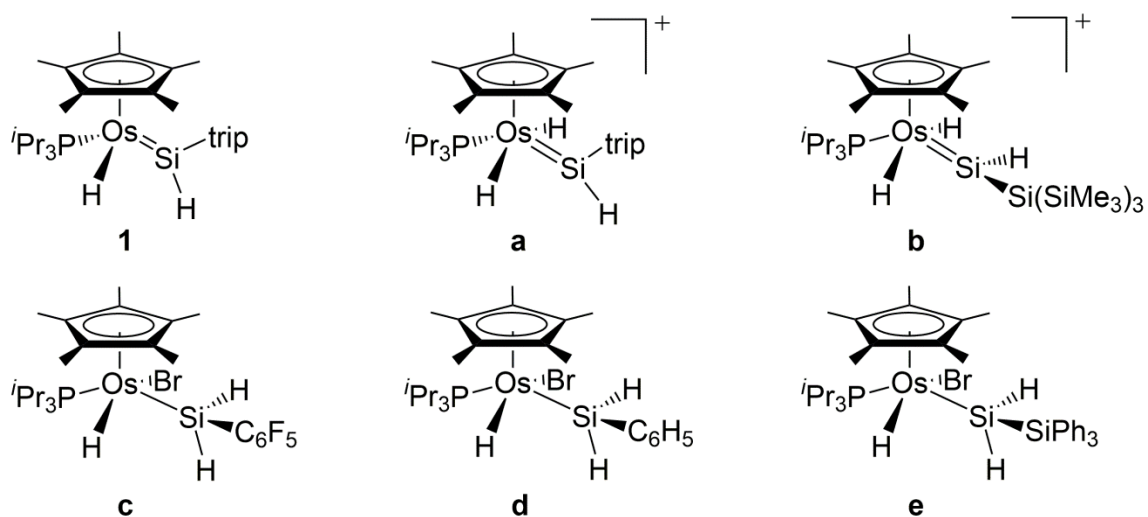


Figure 14. Some selected osmium complexes (1 - e) having the same $\text{Cp}^*(i\text{Pr}_3\text{P})\text{Os}^+$ fragment as **2**. **1**, **a** and **b** have Os=Si double bonds while **c**, **d** and **e** have Os–Si single bonds.

Table 2. The optimized bond lengths for the Os–Si bonds in several osmium species.

Species	Bond Length (Å)
2	2.176
1	2.255
a	2.289
b	2.313
c	2.426
d	2.435
e	2.442

3.4.2 Calibration in ^{29}Si chemical shift calculation

To confirm the validity of the computed structure of compound **2**, the NMR chemical shifts for these species were computed by DFT to compare with the experimental values. Firstly, we used compound **1** to test which functional is appropriate for NMR calculation. Although the computed and experimental geometries of complex **1** agree quite well, none of the functionals tested were able to reproduce the δ (^{29}Si) value of **1** (Table 3). All the data are over 30 ~ 100 ppm away from experimental value largely depending on what functional was used. Basis set effects are not quite obvious for most functionals when the basis sets are large enough for this system. These results suggest that systematic errors might exist in simulating silicon NMR for complicated complexes containing heavy transition metals by DFT. To alleviate systematic error, all of the computed NMR data were corrected by a linear calibration (Figure 15) of the computed values against known experimental ones. All the compounds shown in Figure 14 contain the $\text{Cp}^*(^i\text{Pr}_3\text{P})\text{Os}^+$ fragment, and preserve many structural similarities to **2**. Both families of osmium silyl and osmium silylene complexes were included for a more comprehensive description of the chemical environment around silicon atom. Owing to the structural similarities shared by these compounds, their theoretical versus experimental δ (Si) value plots have a nearly perfect linear correlation ($R^2 = 0.996$). This indicates the NMR data corrected by this calibration curve should be reliable. The δ (^{29}Si) value for **2** was predicted to be 309 ppm after calibration, which agrees quite well with the experimental value, 321 ppm, while the δ (^{29}Si) value of **2'** was predicted to be

282 ppm. Taken together this comparison of the NMR chemical shifts provides very strong evidence that the proposed structure complex **2** is correct.

Table 3. Silicon chemical shift values in **1** calculated by different functionals and basis sets.

		δ (^{29}Si) of 1 (ppm)	
Exp.		229	
Calc.		SDD+2f/6-311++G(2d,p) ^a	LANL2DZ+f/6-311++G(2d,p) ^a
OPBE		263	264
OLYP		271	270
M06L		274	265
TPSS		280	275
PBE		291	
BP86		293	
PW91		293	
BLYP		300	
PBE0		319	
B3LYP		326	
		SDD+2f/6-311++G(2d,p) ^a	SDD+2f/6-311++G(2df,2pd) ^a
OPBE		263	261
OLYP		271	270
TPSS		280	281

^aThe basis sets (BS) were represented as BS(metal)/BS(non-metal) in the table.

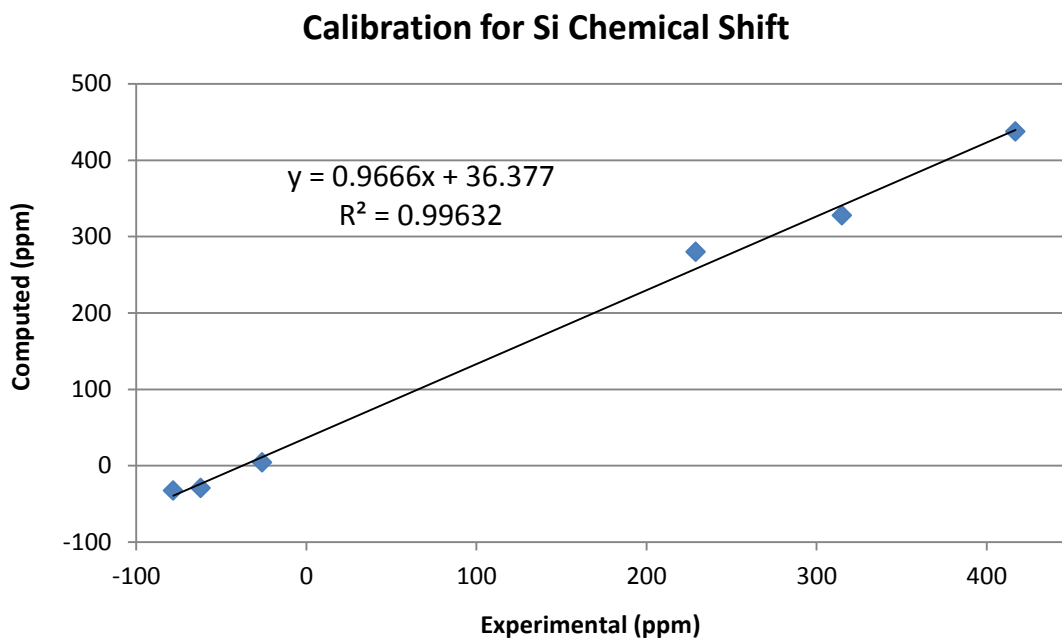


Figure 15. Experimental and computed chemical shift of Si atom in compounds **1** and **a** ~ **e** (shown in **Figure 14**). An excellent linear correlation is found between these chemical shifts for the silicon atoms, which suggests that the calculated silicon chemical shift of **2**, **3** and **4** could be corrected by this trend line to reduce the systematic error in the calculations.

3.4.3 The analysis of the Os-Si bond in **2**.

In order to understand the nature of this Os–Si bond in **2**, natural bond orbital (NBO) analysis was performed. The three strongest interactions between Os and Si consist of one σ bond and two π bonds (**Figure 16**). The σ bond has 43% osmium and 57% silicon character, so it is slightly polarized towards the silicon atom. The osmium component contains 43% *s* and 57% *d* orbital character, and the silicon component is composed by 55% *s* and 45% *p* orbital character, providing additional evidence for *sp* hybridization on silicon (**Table 4**). With the default NBO parameters, both π bonds are characterized as donor-acceptor interactions, i.e. back donations from doubly occupied Os *d* orbitals to empty Si *p* orbitals. The polarization of this bond gives rise to a highly electrophilic silicon atom with a NPA (natural population analysis) charge of 1.14.

In order to obtain a more quantitative understanding about the energetics of this bonding interaction, a combination of the extended transition state (ETS) energy decomposition scheme and the natural orbital for chemical valence (NOCV) density decomposition approach was employed to study the interactions between the two closed shell fragments: $\text{Cp}^*(i\text{Pr}_3\text{P})(\text{H})\text{Os}$ and $[\text{Si}(\text{Trip})]^+$. In the ETS decomposition scheme the two attractive interactions, the covalent interaction (also known as orbital interaction, –168.5 kcal/mol) and the electrostatic interaction (–166.1 kcal/mol), have nearly equal contributions; these attractive interactions are offset by a large Pauli repulsion (206.5 kcal/mol) (**Table 5**). The NOCV analysis reveals that the orbital interaction contains three major contributions from three *nocv* bonding orbitals (**Figure 17**). It also suggests strong π contributions to the overall orbital interactions. Such strong π interactions are

consistent with the short Os–Si bond. The high reactivity of this bond may reflect ease of polarization of the Os–Si π bonds from nearly covalent to donor-acceptor interactions.

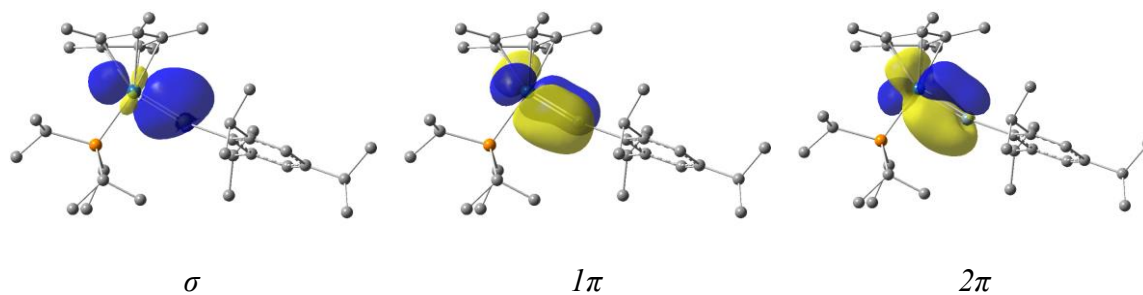


Figure 16. Three bonding interactions in compound **2** described by natural bond orbital analysis. 1π and 2π are back donations from filled osmium d orbitals to empty silicon p orbitals.

Table 4. NBO analysis of the Os-Si π bond in compound **2**.

		% s	% p	% d	Second-Order Perturbation Donor-Acceptor Interaction Energies (kcal/mol)
1π	Os (donor)	0.00	0.02	99.97	22.9
	Si (acceptor)	0.37	99.33	0.81	
2π	Os (donor)	0.13	0.05	99.82	20.8
	Si (acceptor)	0.01	99.97	0.03	

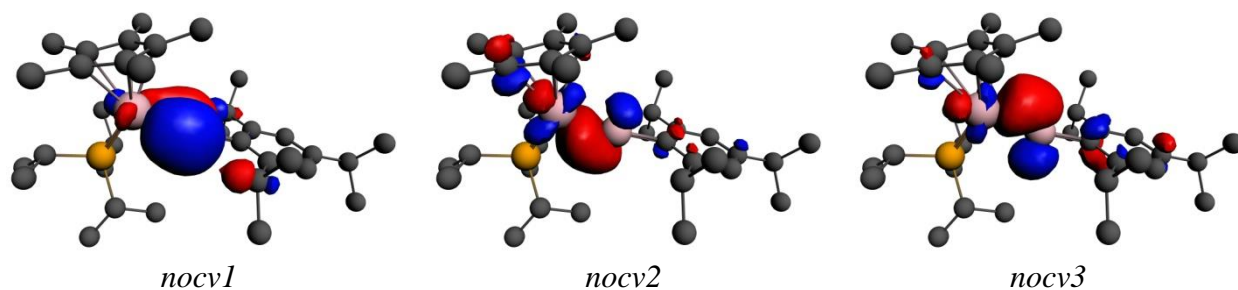


Figure 17. Three NOCV orbitals contributing the majority of the orbital interaction energies. *Nocv1* is a clean in-plane π bond, while *nocv2* and *nocv3* are mixtures of the σ bond and the out-of-plane π bond.

Table 5. ETS-NOCV results for compound **2**.

	kcal/mol
ΔE_{int}	-128.0
ΔE_{Pauli}	206.5
$\Delta E_{elestat}$	-166.1
ΔE_{ster}^a	40.4
ΔE_{orb}^b	-168.5
ΔE_{nocv1}	-58.7
ΔE_{nocv2}	-45.1
ΔE_{nocv3}	-39.7

Table 6. ^{29}Si and ^{31}P chemical shift values (ppm) for different isomers of **2**, **3** and **4**.

Species	δ (^{29}Si) (Exp.)	δ (^{29}Si) (Theo.)	δ (^{31}P) (Exp.)	δ (^{31}P) ^a (Theo.)
2	321	309		
2'		282		
3a	110	102		
3b		152		
4a	82	96	516	527
4b		157		641

^aThe P atom shown here is the one in the four-member ring instead of the one in phosphine ligand.

3.4.4 Cycloaddition products of **2**

The products of the [2+2] cycloaddition reactions, **3** and **4**, were also investigated by computations. As shown in **Figure 13**, the aromatic ring in the *trip* (2,4,6-*i*Pr₃-C₆H₂) group in compound **2** defines a plane. The small incoming reactant could approach the Os≡Si bond from above or below the *trip* plane, producing two types of isomers labeled “a” or “b” (**Figure 18** and **Figure 19**). Furthermore, this reactant could be positioned either *trans* or *cis* to the hydride on the osmium center, causing another two types of isomers of the final products (**Figure 20**). The energetics of the all-possible isomers (four for **3** and eight for **4**) are shown in **Table 7**.

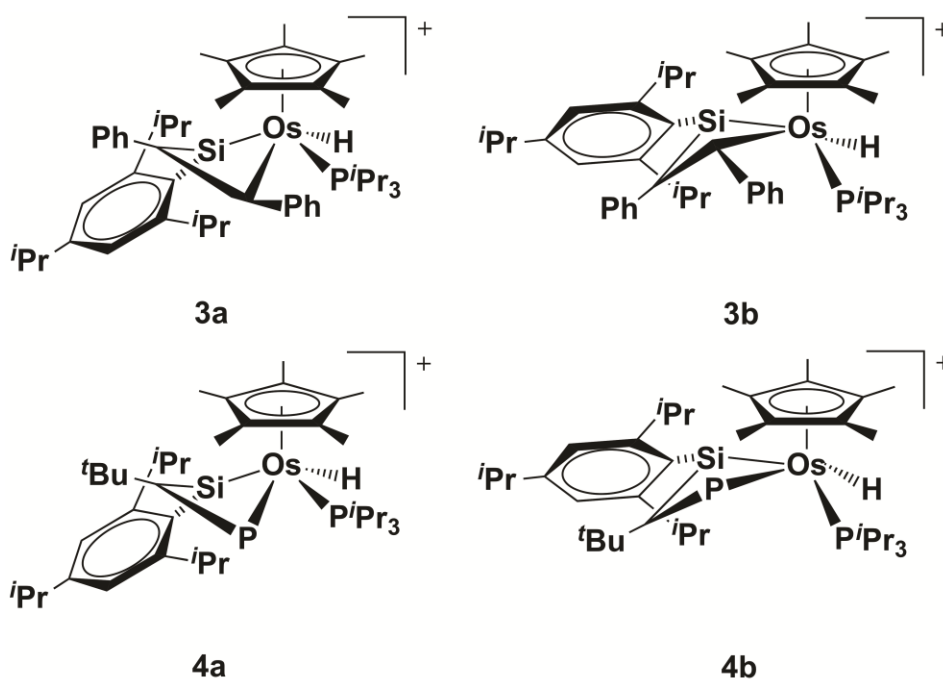


Figure 18. Structural illustrations of the [2+2] cycloaddition products. **3a** and **3b**, **4a** and **4b** are two pairs of product isomers. The isomers labeled “a” (**3a** or **4a**), have their C≡C or P≡C fragments connected to the Os≡Si bond from above the *trip* ring’s plane. Due to steric repulsions, this ring was forced to rotate and bend to a certain extent. Similarly, in isomers labeled “b”, this ring was forced to rotate in the opposite direction since the C≡C or P≡C fragments approached the Os≡Si bond from below the *trip* ring’s plane. As a consequence the four-member rings formed in the [2+2] cycloaddition are bent in opposite directions in isomers labeled “a” and “b”. All the species shown here are cations with one positive charge. Counter-ions are neglected in the computations, but solvation corrections are reported.

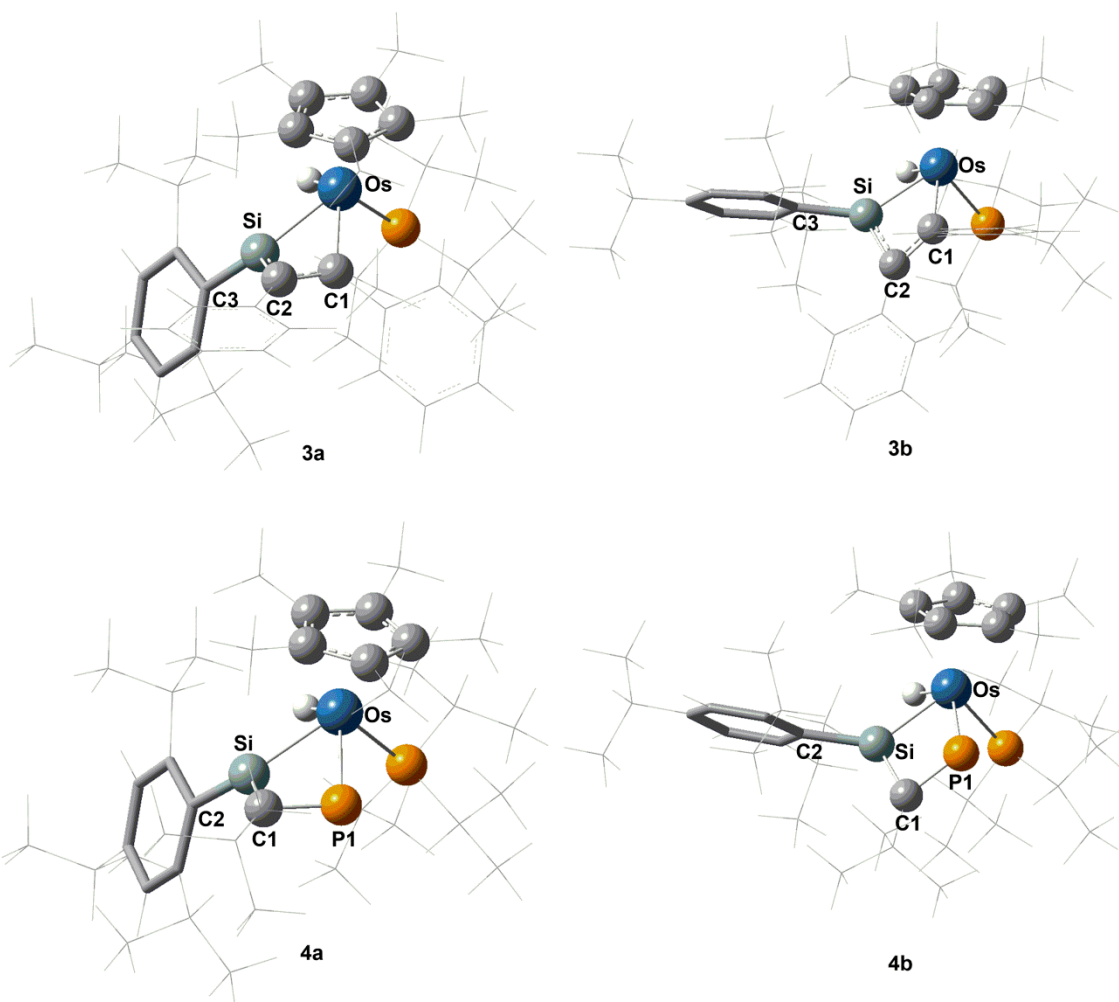


Figure 19. Optimized structure of **3a**, **3b**, **4a** and **4b**. Important bond lengths (Å) and bond angles (°): **3a**) Os-Si: 2.347, Os-C1: 2.248, C1-C2: 1.403, Si-C2: 1.817, Si-C1: 2.126, Os-Si-C3: 140.3; **3b**) Os-Si: 2.331 Os-C1: 2.203, C1-C2: 1.412, Si-C2: 1.802, Si-C1: 2.191, Os-Si-C3: 138.6; **4a**) Os-Si: 2.390, Os-P1: 2.466, C1-P1: 1.744, Si-C1: 1.844, Si-P1: 2.427, Os-Si-C2: 131.4; **4b**) Os-Si: 2.359, Os-P1: 2.426, C1-P1: 1.739, Si-C1: 1.828, Si-P1: 2.498, Os-Si-C2: 132.1.

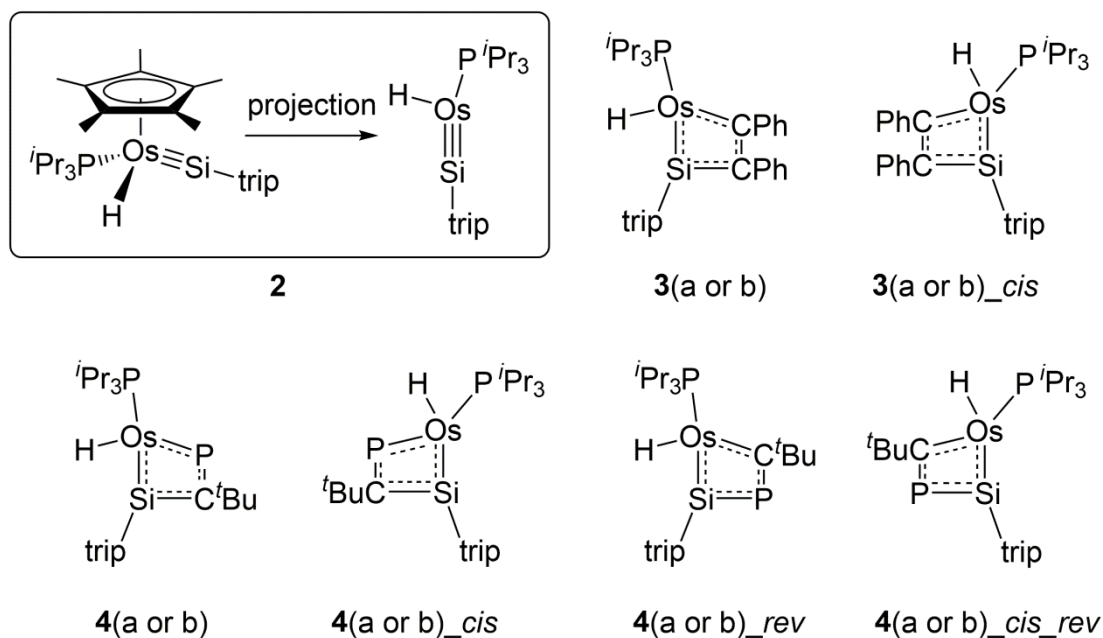


Figure 20. The projection formulas of structures of compound **2** and all the possible isomers of [2+2] cycloaddition products in question. As shown in the rectangular box, in such formulas, all the important atoms and functional groups are projected onto a plane parallel to the Cp* rings and the Cp* ring is hidden for a clearer view. Since isomers labeled “a” or “b” (these differences have been illustrated in **Figure 18** and described in the text) share the same projection formulas, each projection formula in **Figure 20** actually represent two isomers. Two additional types of isomers are illustrated here: 1) whether the PhC-CPh or P-C^tBu fragments are *trans* or *cis* relative to the hydride position (*e.g.* **3a** vs **3a_{cis}**); 2) Furthermore, two bonding patterns are possible for the P≡C bond’s cycloaddition reaction (Os bonding to P or C, *e.g.* **4a** vs **4a_{rev}**). It will be easily recognized from the figure that compound **3** and **4** have 4 and 8 isomers, respectively.

Table 7. Energetic data for all isomers of cycloaddition products^a.

Species	Activation Energies (kcal mol ⁻¹) ^b		Product Energies (kcal mol ⁻¹)	
	ΔH^\ddagger	ΔG^\ddagger	ΔH	ΔG
3a	6.9	23.9	-14.9	4.0
3b	10.9	27.9	-18.3	-1.3
3a_cis	17.8	34.7	-16.5	2.9
3b_cis	13.8	30.0	-15.5	2.9
4a	9.8	25.5	-26.8	-9.5
4b	15.0	31.1	-33.9	-16.9
4a_cis	16.7	33.4	-23.3	-3.2
4b_cis	17.0	33.4	-20.2	-2.5
4a_rev			1.9	19.7
4b_rev			-0.5	16.3
4a_cis_rev			-3.1	15.5
4b_cis_rev			1.1	18.6

^aAll the data shown in this table are relative to the total enthalpies and free energies of reactants and computed in gas phase without dispersion correction.

^bThe activation energies are the overall energy barriers for generating the corresponding products. Activation energies of the last four isomers of **4** in the table are not calculated since the products are too high in energies, so it is safely enough to rule them out from consideration.

From a careful examination of these results, we can see that only two isomers for each product need to be explored further since the other isomers are either thermodynamically or kinetically unfavorable, and thus much less likely to be formed in the cycloaddition reactions. In these two isomers the PhC≡CPh or P≡C^tBu molecule attacks the Os=Si bond from above or below the *trip* plane on the side opposite to the hydride, forming **3a**, **3b**, **4a** and **4b**, respectively. **Figure 19** shows the geometric features of these isomers. The Os-Si bond lengths in the optimized structures of **3a**, **3b**, **4a** and **4b** are 2.347 Å, 2.331 Å, 2.390 Å and 2.359 Å, respectively. These values are intermediate between typical bond lengths of Os-Si single and double bonds, suggesting the importance of the resonance shown in **Scheme 1**. The computed δ (²⁹Si) and δ (³¹P) values of **4a** are 96 ppm and 527 ppm (the P atom in the four-member ring), values quite close to the experimental ones: 82 ppm and 516 ppm. Similarly, the computed and experimental δ (²⁹Si) values of **3a** agree extremely well: 102 ppm vs. 110 ppm. The computed chemical shift for **3b** and **4b** are relatively far from the experimental results, being at least 50 ppm higher. All computed NMR data for **3a** and **4a** differ from the experimental data by less than 14 ppm (**Table 6**), a result that strongly supports the proposed structures of this group of complexes.

When the energetic data and NMR data are considered together, the [2+2] cycloaddition reactions appear to be under kinetic control. The overall barriers of both reactions are quite low with dispersion and solvation correction included (see **Figure 21**), which is consistent with the immediate color change observed in the room-temperature experiments. One might wonder if the dispersion correction over-stabilizes

the transition states and the products by a few kcal/mol, but the trend is not changed even without the dispersion correction. The experimentally observed isomers, **3a** and **4a**, are less stable than **3b** and **4b** by several kcal/mol, but the free-energy barriers for their formation are lower by a similar amount of energy. Thus, these less stable isomers, **3a** and **4a**, would be the ones trapped and detected by NMR at low temperature.

The structures of transition states leading to **3a**, **3b**, **4a** and **4b** can be found in **Figure 22**. Because the osmium center is surrounded by several bulky ligands, the expected structure for the concerted cycloaddition pathway is blocked. Instead of attacking the metal center, the C≡C triple bond donates its electron density to the electrophilic silicon center, overcoming two transition states until reaching the final product. The first transition state (**ts1_3a(b)**) is fairly similar to a σ complex, while the second transition state (**ts2_3a(b)**) has a three-member ring on either side of the phenyl ring. IRC⁶¹ calculations confirmed the characters of these transition states. The transition state keeps a close-shell character in this pathway and its wavefunction tested as being a stable singlet state. The triplet state transition states were calculated to have higher energies than the close-shell species, therefore radical pathways were eliminated from further considerations.

Only one barrier exists on the route to **4a** or **4b**. It may be because phosphorus atom has larger radius and it has interactions with both silicon and osmium atoms in the transition state, the two barriers merge into one. According to the natural population analysis of the transition states, the osmium is nucleophilic (-0.36 in **ts_4a** and -0.34 in **ts_4b**) and the phosphorus atom is electrophilic (0.51 in **ts_4a** and 0.50 in **ts_4b**). Thus,

on the ‘downhill’ side of the TSs, the strong electrostatic interaction between the osmium center and phosphorus atom pulls the incoming fragment to osmium center to form the Os-P bond (and also the four-member ring). IRC calculations confirmed that this single transition state connects the separated reactants and the final product.

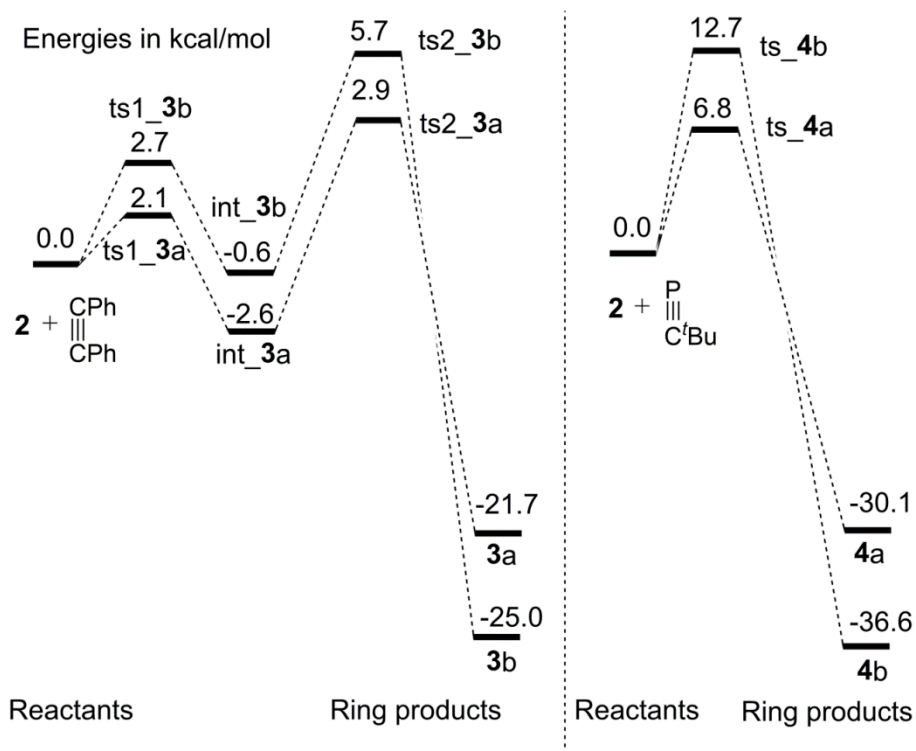


Figure 21. The Gibbs free energy profile of the [2+2] cycloaddition reaction of **2**. Dispersion and solvation correction are included here. **3a** and **4a** are the kinetic products and **3b** and **4b** are the thermodynamic products.

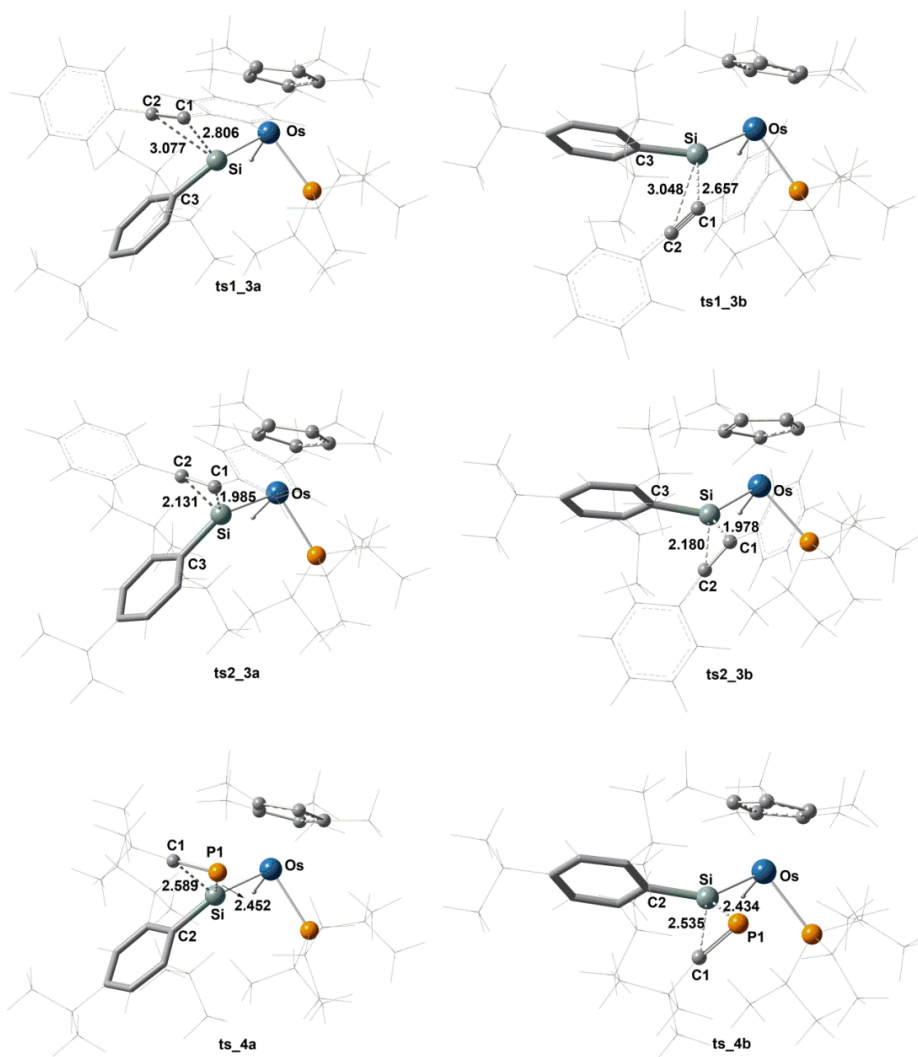


Figure 22. The optimized structure of critical transition states. Some additional geometric parameters: **ts1_3a**) Os-C1: 4.288, Os-C2: 4.709, C1-C2: 1.236, Os-Si-C3: 148.3; **ts1_3b**) Os-C1: 4.235, Os-C2: 4.929, C1-C2: 1.243, Os-Si-C3: 141.1; **ts2_3a**) Os-C1: 3.601, Os-C2: 3.952, C1-C2: 1.291, Os-Si-C3: 138.3; **ts2_3b**) Os-C1: 3.622, Os-C2: 4.148, C1-C2: 1.287, Os-Si-C3: 131.9; **ts_4a**) Os-P1: 3.710, Os-C1: 4.293, C1-P: 1.604, Os-Si-C2: 144.4; **ts_4b**) Os-P1: 3.783, Os-C1: 4.435, C1-P: 1.610, Os-Si-C2: 136.8.

3.4.5 Kinetic control of the cycloaddition reactions

To investigate the origin of the kinetic control of the cycloaddition reactions, the reactants (**2** and $t\text{Bu-C}\equiv\text{P}$) are simplified by reducing the sizes of the bulky substituents. Firstly, we replaced all the isopropyls on *trip* and the tert-butyl on $t\text{Bu-C}\equiv\text{P}$ with methyls, (**4a**^{s1} and **4b**^{s1}, see **Figure 23**). We optimized the structures of the critical species in the reactions and the results are shown in **Table 8**. The bulkier ligands destabilize both isomers of the cyclo-addition products and raise the activation barriers. Moreover, the energy differences between the isomers, **a** and **b**, are smaller both for transition states and for products when they have less bulky substituents.

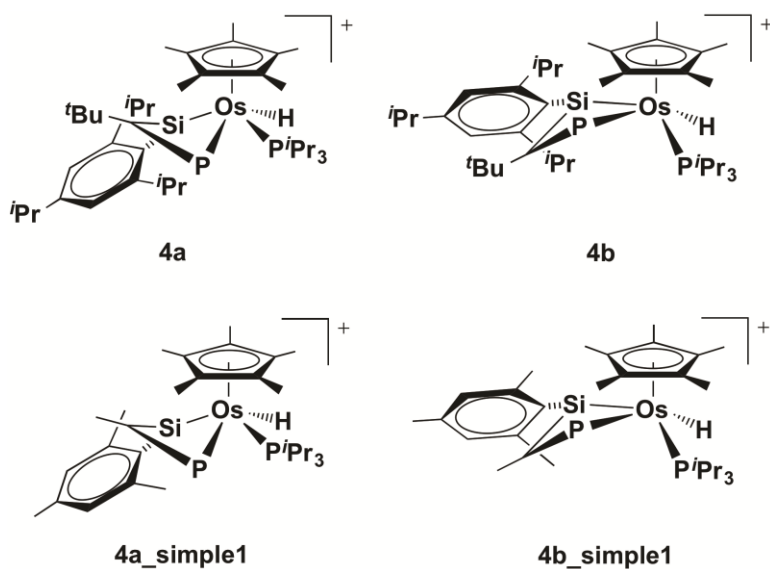


Figure 23. Full models and simplified structures for the **4a** and **4b**.

Table 8. Gas phase electronic energies of full model and simplified model for **4**.

kcal/mol	full model			simplified model		
	4a	4b	4b - 4a	4a^{s1}	4b^{s1}	4b^{s1} - 4a^{s1}
ΔE^\ddagger	9.2	14.6	5.4	1.7	4.3	2.6
ΔE	-28.7	-35.2	-6.5	-40.0	-41.7	-1.7

We can further simplify the compounds by replacing all the alkyl substituents on *trip* by hydrogen atoms. In this case, we can no longer obtain two isomers in the computation. There is only one [2+2] cycloaddition product, in which the four-membered ring is more planar such that **a** and **b** isomers merge into a single structure. These results indicate that steric effect must be an important contribution to the kinetic control.

Energy decomposition analysis (EDA) is also applied to understand the origin of the kinetic control of the cycloaddition reactions (**Table 9**). In the transition state and the final products, the twisted compound **2** (denoted as OsSi fragment) and the incoming small molecule (^tBu-C≡P or PhC≡CPh, denoted as CP fragment or CC fragment, respectively) are set as the two fragments for the EDA. For the transition states, both fragments from **ts_4b** are higher in energy than those from **ts_4a**. This difference can be partly explained by the distorted geometry of both fragments. In the OsSi fragment, the Os-Si-C2 bond angle is smaller in **ts_4b** (136.8°) than that in **ts_4a** (144.4°), which raises the energy of the OsSi fragment in **ts_4b** by 1.29 kcal/mol above that in **ts_4a**.

Similarly, in the CP fragment, the P1-C1-C(^tBu) angle is smaller in **ts_4b** (153.8 °) than that in **ts_4a** (158.1 °), which destabilizes this fragment by 1.85 kcal/mol in **ts_4b** relative to that in **ts_4a**. The difference in the interaction energies for the two fragments to form **ts_4b** and **ts_4a** is smaller (**ts_4a** is favored by 1.7 kcal/mol). Although **ts_4b** has shorter Si-P1 and Si-C1 bonds (**Figure 22**), the larger orbital and electrostatic interactions, are almost offset by the stronger Pauli repulsion. Thus, **ts_4a** is favored by both less distortion of the two fragments in the TS and stronger bonding interactions between them.

For the products, the OsSi fragment in **4b** is 7.61 kcal/mol lower than that in **4a**. This difference can also be partly understood by the shorter Os-Si bond (2.36 Å in **4b** vs. 2.39) in **4a**. Although the total bonding energy of the two fragments favors **4a** by 1.2 kcal/mol, the fragment distortion dominates the total energy and stabilizes **4b**.

Table 9. EDA analysis on the isomers of transition states and the final products of **4**.

EDA (kcal/mol)	ts_4a	ts_4b	4a	4b
OsSi_fragment	0	1.29	0	-7.61
CP_fragment	0	1.85	0	-1.22
Pauli	154.24	175.01	632.45	637.15
Elecstatic	-80.61	-90.30	-316.60	-318.59
Steric	73.63	84.71	315.86	318.56
Orbital	-88.27	-97.61	-415.13	-416.63
Total bond E	-14.64	-12.91	-99.27	-98.07
Geometry^a	ts_4a	ts_4b	4a	4b
Os-Si	2.26	2.27	2.39	2.36
P-C1	1.60	1.61	1.74	1.74
Os-P1			2.47	2.43
Si-P1	2.45	2.43		
Si-C1	2.59	2.53	1.84	1.83
P-C1-C	158.07	153.80	127.38	127.28
Os-Si-C2	144.39	136.83	131.39	132.06

^aGeometry parameters: bond length in Å and bond angel in degree.

3.4.6 Computational studies of osmium silylyne analogues

Based on the successful synthesis of the osmium silylyne compound, Tilley's group expanded the synthetic scope to other $M\equiv E$ ($M = Ru$ and Os ; $E = Si, Ge$ and Sn) compounds. However, for the similar reasons, they could not crystalize them either. So we applied the previous computation paradigm to verify the existence of these compounds.

Table 10. Computed $M\equiv E$ bond lengths.

Calculated Bond length (pm)	Si	Ge	Sn
Ru	214.8	222.4	243.7
Os	217.6	224.9	246.0

Structure optimizations show that all the $HM\equiv E$ structures are more stable than their $M=EH$ isomers by more than 10 kcal/mol. The computed lengths of $M\equiv E$ bonds in **Table 10** show two clear trends: 1) For the same metal atom, the $M\equiv E$ bond length elongated significantly from Si to Sn, which is easy to understand since the covalent radius increases dramatically from Si to Sn. 2) For the same main group atom, the $M\equiv E$ bond length only slightly increases because the covalent radius of $4d$ and $5d$ metal are very similar.

These trends can perfectly explain the differences in interactions between $[MHCp^*P(iPr)_3]$ fragment and $[E-trip]^+$ fragment. The bonding energy decreases when

the main group element is changed from Si to Sn because the bond length increases greatly. However, the bonding energy increases from Ru to Os for the same main group element. The bond length of Ru≡E and Os≡E are very similar, but Os *d* orbitals are more diffused than those of Ru, which leads to stronger orbital overlap and makes stronger bonds. This trend can also be found in bonding interaction values of these compounds. The NOCV calculation results (**Table 11**) again show that the orbital interactions of these compounds can be divided into three major contributions from three NOCV orbitals, suggesting there are M≡E triple bonds in them. An example group of NOCV orbitals are shown in **Figure 24**. Computations also compared the energies of HM≡Si and M=SiH species. All the triple bonded species are found to be favored thermodynamically (**Table 12**).

Table 11. ETS-NOCV analysis of M≡E triple bonds (M = Os and Ru, E = Si, Ge, Sn).

ETS results (kcal/mol)	OsSi	OsGe	OsSn	RuSi	RuGe	RuSn
Pauli repulsion	206.5	178.4	149.4	179.5	153.8	129.6
Elastic interaction	-166.1	-143.7	-125.1	-140.7	-121.1	-106.8
Steric interaction	40.4	34.8	24.3	38.9	32.7	22.7
Orbital interaction	-168.5	-150.1	-120.7	-150.8	-133.6	-107.7
Bonding interaction	-128.0	-115.4	-96.4	-111.9	-100.9	-85.0
NOCV orbital energies (kcal/mol)						
1	-58.7	-52.7	-41.6	-54.2	-48.8	-39.3
2	-45.1	-39.2	-32.5	-37.8	-33.3	-26.6
3	-39.7	-35.5	-28.3	-35.4	-30.5	-24.4

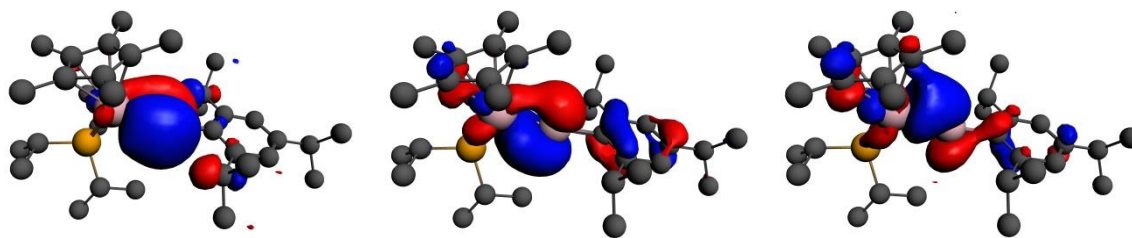


Figure 24. NOCV orbitals of osmium germylyne compound.

Table 12. The gas phase free energy differences between double bond species (M=EH) and their triple bond isomers (HM≡E). ($\Delta\Delta G = \Delta G(\text{M=EH}) - \Delta G(\text{HM}\equiv\text{E})$).

	RuSi	RuGe	RuSn	OsSi	OsGe	OsSn
$\Delta\Delta G$ (kcal/mol)	11.2	16.8	16.5	15.8	21.6	19.9

3.5 Conclusion

In this collaborating work, Tilley's group synthesized a novel compound ($[\text{Cp}^*(\text{Pr}_3\text{P})(\text{H})\text{Os}\equiv\text{Si}(\text{Trip})][\text{HB}(\text{C}_6\text{F}_5)_3]$, Trip = 2, 4, 6-tris(isopropyl)phenyl, **2**) via a new route involving hydride abstraction from silicon. The compound is not thermally stable thus its structure could not be determined crystallographically. NMR and DFT computations helped to validate the proposed structure of this complex: the hydride is on the metal center instead of silicon atom. NBO and ETS-NOCV analysis revealed the nature of this Os–Si bond as a triple bond consisting of a covalent σ bond and two strong π back-donations.

Significantly, the discovery of complex **2** has allowed the exploration of new reactivity for a metal-silicon triple bond. In particular, the cyclo-additions of multiple

bonds portend a rich chemical reactivity for $L_nM\equiv ER$ species. From the computational results, the reaction barriers are very low, consistent with the immediate color change under room temperature found in the experiments. The reaction does not follow simple concerted addition mechanism because the osmium center is surrounded by bulky ligands. Thus for $\text{PhC}\equiv\text{CPh}$ there are two transition states and an intermediate, while only a single transition state for ${}^t\text{BuC}\equiv\text{P}$ has strong Si-P interactions and weak P-Os interactions. The electrophilic silicon center facilitates the mechanism by accepting the electron density of the π bond of the small incoming molecules. The electron transfer makes the $\text{PhC}\equiv\text{CPh}$ or ${}^t\text{BuC}\equiv\text{P}$ more electrophilic and the osmium center more nucleophilic. The Os atom then attacks the $\text{PhC}\equiv\text{CPh}$ or ${}^t\text{BuC}\equiv\text{P}$ as a nucleophile to finally form the four-membered ring product.

The cycloaddition reactions are found to be under kinetic control as **3b** and **4b** are more stable products but their isomers **3a** and **4a** are detected by NMR. Computations predict that the barriers leading to **3a** and **4a** are significantly lower than those leading to **3b** and **4b**. Further analysis indicates the interplay between steric effects and bonding interactions of the two reacting fragments is the major reason for the kinetic control.

CHAPTER IV
COMPUTATIONAL PREDICTION OF INDUCTIVE EFFECTS THAT CAUSE A
CHANGE IN THE RATE-DETERMINING STEP FOR THE CONVERSION OF
RHENIUM AZIDES TO IMIDO COMPLEXES*

4.1 Introduction

Organic azides, RN_3 , were used extensively in synthetic chemistry.⁶² Because they can easily release N_2 molecules and produce reactive nitrene radicals, they receive great attention in trapping and/or transferring nitrene fragments for transformations such as amination⁶³ and aziridination.⁶⁴ In many reactions developed so far, nitrene transfer is catalyzed by transition metal complexes and in most cases the transition metal-azide compounds are proposed as the key intermediates in the azide activation. Metal imido $[M=NR]$ compounds are also involved in the nitrene transfer reactions as important intermediates. The reactive site of organic azides is the linear NNN moiety, which possesses zwitterionic character. Two resonance forms delocalizing negative charge between N_α and N_γ can be envisaged (**Figure 25**). The bond orders for $N_\alpha-N_\beta$ and $N_\beta-N_\gamma$ are approximately 1.5 and 2.5, respectively (bond lengths of 1.24 and 1.13 Å for HN_3).⁶⁵ The N_α is more basic and is therefore the most likely donate electrons density to an electron-poor metal center by forming $M-N_\alpha$ bond.

*Reprinted (adapted) with permission from Travia, N. E.; Xu, Z.; Keith, J. M.; Ison, E. A.; Fanwick, P. E.; Hall, M. B.; Abu-Omar, M. M. *Inorg. Chem.* **2011**, *50*, 10505. Copyright 2011 American Chemical Society.

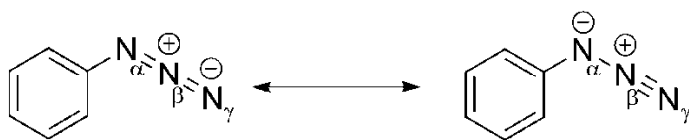


Figure 25. Resonance forms of phenyl azide.

Except for the α -N bonding mode, organo-azide can bind to transition metal center in a variety of ways and some reported bonding patterns⁶⁶ were shown in **Figure 26**. The reaction of organic azides with transition metal complexes can lead to transition metal imido compounds and several reaction mechanisms have been proposed. In 1967, Kwart and Khan observed N_2 -evolution from benzyldisulfonyl azide stirred over copper powder and tentatively proposed a metallocycle intermediate in which copper is coordinated to both N_α and N_γ of the azide.⁶⁷ Later, the Lewis acid catalyzed ($AlCl_3$) rearrangement of 1-azidoadamantane was proposed to proceed by Al coordination to N_α only.⁶⁸ Osborne and Trogler provided mechanistic insight by preparing exclusively $(Cp^*)_2V^{15}NPh$ from a labeled phenyl azide ($Ph^{15}NNN$). They proposed a short-lived intermediate whereby PhN_3 coordinates to vanadium through the labeled N_α to give an η^1 -diazoamine complex (**Figure 26-b**)⁶⁹. Density Functional Theory (DFT) computations strongly suggested that Cu and Ru catalyzed 1, 3-dipolar cycloaddition to alkynes proceeds through a similar η^1 -diazoamine coordination to the metal alkynyl.⁷⁰ Alternatively, $Cp_2TaMe(N_3Ar)$ and $Cp_2Zr-(\mu-N^tBu)(\mu-N_3Ph)-IrCp^*$ have been suggested to decompose through anti/syn isomerization of the initial diazenimido (**Figure 26-d**) followed by attack of N_α onto the metal to form a four-member

tetraazametallocyclobutene intermediate.⁷¹ Computational studies demonstrated that both types of intermediates (azametallocycle and diazoamine) are available for the imide formation from (dtbpe)Ni(η^2 -N₃R), but a highly negative entropy of activation was more consistent with the four-member ring azametallocycle pathway.⁷²

Cationic rhenium(VII) oxo imido complexes of salen, saldach, and *bis*(oxazoline) ligand architectures were recently prepared by Abu-Omar's group via the reaction of aryl azides with mononuclear cationic oxorhenium(V) complexes.⁷³ The reaction proceeds cleanly at room temperature and features reproducible kinetics with first-order dependence in both Re and azide. Drawing from other d^2 examples, Abu-Omar's group tentatively assigned a mechanism whereby the aryl azide coordinates via the terminal N_γ before proceeding through an azametallocycle analogous to the mechanism described by Bergman for Cp₂TaMe(N₃Ar).⁷¹ Recently, our group offered an alternative mechanism based on DFT computations. The organic azide binds rhenium through the internal N_α to give a η^1 -diazoamine intermediate, which extrudes N₂ directly.⁷⁴ These computations showed that while a tetraazametallocyclobutene intermediate was accessible for the Ta complex of Bergman, a prohibitive activation barrier (>50 kcal/mol) was required for the cationic oxorhenium(V) salen complex. In comparison, the activation energy for direct N₂ extrusion is only 13 kcal/mol.

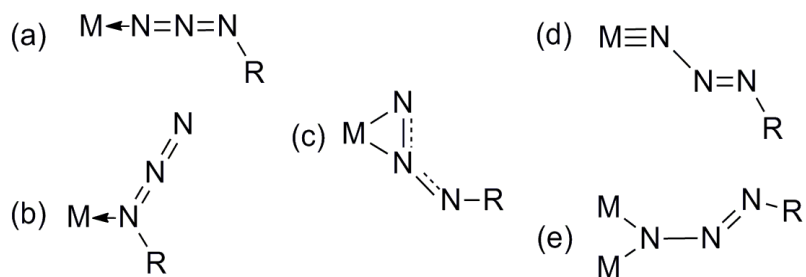


Figure 26. Coordination modes of organic azides. (a) terminal azide nitrogen (N_γ) complexation, (b) coordination through N_α , (c) η^2 -adduct analogue of olefin complexation, (d) diazenimido, and (e) bridging μ -imido ligation.

In this collaborating work, we clarify the mechanism of azide reaction with $[\text{Re}(\text{O})(\text{hoz})_2(\text{CH}_3\text{CN})][\text{B}(\text{C}_6\text{F}_5)_3]$ (Hhoz = 2-(2'-hydroxyphenyl)-2-oxazolinine), **1** (**Figure 27**), by DFT calculations. Detailed kinetic analysis from experiments suggested the reaction is indeed first-order in Re and in azide for a variety of electronically substituted aryl azides over a wide range of concentrations. Moreover, Hammett ρ/σ analysis revealed a drastic change in electronic effect between electron-donating and electron-withdrawing aryl substitutions. Our calculation results described herein predict a multi-step mechanism which perfectly explains the rate change. This mechanism involves: (1) isomerization of **1**, (2) attack of the azide, (3) N_2 extrusion, and (4) rearrangement of the product, with steps (2) and (3) being rate-determining for electron-donating and electron-withdrawing substituents, respectively.

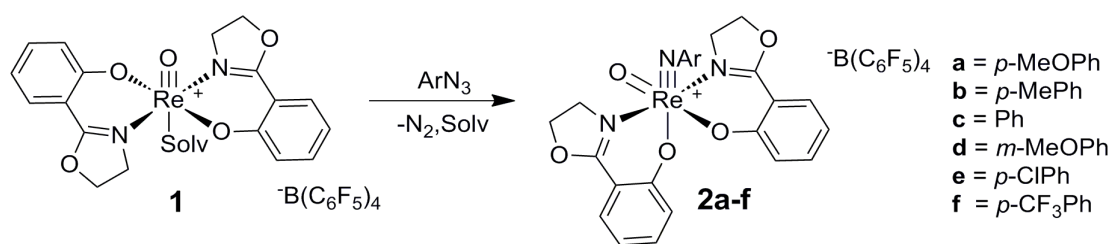


Figure 27. Formation of Re(VII) oxo imido complexes. A series of substituted Ar groups (**a ~ f**) are involved in the reactions.

4.2 Experimental observations

The reaction of **1** with excess ArN₃ in CH₃CN or CH₂Cl₂ gave a change in color from green to intense red, corresponding to a change in oxidation state from Re(V) to Re(VII).⁷³ A series of products, **2a-f** (**Figure 27**), were isolated and recovered in high yields, characterized to be the oxo imido complexes by ESI-mass spectrometry, and confirmed to be pure by ¹H NMR.⁷⁵

The kinetics of formation of **2** in CH₃CN are first-order in both azide (N₃Ar) and oxorhenium(V) complex **1**. The rate law can be written as $d[\mathbf{2}]/dt = k[\text{X-PhN}_3][\mathbf{1}]$. The Hammett ρ/σ analysis is used to evaluate the inductive effect that different substituents on the aryl azides have on the reaction rate (**Figure 28**).⁷⁶ A strong inductive effect is observed for electron-withdrawing substituents resulting a negative Hammett reaction constant $\rho = -1.3$. However, electron-donating substituents on phenyl azide deviate significantly from this trend. From detailed experimental data, the enthalpic barriers (ΔH^\ddagger) calculated from the Eyring-Polanyi equation are within the range of 14-19 kcal mol⁻¹ for all six aryl azides. With respect to activation entropy, electron-donating 4-methoxyphenyl azide shows a large negative value, $\Delta S^\ddagger = -21 \text{ cal mol}^{-1} \text{ K}^{-1}$, which is very different to the near zero ΔS^\ddagger observed for phenyl azide and 4-trifluoromethylphenyl azide. The Hammett linear free energy relationship and the activation parameters suggest a mechanism change between electron-withdrawing and electron-donating aryl azides. The initial mechanistic hypothesis was: 1) electron-withdrawing azides favor direct N₂ extrusion mechanism, because those azides favor the resonance structures with negative charges on the internal α -N; electron-donating azides

favor the Bergman's mechanism, in which the terminal γ -N firstly binds to Re center then goes a Re-N-N-N four-member-ring transition states, because those azides favor the resonance structures with negative charges on the terminal γ -N.

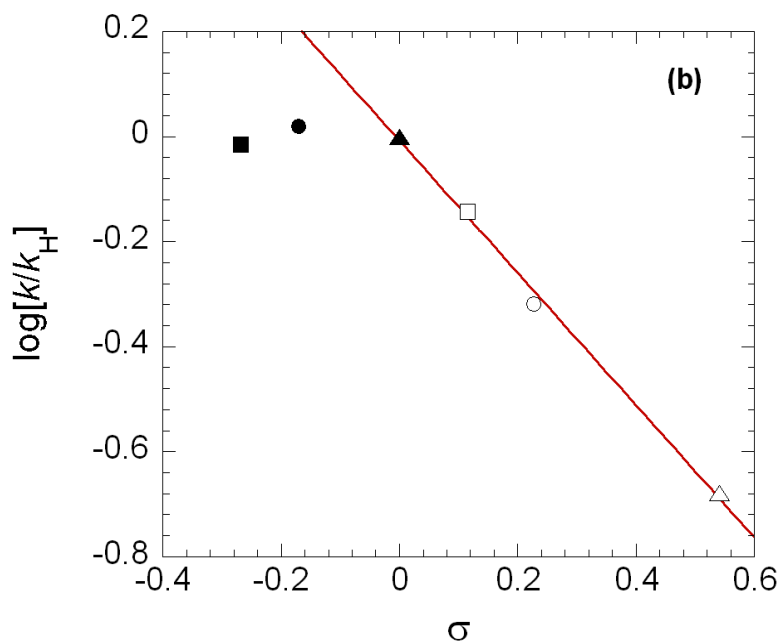


Figure 28. Hammett plot for aryl azides with different substituents. Reaction rates of rhenium imido compounds show linear relationship on the σ value of electron-withdrawing substituents. Reactions involving azides with electron-donating substituents deviate significantly from this trend. Key: \blacksquare p -MeO, \bullet p -Me, \blacktriangle H, \square m -MeO, \circ p -Cl, and Δ p -CF₃.

4.3 Computational details

4.3.1 General procedure

All the geometry optimization and frequency determinations were performed with the Gaussian 09 package of programs⁴⁸ at the B3LYP⁷⁷ level. Transition states were located with the use of synchronous transit guided, quasi-Newton method.⁷⁸ The basis set used for rhenium is the effective-core potential, extended valence double-zeta LANL2DZ⁷⁹ basis, in which the 6p functions were replaced by the re-optimized functions of Couty and Hall,⁸⁰ and a set of diffuse f functions (exponent = 0.869) were added.⁸¹ The 6-31G** basis sets were used for all hydrogen, carbon, nitrogen, oxygen, chlorine and fluorine atoms.⁸² Solvation energies were obtained from single-point calculations on gas-phase geometries by applying the SMD solvation model⁸³ for acetonitrile with default radii and non-electrostatic terms. The 3D molecular structures were drawn by the JIMP2 program.⁸⁴

4.3.2 The estimation of free energy values of TS_2s

Due to the difficulties encountered in locating the transition states **TS_2**, a scheme was applied to estimate the barriers from enthalpy/entropy changes. A potential surface scan was carried out by freezing various Re-N bond lengths (**Figure 29**). Almost all the curves have flat plateaus when the bond lengths are longer than 4 Å, which indicates the transition states should have bond lengths ranging from 4.2 Å to 5 Å. In this case, the enthalpies changes from reactants to transition states can be neglected. The barriers in free energies just came from entropy losses in the formation of the intermediate **3_α**: $\Delta G_{gas} = -T\Delta S_{gas}$ [$\Delta S = S(\text{azide}) + S(\mathbf{1}_{cis}) - S(\mathbf{3}_{\alpha})$]. For solvent

correction, we calculated the average correction for three cases in which Re-N bond lengths are 4.2 Å, 4.6 Å and 5.0 Å, respectively. In this way we obtained the estimated free energy value for all TS_2s.

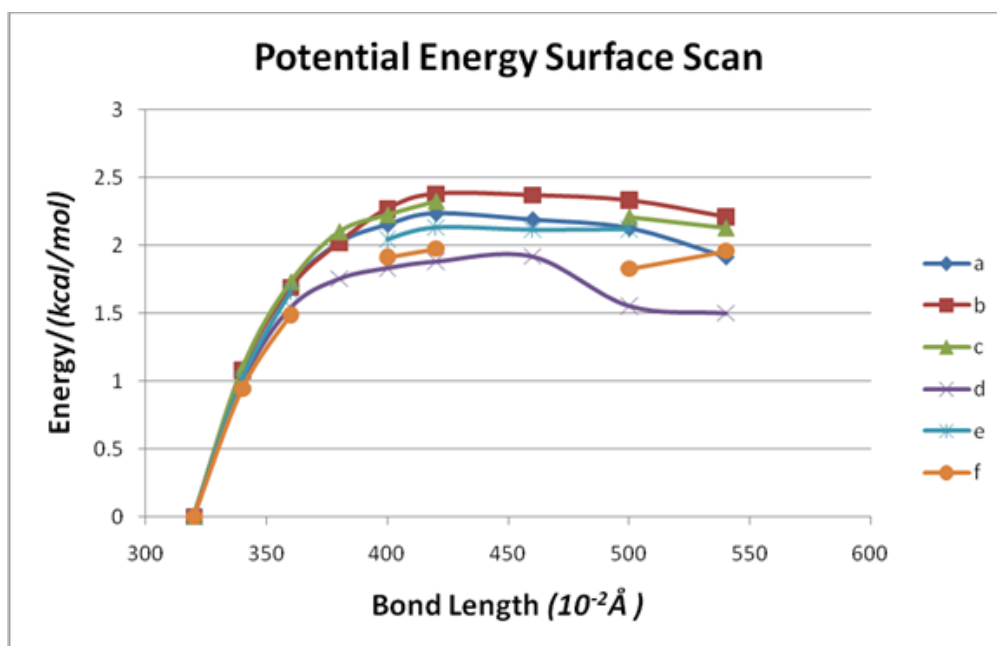


Figure 29. The potential energy surface scanning of the Re-N bond length elongated from the intermediate for different substituted azides.

4.4 Computational results and discussion

4.4.1 Computational characterization of 2a

At the very beginning, the structure of the experimentally determined product, $[\text{Re}(\text{O})(p\text{-MeOPhN})(\text{hoz})_2]$ (**2a**, see **Figure 30**), was optimized as described above, and some selected bond lengths and angles are compared to those of the crystal structure (**Table 13**). The agreement is fairly good with the largest error in bond lengths being 0.02 Å, while the largest angular errors occur for C31-N3-Re and the C31-N3-Re-O33 dihedral angle. Optimizing the structure of this product with other functionals yielded similar values for these two angles (**Table 14**). One might attribute these angular differences to packing effects within the crystal as our structures are optimized in the gas phase. It also indicates that our choice of computational model is appropriate for geometry optimization.

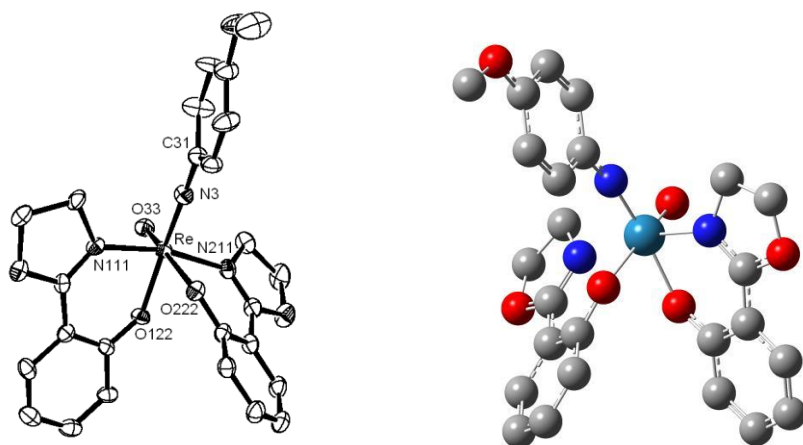


Figure 30. The crystal structure (left) and computational optimized structure (right) of **2a** with H atoms omitted.

Table 13. Comparison between crystal structure and computed structure for selected bond lengths (Å) and angles (degree) for **2a**.

	Exp	Calc		Exp	Calc
Re-O33	1.716	1.699	C31-N3-Re	168.2	160.9
Re-N3	1.763	1.772	O33-Re-N3	101.7	101.8
Re-O122	2.016	2.015	O33-Re-O122	89.5	91.0
Re-O222	2.024	2.028	N3-Re-O122	168.4	167.0
Re-N111	2.081	2.075	O33-Re-O222	164.9	164.2
Re-N211	2.103	2.124	N3-Re-O222	88.8	88.3
			O122-Re-O222	80.8	79.8
			O33-Re-N111	99.7	99.6
			C31-N3-Re-O33	152.4	173.1
			N3-Re-N111	90.2	91.2
			O122-Re-N111	84.9	84.2
			O222-Re-N111	91.1	92.3
			O33-Re-N211	86.7	86.3
			N3-Re-N211	99.2	97.1
			O122-Re-N211	84.3	86.0
			O222-Re-N211	80.9	80.3
			N111-Re-N211	167.4	168.6

Table 14. Selected structural data of **2a** obtained from X-ray and computed by different functionals.

	C31-N3_Re-O33	C31-N3-Re
Exp.	152.40	168.2(6)
b3p86	172.14	159.74
b3pw91	172.16	161.72
blyp	170.49	162.32
bp86	170.15	160.85
m06l	168.97	159.45
pbe1pbe	172.15	159.74
pw91pw91	169.95	159.82
tpsstpss	170.60	161.38
b3lyp	173.06	160.91

The ligands around Re center in **2a** have a distorted octahedral geometry. The Re imido bond angle is calculated as 161° which is close to linear. The Re-imido and Re-oxo bond lengths are calculated to be 1.77 and 1.70 Å, which are within the typical length range of Re-heteroatom multiple bond.⁸⁵ Because the oxo and imido ligands are both *trans* to Re-O single bonds, the trans influence elongates those Re-O bonds (was 1.968 Å in reactant **1**) to 2.028 Å (*trans* to oxo) and 2.015 Å (*trans* to imido).

4.4.2 Isomers of reactants, intermediates and products

All reactions starts from the attacking of an azide molecule on Re(V) reactant **1**. In this step the azide kicks the solvent molecule away and binds the rhenium center to form intermediate **3**. There are two possible modes generating intermediates **3_α** and **3_γ** (**Figure 31**), respectively. **3_γ** is lower in energy than **3_α**, in part because of steric crowding in **3_α**. As described in previous work, the four-member ring species proposed in Bergman's mechanism, where the N_α in **3_γ** bends over and also binds to the metal before losing N₂, is highly unfavorable in energy ($\Delta G^{\ddagger}_{sol} > 50$ kcal/mol) because the 7-coordinate species is both sterically crowded and a 20 e⁻ species if it maintains the Re=O bond. Thus, Bergman's mechanism is very unlikely for this system, but is viable with coordinatively and electronically unsaturated early metals. Here, the α-bonding intermediate, which extrudes N₂ directly via the previously proposed mechanism dominates the reaction.

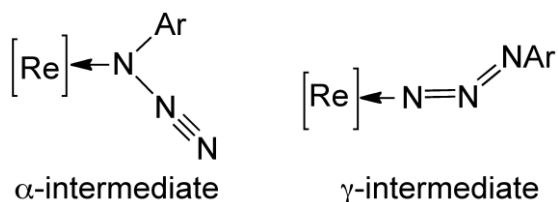


Figure 31. α- and γ- intermediates of rhenium azide compounds.

Although the structures of the reactant and other products have not been determined, all possible isomers for reactant **1** and the simplest product **2c** were then optimized. The reactant **1** (without solvent molecule) has two isomers, for which the two

equatorial oxazoline nitrogens occupy *trans* and *cis* positions, **1_{trans}** and **1_{cis}** (**Figure 32**). Due to the repulsion between the hydrogen atoms on the two nitrogen atoms in **1_{cis}**, the ligands in the equatorial plane adopt a twisted conformation that contributes to making **1_{cis}** higher in free energy than **1_{trans}** by 8.5 kcal/mol.

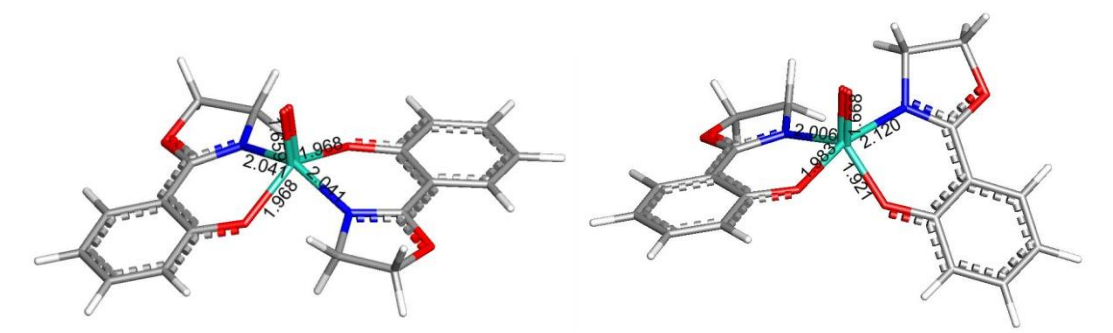


Figure 32. Structures and some selected bonds lengths of **1_{trans}** (left) and **1_{cis}** (right). The ligands lying in the equatorial plane are relatively flat in **1_{trans}**, while fairly twisted in **1_{cis}**.

The imido product **2** from the reaction between **1** and an azide could exist in six possible isomers (**2_{iso1-6}**, see **Figure 33**). The reaction energies for the formation of **2c_{iso1-6}** (see **Figure 33**) can be rationalized to some extent by the *trans* influence. The oxo-Re triple bond uses the d_z , d_{xz} and d_{yz} orbitals of Re, so it is particularly difficult for the imido nitrogen to bond *trans* to oxo, so **2c_{iso1}** and **2c_{iso4}** are significantly higher in energy than the other isomers. Because the alkoxide O to Re bond has more ionic character than imine coordination to Re bond, among the other four isomers, the ones with O *trans* to oxo (**2c_{iso3}** and **2c_{iso6}**) are more stable than those with N *trans* to

oxo (**2c_iso2** and **2c_iso5**). However, the energies of these four isomers, and particularly the two most stable ones, are quite close. Because the differences are so small the preferred arrangement of ligands in these isomers may be influenced by aspects other than the *trans* influence.

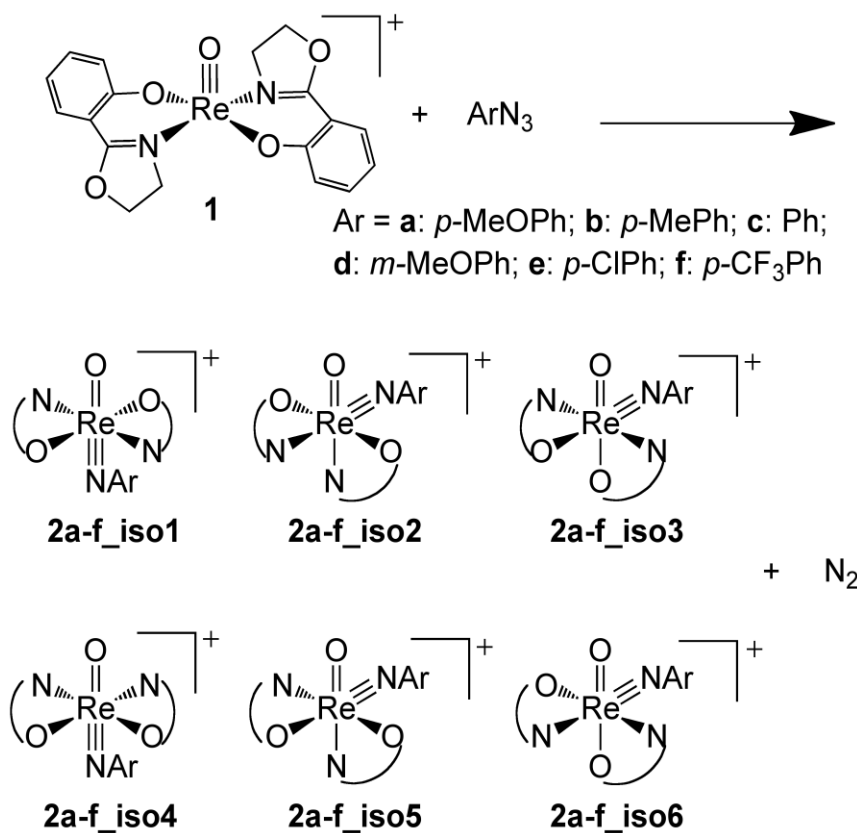


Figure 33. Different isomers of product **2a-f**.

Table 15. Reaction energies for different isomers of **2c** relative to **1_{trans}** + PhN₃ (kcal/mol).

	2c_iso1	2c_iso2	2c_iso3	2c_iso4	2c_iso5	2c_iso6
ΔE_{elec}^{a1}	-18.86	-44.73	-47.42	-19.22	-39.76	-46.76
ΔH^{a2}	-19.65	-45.49	-48.06	-20.07	-40.54	-47.43
ΔG_{gas}^{a3}	-17.62	-45.65	-46.42	-18.82	-39.52	-46.61
ΔG_{sol}^{a4}	-13.20	-39.97	-40.83	-14.00	-37.85	-41.20
$\Delta G_{sol}^{\ddagger b}$	42.15	29.59	32.63	46.13	33.27	24.30

^a Electronic energies (a1), enthalpy (a2), gas phase free energies (a3) and solvated free energies (a4) of reactions leading to different isomers of product. All energies are relative to initial reactants **1** and PhN₃.

^b The free-energy barriers for elimination of N₂ in different pathways to form **2c_iso1-6** relative to initial reactants **1** and PhN₃.

The similarity in the relative energies for two most stable isomers **2_iso3** and **2_iso6** seen above for **2c** is true for all the products **a** through **f** (see **Table 16**). The **2_iso3** isomers are lower in electronic energy than the **2_iso6** isomers for all 6 substituents. The crystal structure obtained for **2a** corresponds to the computed structure **2a_iso3**, an observation which suggests that the final products prefer the **iso3** structure. On the other hand, the computational results predict that **2_iso6** isomers have lower solvated free energies than **2_iso3** isomers for all species except **2f**. However, since all

the energy differences between the two isomers for each product are less than 1.0 kcal/mol, the calculations are most likely too inaccurate to trust these subtle energy differences (different functional produce similar results see **Table 17**). Because the number of approximations involved, such as the harmonic approximation for vibrational frequencies and implicit solvation model, increase for the calculation of H and G_{sol} , the electronic energy differences may more accurately reflect the preferred solid-state structure. Thus, we will assume that **2_iso3** isomers represent the final products in accordance with experiment. The energy barriers for the rearrangement between isomers **2_iso6** and **2_iso3** are computed to be ~ 24 kcal/mol (see **Figure 34**). Thus, their rearrangement could occur at room temperature; furthermore, the alternative final product does not influence the rate of the reaction for the mechanism described below as this rearrangement would occur after formation of the very stable products.

Table 16. Comparisons of energy between **iso3** and **iso6** for **2a-f** (kcal/mol).

	iso6 – iso3					
	2a	2b	2c	2d	2e	2f
ΔE_{elec}	0.48	0.61	0.66	0.70	0.68	0.77
ΔH	0.46	0.54	0.63	0.64	0.61	0.70
ΔG_{gas}	-0.13	-0.27	-0.19	-0.09	-0.26	0.39
ΔG_{sol}	-0.11	-0.37	-0.37	-0.21	-0.40	0.15

Table 17. Results of energies differences^a between **2c_iso6** and **2c_iso3**.

	b3lyp	bp86	m06l	pw91	tpss
ΔE	0.67	1.15	1.27	1.33	0.86
ΔH	0.63	1.11	1.12	1.28	0.81
ΔG_{gas}	-0.19	0.38	0.26	0.69	0.20

^aEnergy difference is defined as $\Delta E = E(\mathbf{2c_iso6}) - E(\mathbf{2c_iso3})$. All results from different functionals show that the energies of **2c_iso6** and **2c_iso3** are quite close.

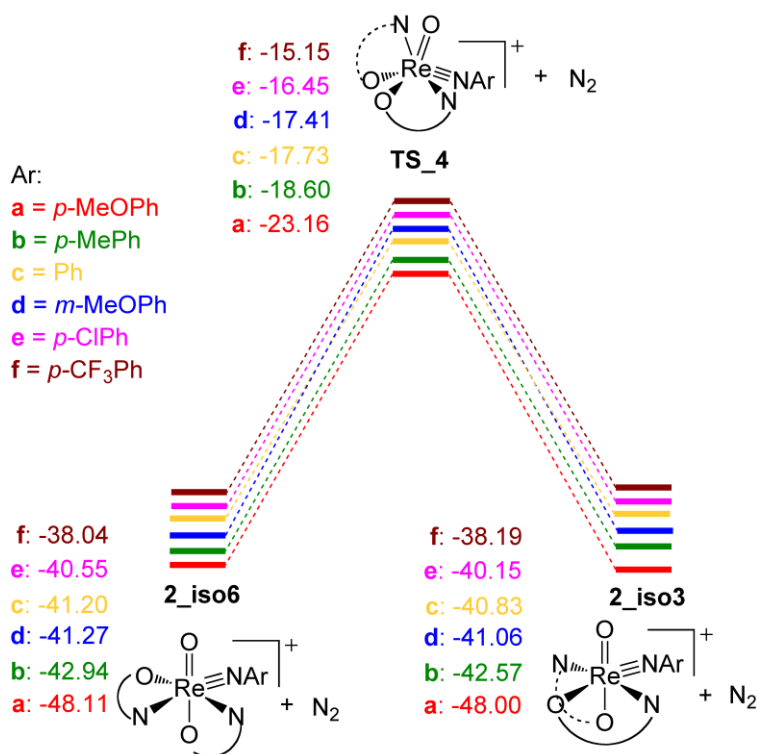


Figure 34. The rearrangement between **2_iso6** and **2_iso3**.

4.4.3 Descriptions of the reaction pathway

In the reaction examined here, the reactant, **1**, firstly binds an azide molecule to form intermediate **3_α**, which then extrudes N₂ directly to yield the desired product, **2**. Since several different isomers of the intermediates and products need to be considered, we will refer to the paths to each of the various isomeric products by using the isomer label of the product. For example, path 6 is the reaction path from **1** + azide to the one of the products **2_iso6**. We begin by noting that in paths 1 through 3 (1-3), **1_trans** can directly bind an azide to form **3_α_iso1-3**, while in paths 4-6, **1_trans** isomerizes to **1_cis** before coordinating an azide molecule. The results in **Table 15** show that the lowest free-energy barrier, ΔG_{sol}^\ddagger , between **1** + azide and **2c** exists in path 6; indicating path 6 is the most probable. Although the next highest barrier (path 2) is only ~5 kcal/mol higher, DFT energy differences for the barriers of these two very similar steps, extruding N₂, should be accurate enough to eliminate all paths but path 6 from further consideration as the experimental ΔG^\ddagger span a range of only 2 kcal/mol.

A detailed free-energy profile for the reaction between all 6 substituted azides through path 6 is shown in **Figure 35**. The formation of the initial product, **2_iso6a-f**, has three important barriers that are somewhat similar in their overall free-energy (**TS-1**, **TS-2**, **TS-3**) with respect to the reactants, **1_trans** + azide. These transition states correspond to: **TS-1**, the **1_trans** to **1_cis** isomerization, which is necessary to access the lowest energy path for the remainder of the reaction (path 6), **TS-2**, the attack of the azide on **1_cis**, which distorts to accommodate the incoming azide, and **TS-3**, the extrusion of N₂ to form the product. Since the two intermediates, **1_cis** + azide and

3_α_iso6, are similarly less stable than the reactant, **1_trans** + azide, and since the product is much more stable, the rate-determining step should correspond to the highest point on the free-energy profile displayed in **Figure 35**. As **TS-1** is always lower in energy than the rate-determining step, which varies between **TS-2** or **TS-3** depending on the azide, the isomerization of the reactant never serves as a rate-determining step in the reactions. Thus, in agreement with the experimental results that all the reactions are first-order in both azide and Re complex, the calculations predict the either **TS-2** or **TS-3** will determine the observed second order rate constant.

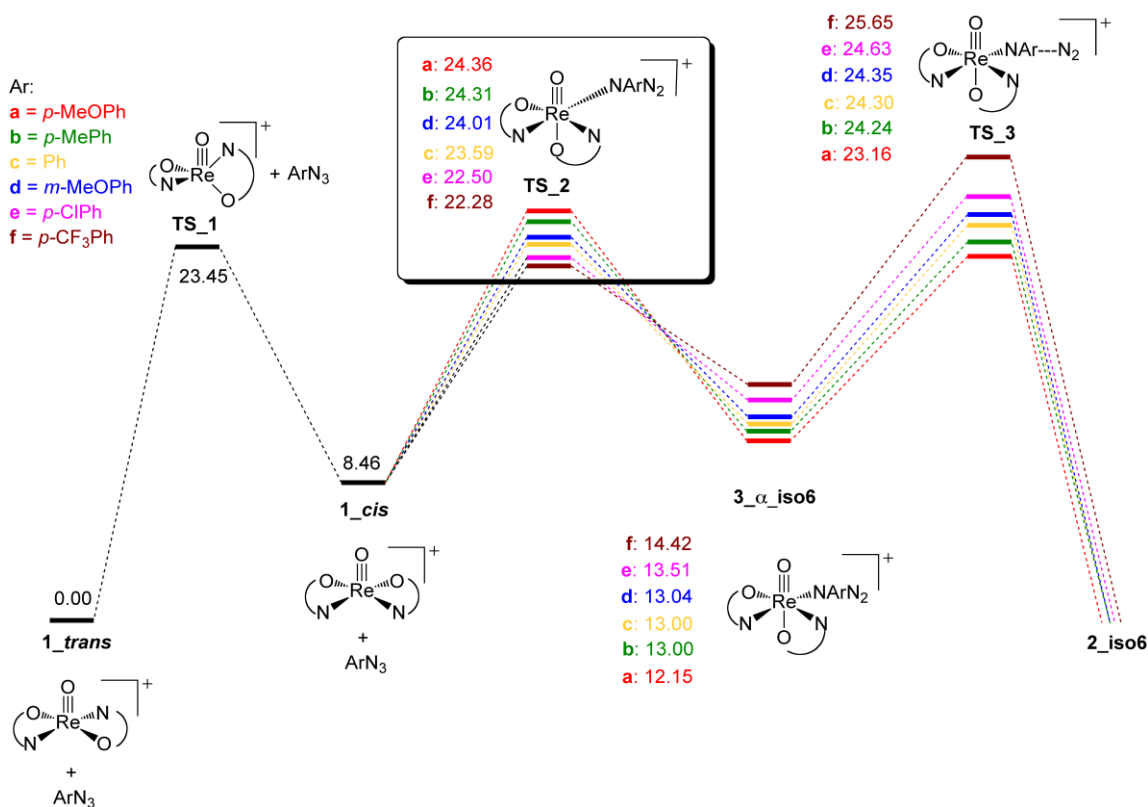


Figure 35. The solvated ΔG (kcal/mol) diagram for the reaction of Rhenium oxo complex with ArN₃. (solvent: CH₃CN)

The first of these key free-energy barriers, **TS-2** (in the box), corresponds to attack of the azide in the forward direction or loss of the azide from the six-coordinate intermediate, **3_α_iso6**, in the back direction. On the electronic energy surface, **3_α_iso6** is more stable than **1_cis** + azide, while the entropy loss in forming **3_α_iso6** from **1_cis** + azide results in a higher free-energy for **3_α_iso6** as shown in **Figure 35**. A scan of the electronic energy for the removal of the bound azide from **3_α_iso6** results in a smooth increase in the energy as the system returns to **1_cis** + azide (see **Figure 29**). Thus, the free-energy barrier for the loss of the azide from **3_α_iso6** is dominated by the enthalpy difference between **3_α_iso6** from **1_cis** + azide, so **TS-2** is located on the free-energy profile at this energy. Because of this close relationship, the order of the **TS-2** free-energy barriers corresponds inversely to the order of stability for the intermediate, **3_α_iso6**. So the most stable intermediate, **3_α_iso6**, has the highest barrier for the loss of the azide. The second key free-energy barrier, **TS-3**, corresponds to the extrusion of N₂ from the intermediate **3_α_iso6**. Here, the most stable intermediate **3_α_iso6**, is the intermediate that is further along the reaction coordinate toward products, and hence, has the lowest barrier to N₂ loss. Thus, the order of the free-energy barriers for **TS-3** corresponds directly to the order of stability for the intermediate, **3_α_iso6**.

4.4.4 Explanation of the break in slope in Hammett plot

Most importantly, the key to the 'break' in slope in the Hammett plot lies in the inverted order of the magnitude of the barriers for **TS-2** and **TS-3** for the different azides, **a-f**. So for **TS-2** the order from highest to lowest barrier is **a** to **f**, while for **TS-3** the order is **f** to **a**. This inverted order is easily explained by the stability of the

intermediate **3_α_iso6**. Since this species is the bound azide adduct, the least strongly bound azide, **f**, will be both the easiest to remove and the most difficult to react to product. Thus, for reactions between **1_cis** and (**f**) *p*-CF₃PhN₃, (**e**) *p*-ClPhN₃, (**d**) *m*-MeOPhN₃ and (**c**) PhN₃, the rate-determining step is the extrusion of N₂ (**TS-3**). However, for the other two azides, (**a**) *p*-MeOPhN₃ and (**b**) *p*-MePhN₃, the rate-determining step switches to the adduct formation (**TS-2**). It is this change of the rate-determining step that results in these two points having a different slope in the computed Hammett plot (**Figure 36**). One can also observe corresponding trends in the bond distances that reinforce these conclusions. For example, the least stable **3_α_iso6** intermediate, (**f**) *p*-CF₃ArN₃, has a ReN bond length of 2.246 Å, while the most stable one, (**a**) *p*-MeOArN₃, has a ReN distance of 2.208 Å. Thus, the most stable intermediate (**a**) has the shortest (and strongest) ReN bond, which means it will have the most difficult azide to remove (**TS-2**) and it is also the furthest along the forward reaction coordinate and will have the lowest barrier for imido formation (**TS-3**).

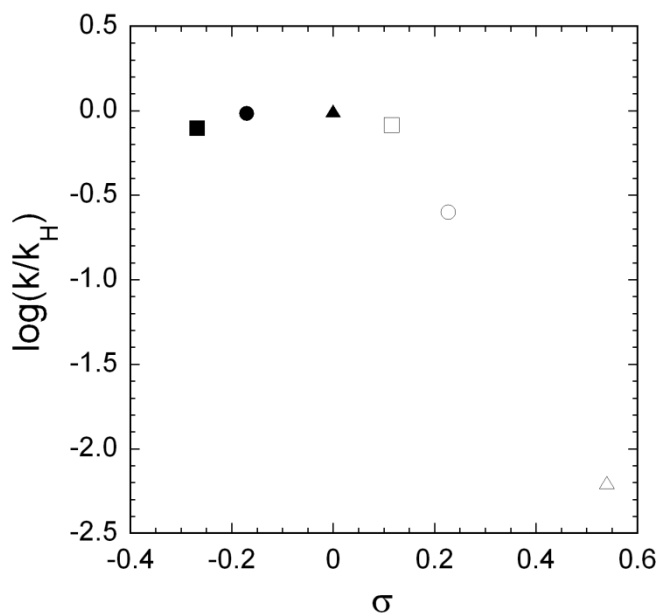


Figure 36. The computed Hammett plot shows fairly good agreement with experimental plot. Key: ■ *p*-OMe, ● *p*-Me, ▲ H, □ *m*-OMe, ○ *p*-Cl, and Δ *p*-CF₃.

4.4.5 Discussion of the accuracy of the computational model

Although the energy differences between the various azides for both **TS-2** and **TS-3** are small and less than the absolute accuracy of DFT calculations, DFT typically reproduces such trends much more accurately as is observed here. Alternative choices for the functional reproduce the trends for the order of the azides **a-f** for each of the TSs and reproduce the inverse of the order of the free-energies within the two transition states discussed above. Furthermore, the range of the experimental rates for the formation of **2a-f_iso6** is consistent with the computed barriers whose range is within 2 kcal/mol. Since the inductive effect of the substitution should affect the barriers of all paths similarly, the lowest overall barriers for reactions between different substituted

azide species and **1** should always be found in path 6, which is more than 5 kcal/mol lower than the next lowest path. The computed absolute overall barriers are around 25 kcal/mol, slightly higher than 21 kcal/mol obtained experimentally, but this systematic error of DFT does not mar the relative trends of concern here. However, one must be cautious about the relative energy of **TS-2** with respect to that of **TS-3** because these two TSs are differently in their electronic structure so different functional can shift all of the **TS-2** free-energies with respect to those of **TS-3**. Apparently, the B3LYP functional with the basis set and solvation corrections used here places the two transitions at the correct relative energy such that the 'break' in the predicted Hammett plot occurs in the same region as the experimental one. Other functional do not produce such fortunate results. However, they do produce the same trends and would result in the same explanation of the experimental results. Thus it is the judicious combination of experiment and theory that leads to the insight about this mechanism.

4.5 Conclusion

In this collaborating work, Abu-Omar group have demonstrated via experiments that the reaction of aryl azides with oxorhenium(V) follows overall second-order kinetics and proceeds via a metal azide intermediate. Furthermore, a Hammett study of the electronic effects on this reaction unveiled a deviation from linearity. Aryl azides with electron-withdrawing substituents and PhN₃ follow a common trend with a reaction constant $\rho = -1.3$. Aryl azides with electron-donating substituents give a $\rho \approx 0$. Our DFT computations reveal that all the reactions follow the direct N₂ extrusion mechanism and the same pathway leading to final products. However, the rate-determining step for the

formation of **2a-f** switches from the formation of the azide adduct to extrusion of N₂ from this adduct. A key to observing this phenomenon is that in this particular case the two barriers are sufficiently close in energy that the change in substituent causes a change in the rate-determining step. What is remarkable about this particular reaction is not that these two barriers have opposite behavior with respect to their order for a series of substituents, which is essential but easily explained, but that they have such similar barriers that changes in substituents somewhat far from the reacting atoms cause a change in the rate-determining step.

CHAPTER V

A NITRENE-RELEASE MECHANISM IN CONVERSION FROM VANADIUM ORGANOAZIDE COMPLEXES TO TERMINAL VANADIUM IMIDES

5.1 Introduction

Organic azide molecules are commonly used in organic synthesis as they are easy sources of nitrene radicals.^{62, 63, 64} The nitrene transfer reactions are usually catalyzed by transition metal complexes. The chemistry of this transformation has been reviewed in the introduction of CHAPTER IV, so I will briefly introduce the chemistry of phenyl nitrene radical herein.

The electronic structure and chemistry of nitrene radicals have been studied both experimentally and theoretically for decades.⁸⁶ It is widely accepted that the phenyl nitrene radical has a triplet ground state. In a qualitative view (**Figure 37**), it has three nonbonding molecular orbitals centered on nitrogen: one *sp* hybrid orbital with very large *s* character and two near-degenerate *2p* orbitals, and those three orbitals are orthogonal to each other. Due to its large component of *s* character, the hybrid orbital is significantly lower in energy than the two pure *2p* orbitals, therefore accommodating a pair of electrons. Each of the other two electrons occupies one nitrogen *2p* orbital, respectively. These two electrons adopt same spin to gain the stability brought about by exchange energy, making the triplet configuration the ground state (3A_2) of this radical. The first excited state is the “open-shell singlet” configuration, in which the two unpaired electrons are anti-ferromagnetically coupled (1A_2). Both experimental and

computational data reveal an energy gap of ~18 kcal/mol between this excited state and the ground state.^{87,86} The close shell singlet state is even higher in energy (~31 kcal/mol above the ground state) because of the strong Coulomb repulsion when the two electrons occupy the same orbital.

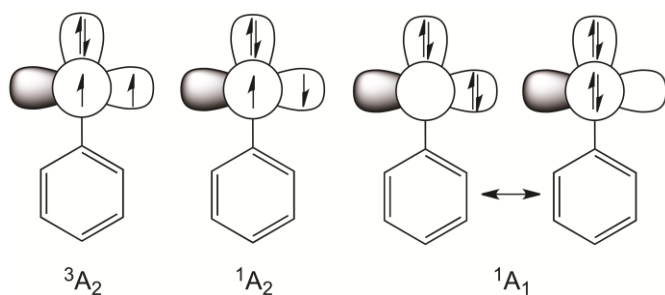


Figure 37. Qualitative view of the electronic configuration of the triplet nitrene and singlet nitrene.

The phenyl nitrene radical usually comes from the photo or thermal dissociation of phenyl azide. The radical is highly unstable at room temperature and prone to dimerize or isomerize rapidly (**Figure 38**). The singlet phenyl nitrene can rearrange into benzazirine (BA) or dehydroazepine (DA). These species can be trapped to make ethanethiol or diethylamine products. Triplet phenyl nitrene can be formed directly from photolysis of phenyl azide or from inter-system crossing of singlet nitrene. When the temperature is below 170 K, the singlet nitrene rearrangement is impeded. Instead, azobenzene (AB) is formed upon photolysis of PhN_3 . This product can be viewed as dimerization product of triplet nitrene.

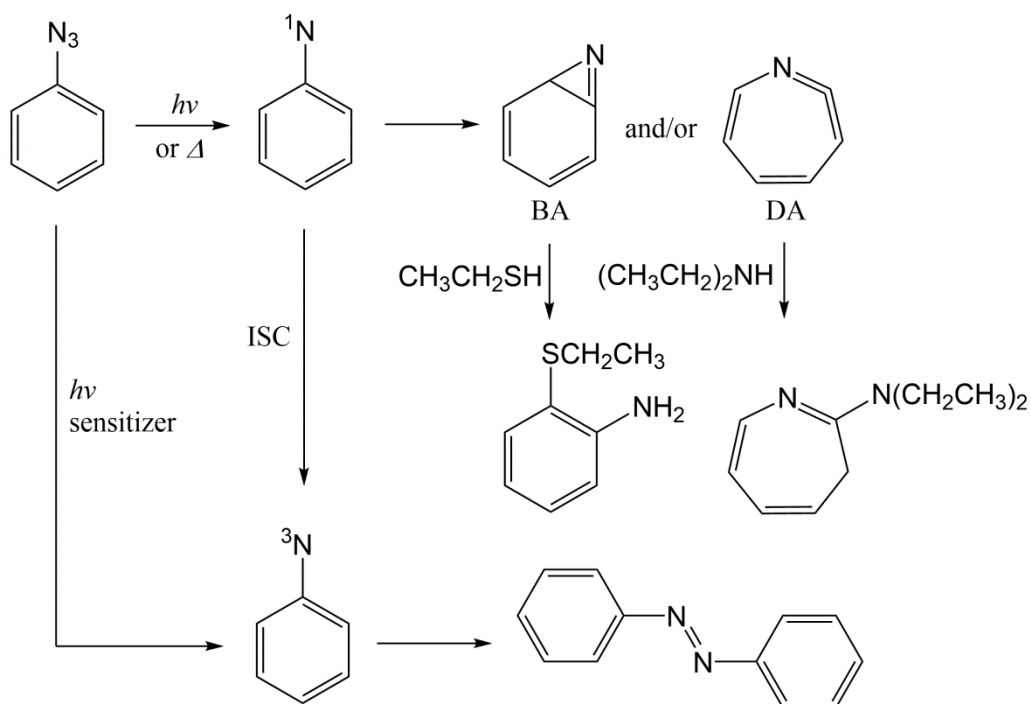


Figure 38. A summary of transformation of nitrene radicals.

Metal organoazide complexes have long been proposed as the important intermediates in nitrene transfer reactions and most reported reactions yield metal imido compounds. Only a few systems are able to catalyze N-N coupling to generate azoarenes. Peters and co-workers investigated these transformations by a trigonal bipyramid iron compound in 2010⁸⁸ and a trigonal bipyramid ruthenium metalloradical in 2012.⁸⁹ Chang and coworkers also reported that a well-defined vanadium organoazide complex generates azoarene as side product during the conversion to vanadium imide.⁹⁰ In the proposed mechanisms, free nitrene radicals are released in these reactions before forming azoarene species. However, it was extremely difficult to trap the triplet nitrene since all the trapping reagents would react with the metal compounds. Therefore

computational tools are needed to verify the proposed mechanisms. In this work, we will mainly focus on the Chang's vanadium system and explore all the possible reaction pathways to determine which mechanism is the most favorable one.

5.2 Summary of experimental observations

Chang and co-workers synthesized a series of vanadium organoazide compounds, $(\text{tpa}^{\text{Mes}})\text{V}[\eta^1\text{-N}_3(p\text{-C}_6\text{H}_4\text{R})]$ (tpa^{Mes} = tris(pyrrylmesityl)amine; R = OCH₃ (**2a**); H (**2b**); CH₃ (**2c**); N(CH₃)₂ (**2d**)) from reactions between $(\text{tpa}^{\text{Mes}})\text{V}(\text{THF})$ (**1**) and the corresponding aryl azide molecules (**Figure 39**). Compound **2(a ~ d)** were isolated and well characterized by crystallography.

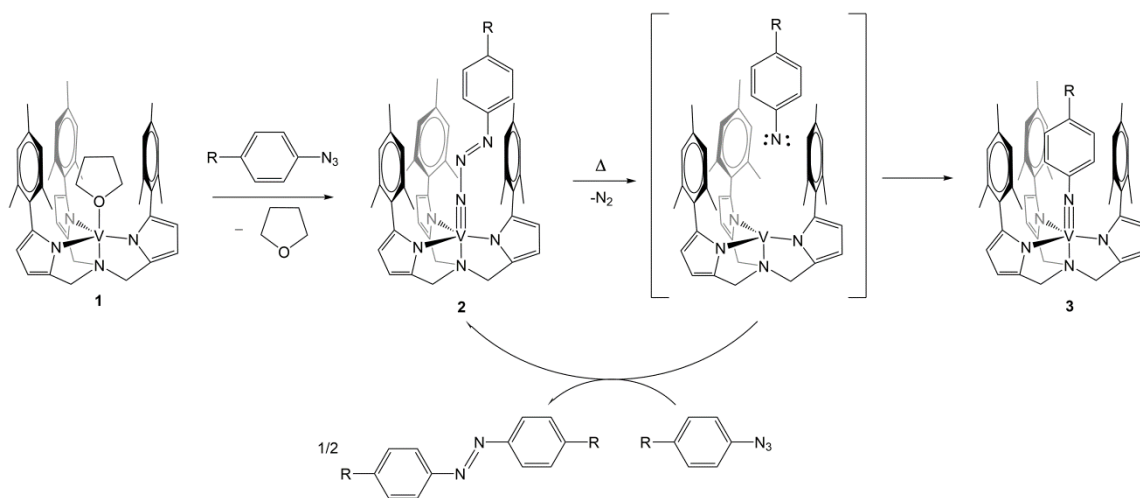


Figure 39. Synthetic scheme of vanadium azide compounds and vanadium imido compounds.

When compound **2(a ~ d)** (dissolved in benzene) was heated to 55 °C for 30 m ~ 3 h, color change was observed. The products were isolated and fully characterized as a

vanadium imido compounds, $(\text{tpa}^{\text{Mes}})\text{V}[\text{N}(p\text{-C}_6\text{H}_4\text{R})]$ (**3a** ~ **3d**). This thermal decay of **2** is first order in the reactant and the reaction rate is accelerated by electron-donating substituents on the phenyl ring. These four species follow the same linear trend in Hammett plot, which suggests that these reactions follow the same disassociation mechanism.

Interestingly, stoichiometric thermolysis of **2** yielded small amount of corresponding azoarene. This observation may indicate a similar nitrene-release mechanism as that proposed for Peter's iron and ruthenium systems. When the azide alone was heated in the same condition, there is no detectable nitrene or azoarene formed in the solution, suggesting that the vanadium compounds were involved in azoarene formation. The singlet nitrene trapping experiments were inconclusive. The triplet nitrene trapping could not be investigated because all the trapping reagents react with the transition metal compounds.

5.3 Computational details

The computations were accomplished by density functional theory (DFT) as implemented in the Gaussian 09 program.⁴⁸ TPSS⁵¹ functional was used throughout the whole project. For all the geometry optimization, BS1 was applied. In BS1, effective core potential (ECP10MDF)⁹¹ and its corresponding basis set $((8s7p6d2f1g)/[6s5p3d2f1g])$ ⁹² was used on the vanadium atom. The four nitrogen atoms on the support ligand and the three nitrogen atoms in the azide used large basis set, 6-311G(d).⁵⁶ All the other atoms used 6-31G basis sets.⁵⁴ In order to obtain more accurate energetic data and include the solvation correction, the single point energies of all

important species were calculated by BS2 in SMD⁸³ solvation model. In BS2, the basis set used for vanadium is the same as in BS1. 6-311+G(d)⁵⁶ is used on all the nitrogen atoms and 6-311G(d)⁵⁶ is used on all the carbon, oxygen and hydrogen atoms. NBO 5.9⁴⁹ was also used to characterize the bonding situation in a few critical species. The importance of dispersion correction was also tested based on Grimme's DFT-D3 scheme.⁵⁷

5.4 Results and discussion

5.4.1 Computational characterizations of metal organoazide compound 2

In Chang group's work, a η^1 -azide adduct **2a** was obtained from treatment of (tpa^{Mes})V^{III}(THF) (**1**, THF = tetrahydrofuran) with *p*-methoxyphenyl azide (N₃Ar^{OMe}) in toluene at room temperature. **2a** was isolated and characterized as a "diazenylimidovanadium(V) species" based on structural parameters and its diamagnetic nature. **1** has triplet ground state since each of the two *d* electrons occupies one of the two nearly degenerate orbitals, *d*_{xz} and *d*_{yz}, respectively. During the process of conversion from **1** to **2a**, THF was replaced by azide ligand; vanadium center loses two electrons and a close-shell compound was made.

One may readily propose the existence of a triplet η^1 -azide adduct, in which the organoazide just act as an L type ligand. In fact, both close-shell and open-shell **2a**, namely, **2a_sing** and **2a_trip** were optimized in the computations (**Figure 40**). Selected computed structural parameters of **2a_sing**, **2a_trip** and the experimental data of **2a** are listed in **Table 18** for comparison. Optimized geometry of **2a_sing** agrees quite well with the crystal structure, especially on the key parameters of this compound, like V-N3

bond length and bond angles of V-N3-N2 and N1-N2-N3. The extremely short V-N3 bond (1.692 Å) suggests multiple bond character and the two bond angles (172° and 121°) reflect sp and sp^2 hybridization on N3 and N2 atoms, respectively. The geometry of **2_trip** is quite different from its close-shell isomer. The V-N3 bond is ~0.3 Å longer than that in **2_sing**, indicating a much weaker interaction between the vanadium center and the azide ligand in **2_trip**. The N-N bond lengths of the azide ligand are almost the same as those in free azide molecule (1.238 Å for N1-N2 and 1.149 Å for N2-N3 from computational optimization). Furthermore, N1, N2 and N3 atoms remain nearly linear. All of these geometric features indicate lone-pair σ donation from the terminal nitrogen is the only interaction between vanadium and azide.

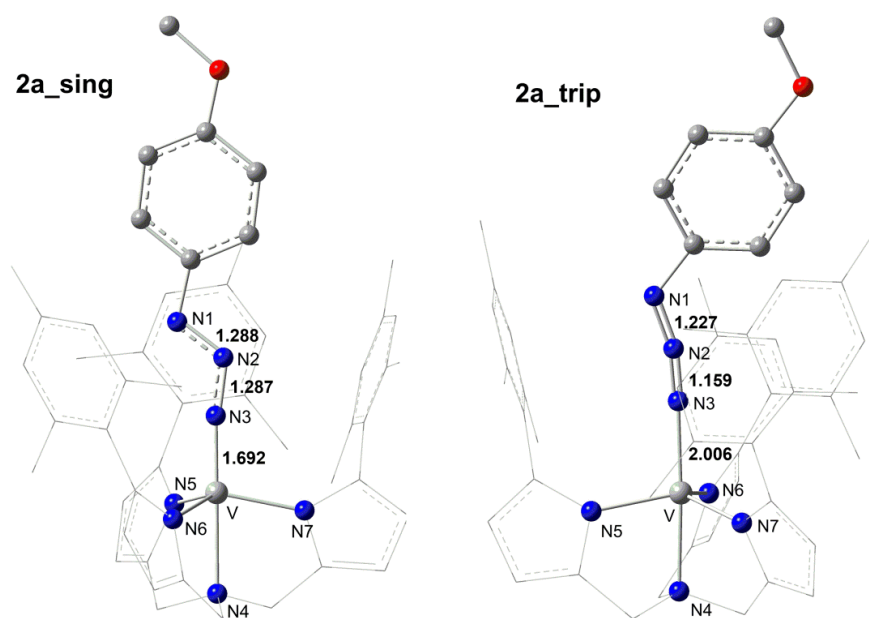


Figure 40. The optimized structures of **2a_sing** (left) and **2a_trip** (right).

Table 18. Selected structural parameters of **2a** from computations and experiments. (Bond length in Å, bond angle in degree.)

	Computational		Experimental ^a
	2a_sing	2a_trip	2a
V-N3	1.692	2.006	1.693
N1-N2	1.288	1.227	1.261
N2-N3	1.287	1.159	1.271
V-N4	2.214	2.144	2.173
V-N(eq) ^b	1.953	1.976	1.925
N1-N2-N3	121	165	118
V-N3-N2	172	176	170

^aAll the experimental parameters are from ref 90.

^bThe average bond length between vanadium atom and the three nitrogen atoms in the equatorial plane (N5, N6, N7 shown in **Figure 40**).

With respect to these species' electronic structures, NBO analysis on the V-N3 bond in **2a_sing** unambiguously shows triple bond character (**Figure 41**). All three bonds are polarized toward the nitrogen atom, especially the σ bond, which is defined as donor-acceptor interaction by NBO. For the two π bonds, nitrogen p orbitals contribute 61% and 68%, respectively. So the formation of **2a_sing** could be simply viewed as a 2-electron oxidation on vanadium center. In **2a_trip**, the Mulliken spin density on vanadium center is computed as 1.95, so the two unpaired electrons are located in non-

bonding orbitals, d_{xz} and d_{yz} , indicating minimal or no π interactions between vanadium and the terminal azide nitrogen. The longer V-N4 bond in **2a_sing** (2.214 Å) than that in **2a_trip** (2.144 Å) also reflects that the azide ligand has stronger *trans* influence (hence stronger azide-vanadium interactions) in **2a_sing**.

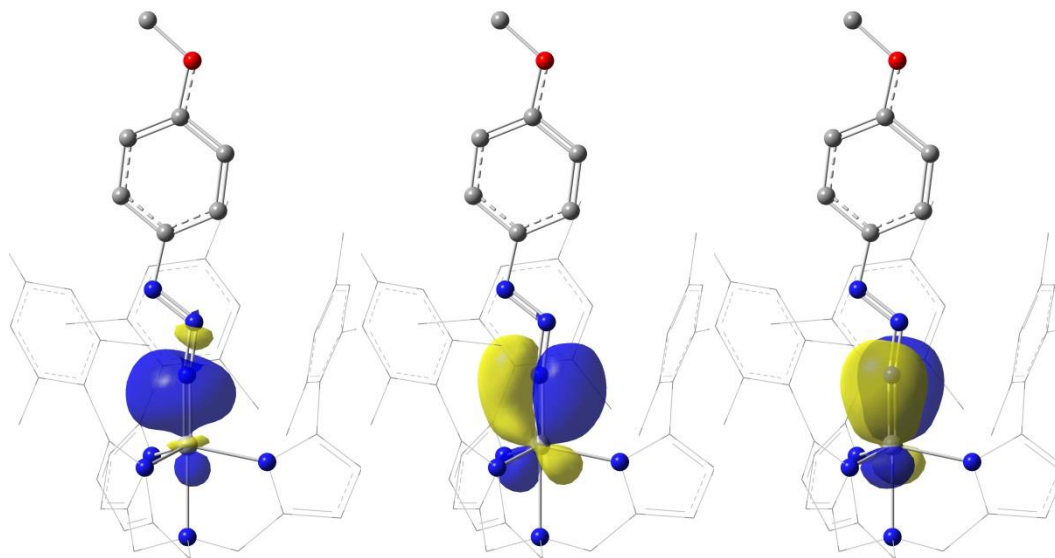


Figure 41. Natural bonding orbitals of **2a_singlet** clearly show one V-N σ bond and two V-N π bond.

2a_sing is more stable than **2a_trip** by 0.5 kcal/mol ($\Delta\Delta G_{sol}$) calculated by TPSS, which is consistent with the experimental fact that the product is diamagnetic. Comparisons of their energies by the popular hybrid functionals B3LYP predicts that **2a** has a triplet ground state. This finding suggests that the inclusion of HF component in the functional favors the high spin triplet state too much. Therefore a pure functional like TPSS is a more appropriate choice for this system.

In the process of forming **2a**, the N_γ of azide molecule approaches the metal center, which has two parallel-spin electrons. Before the stable intermediate **2a_sing** is formed, **2a_trip** will be generated by only σ lone pair donation without the spin flip that must occur. **2a_trip** is 8.8 kcal/mol more stable than the initial reactants, showing stronger interaction between the vanadium and azide than that between vanadium and THF (**Figure 42**). Before proceeding to **2_sing**, the reaction will go through a region in which the triplet potential energy surface crosses the singlet one (**Figure 43**) and at some specific point the reacting species will move from the triplet surface onto the singlet surface. Accurately locating this minimum energy crossing point (MECP) between the two potential energy surfaces is still a big challenge for current computational codes. In this work we employed an approximate algorithm developed by Jeremy Harvey and his co-workers.⁹³ The calculated structure of MECP is intermediate between **2a_sing** and **2a_trip**. The V-N3 bond length of it is 1.832 Å and the N1-N2-N3 angle is 142.2° (**Table 19**). From the energetic data (**Figure 43**), there is only a very low barrier to overcome from **2a_trip** to **2a_sing**, which could explain why the **2a_trip** is not detected in the experiment.

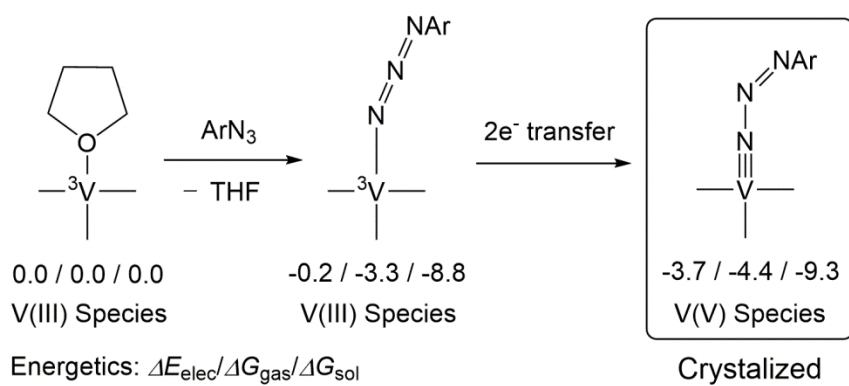


Figure 42. The formation of **2a_sing**.

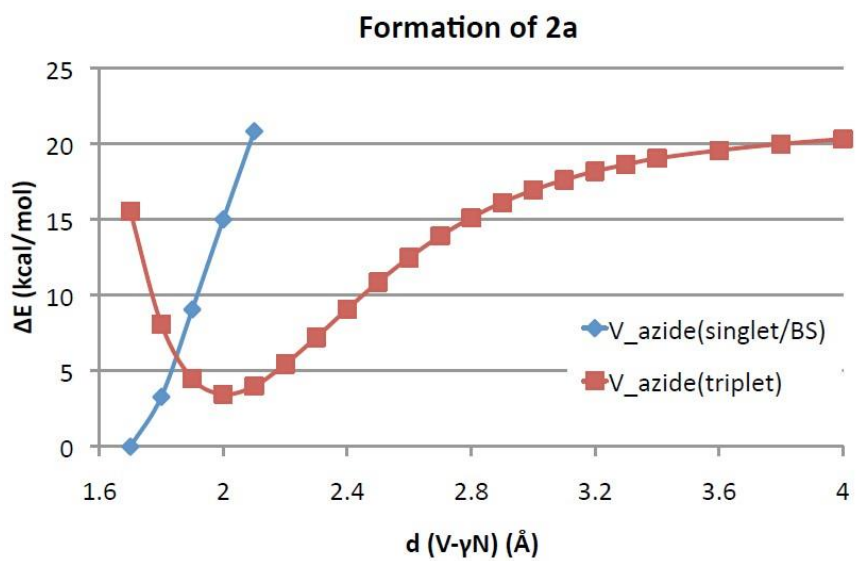


Figure 43. Potential energy surface scan during the formation of **2a**.

Table 19. Comparisons of energetics, critical geometric parameters and S^2 values among **2a_sing**, **2a_trip** and the MECP.

	$\Delta E(\text{kcal/mol})$	$d(\text{V-N3})(\text{\AA})$	$\text{N1-N2-N3}(\text{ }^\circ)$	S^2
2a_trip	3.5	2.006	165.0	2.0
MECP	9.0	1.832	142.2	0.55
2a_sing	0.0	1.692	118.4	0.0

5.4.2 Decomposition of azide molecule

Before moving to a thorough discussion of the decomposition of **2a_sing**, it might be helpful to examine decomposition process of the free azide molecule, $\text{N}_3\text{Ph}^{\text{OMe}}$. The decomposition products are nitrene radical and N_2 molecule. Since the azide molecule has a singlet ground state and the nitrene has a triplet ground state, there will be another spin-crossover in this system. A potential energy scan was conducted in order to have a rough idea about the structures involved in MECP (**Figure 44**). The triplet state is >40 kcal/mol higher than the singlet state before the $\text{N}_\alpha\text{-N}_\beta$ bond is stretched. When this bond is elongated, the energy of the singlet state rises quickly and triplet state is gradually stabilized. When the bond length is longer than 1.4 Å, the open-shell singlet wavefunction has lower energy than the close-shell singlet wavefunction, which means the NPh fragment already has some nitrene character at this stage. Before the dissociation transition state on singlet state is reached, the energy of the triplet falls below the open-shell singlet one. Again Harvey's scheme is used for locate this point

more accurately. The energies of the MECP and open-shell transition state are really close, while the MECP has shorter N_α - N_β bond length at 1.502 Å.

The electronic states of the dissociating azide molecule (or the nitrene- N_2 adduct) are fairly complicated and are difficult to be accurately described by DFT (single determinant) calculations. It seems that the spin-crossover occurs before the open-shell singlet species reaches its dissociation transition state. However, since the reaction was conducted without light, the probability of spin-crossover might not be quite high and it is hard to make accurate predictions. Therefore the barrier height might be higher than the number we obtained by MECP calculation. Furthermore, the barrier height we calculated for the open-shell transition state is from a broken-symmetry DFT calculation. This barrier will increase if it is corrected by Yamaguchi's spin projection scheme.⁹⁴ However, the exact barrier height for the free azide dissociation reaction is not critical for understanding the transition metal reaction. These results indicate that the barrier of free azide decomposition should be no lower than ~34 kcal/mol and this lower bound information is sufficient for this study.

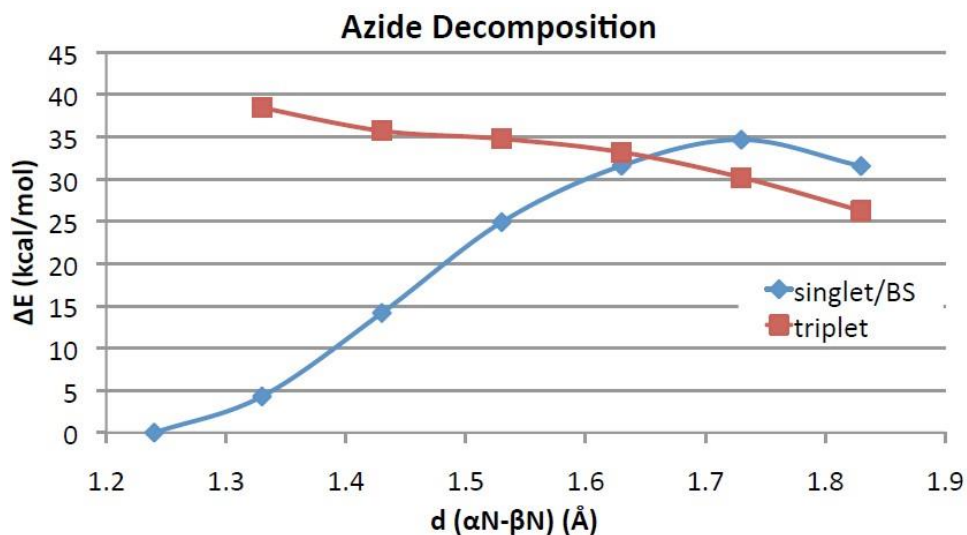


Figure 44. Potential energy surface of free azide decomposition.

Table 20. Important parameters of MECP and singlet transition state during the free azide decomposition process.

	ΔE^a (kcal/mol)	$d(N_\alpha-N_\beta)$ (Å)	S^2
MECP	35.3	1.502	0.65
1 TS	34.4	1.705	0.57

^a ΔE is relative to the energy of the ground state azide molecule.

5.4.3 Decomposition of the metal azide compound

Since the azide can bind to a transition metal center in various ways, the structure of the stable intermediate **2a_sing** determined above, may not be the only structure involved in the reaction. Therefore, we tested all the possible pathways in which metal azide converts to metal imide (**Figure 45**).

5.4.3.1 Examination of PATH1

According to the experimental proposal, the N1-N2 bond of **2a_sing** is gradually stretched during the decomposition process and **2a_sing** is finally separated into a free triplet nitrene radical and vanadium dinitrogen adduct. The latter species is very stable since N₂ is not a good σ donor. In this process the vanadium center goes through a two-electron reduction, producing a vanadium dinitrogen adduct in a triplet ground state. The triplet nitrene quickly and easily replaces the N₂ ligand and forms a strong V \equiv N triple bond, yielding vanadium imido product.

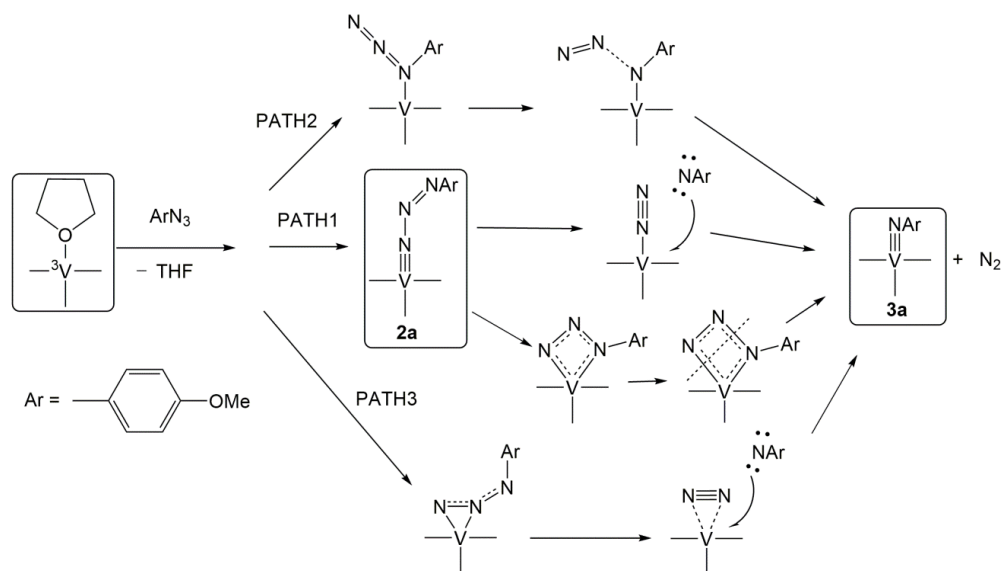


Figure 45. Possible pathways of conversions from metal azide to metal imide.

The computational results are shown in **Figure 46** and **Figure 47**. Two electrons transfer from the azide ligand to the vanadium center, generating two fragments both having triplet ground state. These two fragments are anti-ferromagnetic coupled (**Figure**

48), so the overall spin of this compound is still zero. Since broken-symmetry (BS) DFT was applied in these computations, the wavefunction of this open-shell singlet determinant $M_s = 0$ transition state is not eigenfunction of S^2 operator ($\langle S^2 \rangle = 1.60$), but a mixture of singlet, triplet, and quintet states. It can be viewed as a mixture of true singlet state, triplet state and even quintet state. This direct dissociation barrier of **2a_sing** is 20.0 kcal/mol. In order to gain a better idea of the true singlet state energy, we calculated the single point energies of this transition state geometry on the triplet and quintet surfaces. The electronic energies of triplet and quintet states are higher than the open-shell 'singlet' determinant by 4.89 and 12.51 kcal/mol, respectively. Similarly, this triplet determinant is also a mixture of quintet state energy and true triplet state energy. Only the quintet wavefunction is the eigenfunction of the S^2 operator. Because all three states are involved in the BS 'singlet' wavefunction, it is impossible to obtain the true singlet state energy by Yamaguchi's spin-projection scheme. However, since the energy of both quintet and triplet are higher than that of the BS 'singlet', we can safely conclude that the true singlet energy should be lower than the BS solution. Therefore, the barrier height of 20 kcal/mol can be viewed as an upper bound of this dissociation barrier.

The dissociation products (V-N₂ adduct and nitrene radical) are ~30 kcal/mol lower in energy than the transition state. To proceed to the final product, the nitrene needs to replace the N₂ ligand, which should be easy since N₂ is a poor σ donor. Potential energy scan indicate the barrier for removing the N₂ ligand is no higher than 15 kcal/mol relative to the energy of V-N₂ adduct, which is much lower than the dissociation barrier of **2a_sing**. Once the N₂ is gone, the nitrene fragment easily attacks

the triplet vanadium center to form the final product **3a**. This step is a combination of two radicals, therefore it is extremely exothermic and it can proceed with little barrier.

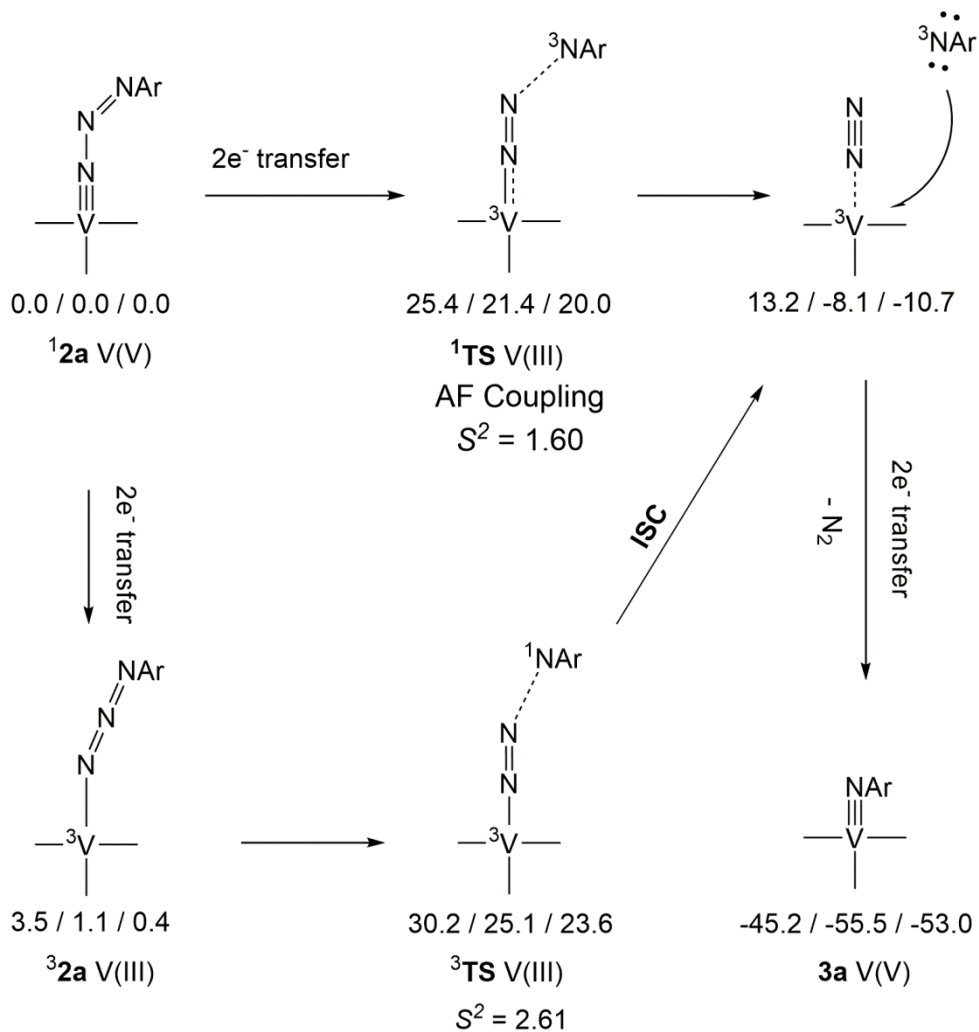


Figure 46. The computed energetic data of PATH1. The energies shown in the figure are in the format of $\Delta E_{elec} / \Delta G_{gas} / \Delta G_{sol}$ and the values are in kcal/mol.

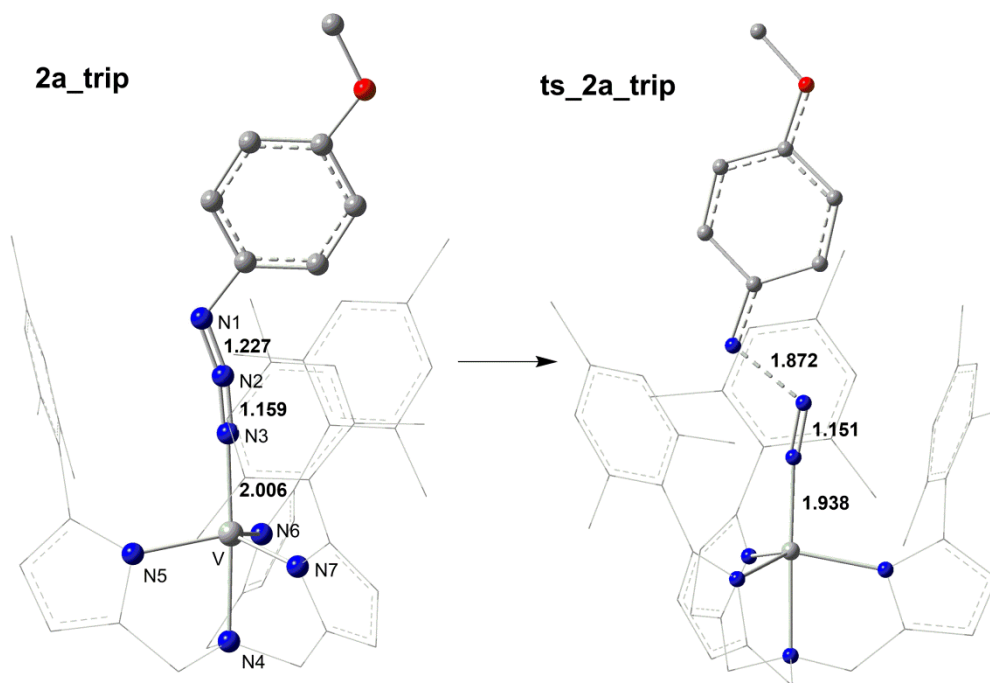


Figure 47. Structures of **2a** and corresponding transition states **ts_2a** in both open-shell singlet and triplet states.

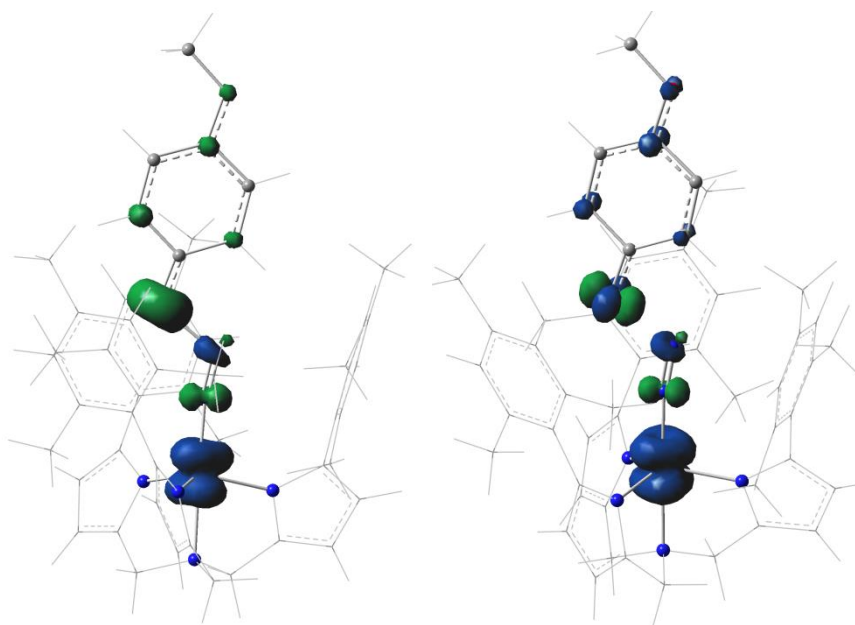


Figure 48. The spin density of direct dissociation transition states of **2a_sing** (left) and **2a_trip** (right).

Comparing the barrier of direct dissociation of **2a_sing** and the barrier of free azide decomposition, we find the barrier significantly lower when the vanadium is present. We can rationalize this difference from the computational results: 1) The N_{α} - N_{β} bond length is longer in **2a_sing** than that in the free azide (1.288 Å vs. 1.238 Å), suggesting a weaker N_{α} - N_{β} bond in **2a_sing**, and 2) The dissociation of **2a_sing** directly leads to two fragments both in their ground states without any spin-crossover. This process is thermodynamically favored and brings down the barrier to some extent. Based on the above reasons, the vanadium center greatly reduced the barrier height of nitrene formation.

When **2a_sing** is heated during the dissociation process, besides directly dissociating into nitrene and V-N₂ adduct, it might firstly overcome a lower barrier to convert into **2a_trip**. Then we have another possible pathway to consider, as **2a_trip** can also dissociate and generate nitrene radical, but there is no electron transfer in this process as that happened in the formation of **2a_trip**. The remainder of this pathway is similar to the free nitrene dissociation. If we assume that there is no spin-cross over before the dissociation transition state, the barrier height is calculated to be 3.6 kcal/mol higher than that of the open-shell singlet transition state.

PATH1 can explain the experimental findings. In the stoichiometric thermolysis reaction of **2a**, immediately after **2a_sing** dissociates into triplet nitrene and vanadium complex plus N₂, the nitrene radical is much closer to the vanadium atoms than to another nitrene because the solution is fairly diluted (~0.004 mol/L). So the probability of recombination between the nitrene radicals and its vanadium complex to form **3a**, is higher than that of the recombination between two nitrenes to form an azoarene. Thus only a small amount of azoarene compounds are detected after the reaction is complete. In the catalytic azoarene formation reaction, the concentration of azide is 25 times higher than **1**. The nitrene radicals form in the dissociation will immediately react with the free azide molecules or other free nitrene radicals to form azoarene. Therefore the formation of **3a** is greatly impeded because almost all the nitrene radicals are consumed to make azoarene compounds.

Furthermore, we also tested this nitrene release mechanism on the thermolysis of **2b**, **2c** and **2d**. The Hammett plot shows linear relationship (**Figure 49**) for the four

species and stronger electron donating ability can accelerate the reactions, which is consistent with the experimental observations. Although the slope of this line ($\rho = -7.6$) is larger than that of the experimental plot ($\rho = -1.5$), it is within the typical error range of DFT since this slope is extremely sensitive to the relative barrier height difference.

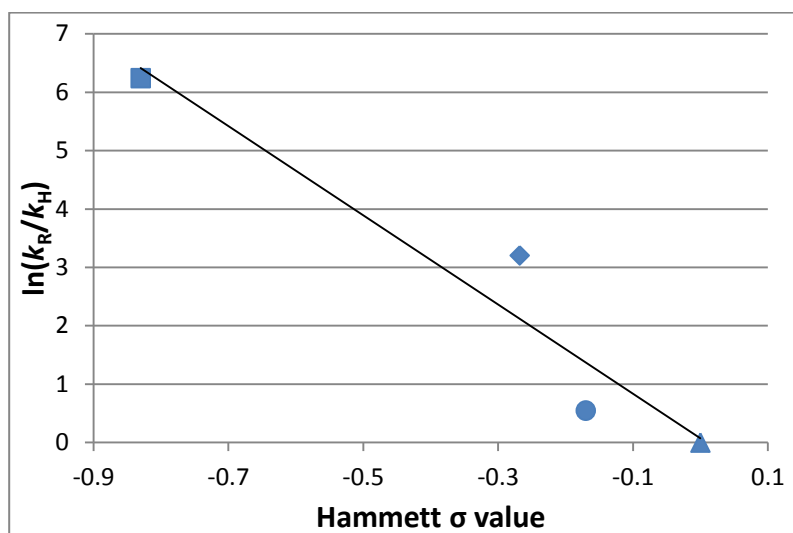


Figure 49. Computed Hammett plot for thermolysis of the vanadium azide compounds, $(\text{tpa}^{\text{Mes}}\text{V}[\eta^1\text{-N}_3(p\text{-C}_6\text{H}_4\text{R})])$. R = ■ $\text{N}(\text{CH}_3)_2$ (2d); ◆ OCH_3 (2a); ● CH_3 (2c); ▲ H (2b).

The slope of this trend line is $\rho = -7.6$.

Besides the direct dissociation of azide ligand, we also tested the mechanism featuring an intermediate with both the azide N_α and N_γ bound to the vanadium center (**Figure 45**). We located this species as intermediates in both singlet and triplet states. They are pretty close in energy and both higher than **2a_sing** by ~41 kcal/mol. So we can safely rule out the possibility of forming the four-member ring intermediates in the reactions.

5.4.3.2 Examination of PATH2

In PATH2, the azide firstly binds to the vanadium center by lone pair donation from N_α , forming intermediate **4a** (**Figure 50**). The Mulliken spin density on vanadium is 2.14, so **4a** has a triplet ground state. Computational results show that this intermediate is 21.4 kcal/mol higher than **2a_sing** (**Figure 51**), even higher than the dissociation barrier of **2a_sing**, meaning it is extremely unlikely in the reaction. The barrier for this intermediate is 34.1 kcal/mol relative to **2a_sing**. The $\langle S^2 \rangle$ value of the transition state is 2.07, a value that indicates almost no mixing from the quintet state, and thus a reliable energy for this transition state.

These energetic data predicts that PATH2 is not feasible for the reaction. The major reason could be the steric effects coming from the bulky ligand. The three mesityl groups on the ligand limit the space for the incoming ligand on the axial position. Obviously **4a** has more trouble in fitting itself in this cup-like space than the end-on adduct **2a** (either singlet or triplet) does. Once **4a** is formed, the repulsion between the azide and the mesityl groups pushes the “cup” open, raising the total energy of this intermediate.

5.4.3.3 Examination of PATH3

The azide molecule can also bind to the metal center in an η^2 -manner to form a N_β - N_γ side-on metal-azide adduct, **5a**. In **5a** both N_β and N_γ form single bond with vanadium center, significantly elongating the N_β - N_γ bond (**Figure 52**). This compound is 15.6 kcal/mol higher in gas phase free energy than **2a_sing**. This difference can be attributed to the steric repulsion, like that in **4a**, and also weaker bonds between metal and azide molecule.

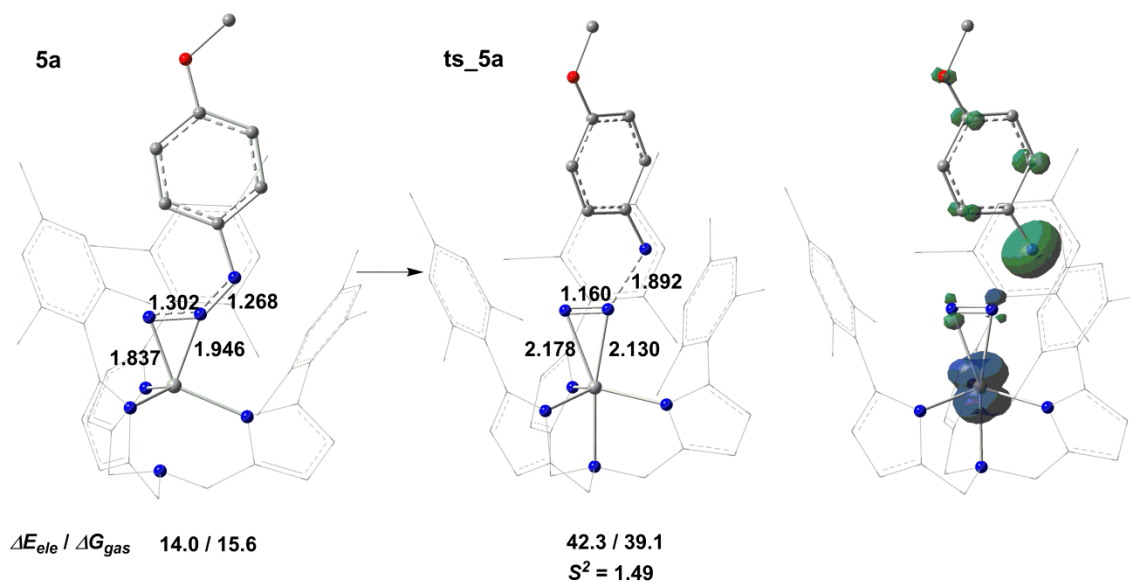


Figure 52. The optimized structures/energetics of **5a** and **ts_5a** and the Mulliken spin density of this open-shell transition state. Energies are in kcal/mol relative to **2a_sing**.

Like **2a_sing**, **5a** can dissociate through an open-shell singlet transition state and yield two triplet fragments. The energy of this transition state is 23.5 kcal/mol higher than **5a**, a relative value similar to that for the dissociation barrier of **2a_sing**. However,

this pathway cannot compete with the direct dissociation of **2a_sing**, due to the steric repulsion in the starting molecule, **5a**, which makes this entire pathway unfavorable.

Like **2a_trip**, there is also a triplet $N_{\beta}-N_{\gamma} \eta^2$ side-on vanadium azide adduct, **5a_trip**. Again, the vanadium azide interaction is even weaker in this compound, making it 9.6 kcal/mol higher than the singlet adduct, **5a**. Therefore, the details of this compound are not discussed since it is definitely not involved in the reaction.

5.4.4 The evaluation of the steric effects and dispersion interactions

In our previous work, we proved that PATH2 is the most favorable pathway for rhenium azide to rhenium imide conversion. In this sterically demanding vanadium system, the free nitrene release pathway is more favorable. The bulky supporting ligand in the vanadium complex limits the space for the incoming azide ligand. In order to have a quantitative understanding about the importance of these steric effects, we describe below a simplified supporting ligand and compare the energy changes in each possible pathway. Moreover, because the species involved in this system have several phenyl rings, we also tested the dispersion correction for some important species to see if it will bring about any change to the reaction pathway.

In the simplification process, all the mesityl groups on the supporting ligand are replaced by methyl groups so that the previously limited space for the incoming substrate is greatly expanded. Then, we fully optimized some of the critical species with this simplified ligand (**Table 21**). It is not surprising that the energies of **4a**, **5a**, and the four-member ring intermediates, which suffer greatly from the steric repulsions, are stabilized significantly. However, simplifying the ligand does nothing to reduce the

barrier in PATH1. On the contrary, the barrier is 1.2 kcal/mol higher after the ligand simplification. It is because that the transition state has less steric repulsion than the starting material does in the full model thus its structure is more relaxed. But the transition state in the simplified model does not gain this stabilization because there is no steric repulsion in neither the starting material or the transition state.

Due to this simplification, the barrier height of PATH2 drops 1.1 kcal/mol below that of PATH1. Again, since the wavefunction of **ts_2a_sing** is a broken-symmetry solution, the true singlet energy should be lower than 26.6 or even 25.5/mol. It is difficult, actually unnecessary, to decide which pathway will dominant this specific reaction with this simplified ligand. More importantly, we know for sure simplified ligand favors PATH2, in which no free nitrene or azoarene will be formed. This finding will provide some insight in ligand design for obtaining different targeting products from this seemingly simple and straightforward reaction.

Dispersion interaction may influences the reaction mechanism since several phenyl groups are involved in the crowded transition states. Compared to the results shown in **Table 22**, the barrier of PATH1 is raised by 2.5 kcal/mol by dispersion corrections. It is mainly because the transition state has more stretched N_{α} - N_{β} bond than **2a_sing** does, making the phenyl ring in the nitrene fragment further away from the three mesityl groups thus reducing the dispersion interaction. In **4a** and **ts_4a**, the phenyl ring in the azide is closer to the mesityl groups so there is stronger dispersion interaction which brings down the relative energies. So the dispersion interaction favors PATH2.

But the previous discussion suggests that the full-model ligand disfavors PATH2 due to steric repulsion. Therefore it is important to balance these two factors in ligand design.

Table 21. Comparison of electronic energies (kcal/mol) between full model and simplified model of some critical species in the proposed mechanism.

	full model	simplified model
2a_sing	0.0	0.0
ts_2a_sing	25.4	26.6
4a	21.9	14.5
ts_4a	34.5	25.5
int_ring_trip	42.3	31.8
int_ring_sing	38.7	27.1
5a_trip	26.6	24.9
5a	14.0	9.3

Table 22. Single point energies (kcal/mol) calculated for some critical species with and without dispersion corrections.

	TPSS	TPSS-D3
2a_sing	0.0	0.0
ts_2a_sing	25.4	27.9
4a	21.9	16.3
ts_4a	34.5	30.2

5.5 Conclusion

In this work, we studied the detailed mechanism of a series of conversions from vanadium azide compounds to vanadium imido compounds. Computational results suggest that the most plausible pathway is PATH1. In this mechanism, the experimentally isolated compound, **2a_sing**, firstly decomposes into a triplet vanadium-N₂ and a triplet nitrene. Then the N₂ ligand is replaced by nitrene to form a very stable vanadium imido product. Since free triplet nitrene radicals are formed in this process, a small amount of them dimerize into azoarene compounds, as found in the experiment.

Both experiments and computations found lower barriers for the end-on vanadium azide compound **2a_sing** to release nitrene radical than for the free azide to do so. The calculations predict the reasons as: 1) the N_α-N_β bond in **2a_sing** is weaker than that in the free azide; 2) The breaking of the N_α-N_β in **2a_sing** directly gives rise to two fragments both in their ground state while the thermolysis of free azide experiences intersystem crossing, which may slow down the yield of triplet nitrene.

In both PATH2 and PATH3, although dispersion interactions can stabilize both starting materials and the transition states in these two pathways to some extent, the species involved in the reaction suffer from significant steric repulsion, making both of them highly unfavorable. The ligand simplification study suggests that these two factors should be carefully balanced in ligand design to obtain the desired products.

CHAPTER VI

CONCLUSION

In this dissertation I present three systems closely relating to the structure, formation and reactivity of compounds featuring transition metal-ligand multiple bond. Our work demonstrates that close interplays between experiment and theory could convincingly determine the structure of novel compounds, and also uncover the mechanism of complicated reactions.

In the first work, Tilley's group synthesized a novel osmium silylyne compound via a new route involving hydride abstraction from silicon. NMR and DFT computations helped to validate the proposed structure of this complex. NBO and ETS-NOCV analysis revealed the nature of this Os–Si bond as a triple bond consisting of a covalent σ bond and two strong π back-donations. Significantly, the discovery of complex **2** has allowed the exploration of new reactivity for a metal-silicon triple bond. In particular, the cyclo-additions of multiple bonds and the kinetic control mechanism of these reactions found by DFT computations all portend a rich chemical reactivity for $L_nM\equiv ER$ species. The synthesis and computations of different $L_nM\equiv ER$ species further suggest the possibility of existence of more novel transition metal-lyne compounds. This work is also an excellent demonstration of close interplays between experiment and theory in studying novel compounds.

In the second work our collaborator, Abu-Omar group, have demonstrated via experiments that the reaction of aryl azides with oxorhenium(V) compound

([Re(O)(hoz)₂(CH₃CN)][B(C₆F₅)₃], Hhoz = 2-(2'-hydroxyphenyl)-2-oxazolinine, **1**) follows overall second-order kinetics and proceeds to metal imide via a metal azide intermediate. However, a Hammett study of the electronic effects on this reaction unveiled an unusual deviation from linearity. Our DFT computations reveal that all the reactions follow the direct N₂ extrusion mechanism and the same pathway leading to final products. However, the rate-determining step for the formation of **2a-f** switches from the formation of the rhenium-azide adduct to extrusion of N₂ from this adduct. The two barriers are sufficiently close in energy and they have opposite behavior with respect to their order for a series of substituents, so that the change in substituent causes a change in the rate-determining step.

The third system is about a series of conversions from vanadium azide compounds ((tpa^{Mes})V[η¹-N₃(*p*-C₆H₄R)]); tpa^{Mes} = tris(pyrrolylmesityl)amine, **2**) to vanadium imido compounds. Besides vanadium imides, small amount of azoarene was produced in the thermolysis of the vanadium azide compounds. Computational results suggest that the most plausible pathway is PATH1. In this pathway, the experimentally isolated compound, **2a_sing**, firstly decomposes into a triplet vanadium-N₂ and a triplet nitrene. Then the N₂ ligand is replaced by nitrene to form a very stable vanadium imido product. Both experiments and computations found lower barriers for the end-on vanadium azide compound **2a_sing** to release nitrene radical than for the free azide to do so. The calculations predict the reasons as: 1) the N_α-N_β bond in **2a_sing** is weaker than that in the free azide; 2) The breaking of the N_α-N_β in **2a_sing** directly gives rise to two fragments both in their ground state while the thermolysis of free azide experiences

intersystem crossing, which may slow down the yield of triplet nitrene. The reaction barriers of other possible pathways were calculated to be significantly high essentially due to the steric repulsion from the supporting ligand.

REFERENCES

1. (a) Hartwig, J., *Organotransition Metal Chemistry: From Bonding to Catalysis, First Edition* University Science books, Mill Valley, CA, **2009**. (b) Hagen, J. *Industrial Catalysis A Practical Approach, Second Edition* Wiley VCH, Weinheim, Germany, **2006**.
2. Crabtree, R., *The Organometallic Chemistry of the Transition Metals, Fifth Edition*. John Wiley & Sons, Inc., Hoboken, NJ, **2009**.
3. (a) Pauling, L., *The Nature of the Chemical Bond and the Structure of Molecules and Crystals: An Introduction to Modern Structural Chemistry, Third Edition*, Cornell University Press, Ithaca, NY, **1960**. (b) Shaik, S. S.; Hiberty, P. C. *A Chemist's Guide to Valence Bond Theory, First Edition*, John Wiley & Sons, Inc., Hoboken, NJ, **2007**.
4. Albright, T. A.; Burdett, J. K.; Whangbo, M. *Orbital Interactions in Chemistry, First Edition*, Wiley-Interscience, New York, NY, **1985**.
5. Bertrand, G. *Carbene Chemistry*, Marcel Dekker, New York, NY, **2002**.
6. Winkler, J. R.; Gray, H. B. *Struct. Bond.* **2012**, *142*, 17.
7. O'Halloran, K. P.; Zhao, C.; Ando, N. S.; Schultz, A. J.; Koetzle, T. F.; Piccoli, P. M. B.; Hedman, B.; Hodgson, K. O.; Bobyr, E.; Kirk, M. L.; Knottenbelt, S.; Depperman, E. C.; Stein, B.; Anderson, T. M.; Cao, R.; Geletii, Y. V.; Hardcastle, K. I.; Musaev, D. G.; Neiwert, W. A.; Fang, X.; Morokuma, K.; Wu, S.; Kögerler, P.; Hill, C. L. *Inorg. Chem.* **2012**, *51*, 7025.
8. Nugent, W. A.; Haymore, B. L. *Coord. Chem. Rev.* **1980**, *31*, 123.
9. Parkin, G. In *Progress in Inorganic Chemistry, Vol. 47*; Karlin, K. D., Ed.; Wiley-Interscience, New York, NY, **1998**.
10. Aktaş, H.; Slootweg, J. C.; Lammertsma, K. *Angew. Chem., Int. Ed.* **2010**, *49*, 2102.
11. Braunschweig, H.; Dewhurst, R. D.; Gessner, V. H. *Chem. Soc. Rev.* **2013**, *42*, 3197.
12. Levine, I. N. *Quantum Chemistry, Sixth Edition*, Prentice Hall, Upper Saddle River, NJ, **2008**.

13. Jensen, F. *Introduction to Computational Chemistry Second Edition*. John Wiley & Sons, Ltd. Chichester, England, **2007**.
14. Szabo, A.; Ostlund, N. S. *Modern Quantum Chemistry*. Dover Publishing, Mineola, NY, **1996**.
15. Cramer, C. J. *Essentials of Computational Chemistry*. Chichester: John Wiley & Sons, Ltd., Chichester, England, **2002**.
16. Koch, W.; Holthausen, M. C. *A Chemist's Guide to Density Functional Theory, 2nd Edition* Wiley-VCH, Weinheim, Germany, **2001**.
17. Hohenberg, P.; Kohn, W. *Physical Review* **1964**, *136*, B864.
18. Kohn, W.; Sham, L. J. *Physical Review* **1965**, *140*, A1133.
19. Slater, J. C. *The Self-Consistent Field for Molecular and Solids, Quantum Theory of Molecular and Solids, Vol. 4*, McGraw-Hill, New York, NY, **1974**.
20. Vosko, S. H.; Wilk, L.; Nusair, M. *Can. J. Phys.* **1980**, *58*, 1200.
21. Becke, A. D. *Phys. Rev. A* **1988**, *38*, 3098.
22. (a) Lee, C.; Yang, W.; Parr, R. G. *Physical Review B* **1988**, *37*, 785. (b) Miehlich, B.; Savin, A.; Stoll, H.; Preuss, H. *Chem. Phys. Lett.* **1989**, *157*, 200.
23. Tao, J.; Perdew, J. P.; Staroverov, V. N.; Scuseria, G. E. *Phys. Rev. Lett.* **2003**, *91*, 146401.
24. Zhao, Y.; Truhlar, D. G. *J. Chem. Phys.* **2006**, *125*.
25. Becke, A. D. *J. Chem. Phys.* **1993**, *98*, 5648.
26. Perdew, J. P. *Physical Review B* **1986**, *33*, 8822.
27. Handy, N. C.; Cohen, A. J. *Mol. Phys.* **2001**, *99*, 403.
28. Perdew, J. P. *Electronic Structure of Solids 91*, Ziesche, E. P. and Eschrig, H. Akademie Verlag, Berlin, Germany, **1991**.
29. Zhao, Y.; Truhlar, D. *Theor. Chem. Acc.* **2008**, *120*, 215.
30. Grimme, S. *J. Comput. Chem.* **2006**, *27*, 1787.
31. Grimme, S.; Ehrlich, S.; Goerigk, L. *J. Comput. Chem.* **2011**, *32*, 1456.

32. Boys, S. F. *Reviews of Modern Physics* **1960**, *32*, 296.
33. Edmiston, C.; Ruedenberg, K. *J. Chem. Phys.*, **1965**, *43*, S97.
34. Pipek, J.; Mezey, P. G. *J. Chem. Phys.*, **1989**, *90*, 4916.
35. (a) Weinhold, F.; Landis, C. R. *Valency and Bonding: A Natural Bond Orbital Donor-Acceptor Perspective*, Cambridge University Press, New York, NY, **2005**
(b) Weinhold, F.; Landis, C. R. *Discovering Chemistry With Natural Bond Orbitals*, Wiley, Hoboken, NJ, **2012**.
36. (a) Mitoraj, M. P.; Michalak, A.; Ziegler, T. *J. Chem. Theory Comput.* **2009**, *5*, 962; (b) Michalak, A.; Mitoraj, M.; Ziegler, T. *J. Phys. Chem. A* **2008**, *112*, 1933; (c) Mitoraj, M.; Michalak, A. *Journal of Molecular Modeling* **2007**, *13*, 347; (d) Ziegler, T.; Rauk, A. *Theor. Chim. Acta* **1977**, *46*, 1.
37. Hopffgarten, M. v.; Frenking, G. *Wiley Interdisciplinary Reviews: Computational Molecular Science* **2012**, *2*, 43.
38. (a) Bunz, U. H. F. *Acc. Chem. Res.* **2001**, *34*, 998; (b) Schrock, R. R. *Chem. Rev.* **2002**, *102*, 145; (c) Furstner, A.; Davies, P. W. *Chem. Commun.* **2005**, 2307; (d) Schrock, R. R.; Czekelius, C. *Adv. Synth. Catal.* **2007**, *349*, 55; (e) Zhang, W.; Moore, J. S. *Adv. Synth. Catal.* **2007**, *349*, 93; (f) Wu, X.; Tamm, M. *Beilstein J. Org. Chem.* **2011**, *7*, 82; (g) Heppekausen, J.; Stade, R.; Kondoh, A.; Seidel, G.; Goddard, R.; Furstner, A. *Chem. Eur. J.* **2012**, *18*, 10281.
39. (a) Jutzi, P. *Angew. Chem., Int. Ed. Engl.* **1975**, *14*, 232; (b) Gusel'nikov, L. E.; Nametkin, N. S. *Chem. Rev.* **1979**, *79*, 529; (c) West, R. *Angew. Chem., Int. Ed. Engl.* **1987**, *26*, 1201; (d) Power, P. P. *Chem. Rev.* **1999**, *99*, 3463; (e) Waterman, R.; Hayes, P. G.; Tilley, T. D. *Acc. Chem. Res.* **2007**, *40*, 712.
40. (a) Simons, R. S.; Power, P. P. *J. Am. Chem. Soc.* **1996**, *118*, 11966; (b) Pu, L.; Twamley, B.; Haubrich, S. T.; Olmstead, M. M.; Mork, B. V.; Simons, R. S.; Power, P. P. *J. Am. Chem. Soc.* **2000**, *122*, 650.
41. (a) Filippou, A. C.; Philippopoulos, A. I.; Portius, P.; Neumann, D. U. *Angew. Chem., Int. Ed.* **2000**, *39*, 2778; (b) Filippou, A. C.; Portius, P.; Philippopoulos, A. I. *Organometallics* **2002**, *21*, 653; (c) Filippou, A. C.; Schnakenburg, G.; Philippopoulos, A. I.; Weidemann, N. *Angew. Chem., Int. Ed.* **2005**, *44*, 5979; (d) Filippou, A. C.; Weidemann, N.; Philippopoulos, A. I.; Schnakenburg, G. *Angew. Chem., Int. Ed.* **2006**, *45*, 5987.

42. (a) Filippou, A. C.; Philippopoulos, A. I.; Schnakenburg, G. *Organometallics* **2003**, *22*, 3339; (b) Filippou, A. C.; Portius, P.; Philippopoulos, A. I.; Rohde, H. *Angew. Chem., Int. Ed.* **2003**, *42*, 445.
43. Mork, B. V.; Tilley, T. D. *Angew. Chem., Int. Ed.* **2003**, *42*, 357.
44. Filippou, A. C.; Chernov, O.; Stumpf, K. W.; Schnakenburg, G. *Angew. Chem., Int. Ed.* **2010**, *49*, 3296.
45. (a) Pandey, K. K.; Lein, M.; Frenking, G. *J. Am. Chem. Soc.* **2003**, *125*, 1660; (b) Filippou, A. C.; Rohde, H.; Schnakenburg, G. *Angew. Chem., Int. Ed.* **2004**, *43*, 2243; (c) Pandey, K. K.; Lledós, A. *Inorg. Chem.* **2009**, *48*, 2748; (d) Pandey, K. K.; Patidar, P.; Power, P. P. *Inorg. Chem.* **2011**, *50*, 7080.
46. Hays, P. G.; Xu, Z.; Beddie, C.; Keith, J. M.; Hall, M. B.; Tilley, T. D., *J. Am. Chem. Soc.*, **2013**, *135*, 11780.
47. Hayes, P. G.; Beddie, C.; Hall, M. B.; Waterman, R.; Tilley, T. D. *J. Am. Chem. Soc.* **2006**, *128*, 428.
48. Frisch, M. J.; Trucks, G. W.; Schlegel, H. B.; Scuseria, G. E.; Robb, M. A.; Cheeseman, J. R.; Scalmani, G.; Barone, V.; Mennucci, B.; Petersson, G. A.; Nakatsuji, H.; Caricato, M.; Li, X.; Hratchian, H. P.; Izmaylov, A. F.; Bloino, J.; Zheng, G.; Sonnenberg, J. L.; Hada, M.; Ehara, M.; Toyota, K.; Fukuda, R.; Hasegawa, J.; Ishida, M.; Nakajima, T.; Honda, Y.; Kitao, O.; Nakai, H.; Vreven, T.; Montgomery, J. A., Jr.; Peralta, J. E.; Ogliaro, F.; Bearpark, M.; Heyd, J. J.; Brothers, E.; Kudin, K. N.; Staroverov, V. N.; Kobayashi, R.; Normand, J.; Raghavachari, K.; Rendell, A.; Burant, J. C.; Iyengar, S. S.; Tomasi, J.; Cossi, M.; Rega, N.; Millam, N. J.; Klene, M.; Knox, J. E.; Cross, J. B.; Bakken, V.; Adamo, C.; Jaramillo, J.; Gomperts, R.; Stratmann, R. E.; Yazyev, O.; Austin, A. J.; Cammi, R.; Pomelli, C.; Ochterski, J. W.; Martin, R. L.; Morokuma, K.; Zakrzewski, V. G.; Voth, G. A.; Salvador, P.; Dannenberg, J. J.; Dapprich, S.; Daniels, A. D.; Farkas, Ö.; Foresman, J. B.; Ortiz, J. V.; Cioslowski, J.; Fox, D. J., Gaussian 09, Revision **D.01**, Gaussian, Inc., Wallingford CT, **2009**.
49. Glendening, E. D.; Badenhop, J. K.; Reed, A. E.; Carpenter, J. E.; Bohmann, J. A.; Morales, C. M. and Weinhold, F., NBO 5.9 (Theoretical Chemistry Institute, University of Wisconsin, Madison, WI, 2011); <http://www.chem.wisc.edu/~nbo5>
50. a) Guerra, C. F.; Snijders, J. G.; te Velde, G.; Baerends, E. J. *Theor. Chem. Acc.* **1998**, *99*, 391. b) te Velde, G.; Bickelhaupt, F. M.; Baerends, E. J.; Guerra, C. F.; van Gisbergen, S. J. A.; Snijders, J. G.; Ziegler, T. *J. Comput. Chem.* **2001**, *22*, 931. c) Baerends, E.J.; Ziegler, T.; *et al* ADF2012, SCM, Theoretical Chemistry, Vrije Universiteit, Amsterdam, The Netherlands, <http://www.scm.com>

51. Tao, J.; Perdew, J. P.; Staroverov, V. N.; Scuseria, G. E. *Phys. Rev. Lett.* **2003**, *91*, 146401.
52. Andrae, D.; Häußermann, U.; Dolg, M.; Stoll, H.; Preuß, H. *Theor. Chim. Acta* **1990**, *77*, 123.
53. a) Krishnan, R.; Binkley, J. S.; Seeger, R.; Pople, J. A. *J. Chem. Phys.* **1980**, *72*, 650; (b) McLean, A. D.; Chandler, G. S. *J. Chem. Phys.* **1980**, *72*, 5639.
54. (a) Hariharan, P. C.; Pople, J. A. *Theoretical Chemistry Accounts: Theory, Computation, and Modeling (Theoretica Chimica Acta)* **1973**, *28*, 213; (b) Francel, M. M.; Pietro, W. J.; Hehre, W. J.; Binkley, J. S.; Gordon, M. S.; DeFrees, D. J.; Pople, J. A. *J. Chem. Phys.* **1982**, *77*, 3654.
55. Figgen, D.; Peterson, K. A.; Dolg, M.; Stoll, H. *J. Chem. Phys.* **2009**, *130*, 164108.
56. (a) Clark, T.; Chandrasekhar, J.; Spitznagel, G. W.; Schleyer, P. V. R. *J. Comput. Chem.* **1983**, *4*, 294; (b) Frisch, M. J.; Pople, J. A.; Binkley, J. S. *J. Chem. Phys.* **1984**, *80*, 3265.
57. a) Grimme, S.; Antony, J.; Ehrlich, S.; Krieg, H. *J. Chem. Phys.* **2010**, *132*. b) BJ-damping scheme is included in the dispersion correction. See ref. Grimme, S.; Ehrlich, S.; Goerigk, L. *J. Comput. Chem.* **2011**, *32*, 1456.
58. (a) Miertuš, S.; Scrocco, E.; Tomasi, J. *Chem. Phys.* **1981**, *55*, 117; (b) Miertuš, S.; Tomasi, J. *Chem. Phys.* **1982**, *65*, 239; (c) Cossi, M.; Barone, V.; Cammi, R.; Tomasi, J. *Chem. Phys. Lett.* **1996**, *255*, 327; (d) Tomasi, J.; Mennucci, B.; Cammi, R. *Chem. Rev.* **2005**, *105*, 2999.
59. (a) Gauss, J. *Chem. Phys. Lett.* **1992**, *191*, 614; (b) Gauss, J. *J. Chem. Phys.* **1993**, *99*, 3629; (c) Cheeseman, J. R.; Trucks, G. W.; Keith, T. A.; Frisch, M. J. *J. Chem. Phys.* **1996**, *104*, 5497. (e) Gauss, J., *Accurate calculation of NMR chemical shifts*. Wiley, Weinheim, Germany, **1995**.
60. (a) Perdew, J. P.; Burke, K.; Ernzerhof, M. *Phys. Rev. Lett.* **1996**, *77*, 3865; (b) Perdew, J. P.; Burke, K.; Ernzerhof, M. *Phys. Rev. Lett.* **1997**, *78*, 1396.
61. (a) Fukui, K. *Acc. Chem. Res.* **1981**, *14*, 363. (b) Hratchian, H. P. and Schlegel, H. B., in *Theory and Applications of Computational Chemistry: The First 40 Years*, Ed. Dykstra, C. E., Frenking, G., Kim, K. S. and Scuseria, G. (Elsevier, Amsterdam, **2005**) 195-249. (c) Hratchian, H. P.; Schlegel, H. B. *J. Chem. Theory Comput.* **2004**, *1*, 61. (d) Hratchian, H. P.; Schlegel, H. B. *J. Chem. Phys.* **2004**, *120*, 9918.

62. Brase, S.; Gil, C.; Knepper, K.; Zimmermann, V. *Angew. Chem. Int. Ed.* **2005**, *44*, 5188.
63. (a) Cenini, S.; Gallo, E.; Caselli, A.; Ragaini, F.; Fantauzzi, S.; Piangiolino, C. *Coord. Chem. Rev.* **2006**, *250*, 1234. (b) Omura, K.; Murakami, M.; Uchida, T.; Irie, R.; Katsuki, T. *Chem. Lett.* **2003**, *32*, 354. (c) Shen, M. H.; Leslie, B. E.; Driver, T. G. *Angew. Chem. Int. Ed.* **2008**, *47*, 5056.
64. (a) Fantauzzi, S.; Gallo, E.; Caselli, A.; Ragaini, F.; Macchi, P.; Casati, N.; Cenini, S. *Organometallics* **2005**, *24*, 4710. (b) Gao, G. Y.; Jones, J. E.; Vyas, R.; Harden, J. D.; Zhang, X. P. *J. Org. Chem.* **2006**, *71*, 6655. (c) Han, H.; Park, S. B.; Kim, S. K.; Chang, S. B. *J. Org. Chem.* **2008**, *73*, 2862. (d) Jones, J. E.; Ruppel, J. V.; Gao, G. Y.; Moore, T. M.; Zhang, X. P. *J. Org. Chem.* **2008**, *73*, 7260. (e) Li, J.; Fu, Y.; Guo, Q. X. *Tetrahedron* **2008**, *64*, 11167.
65. Winnewisser, M.; Cook, R. L. *J. Chem. Phys.* **1964**, *41*, 999.
66. (a) Proulx, G.; Bergman, R. G. *J. Am. Chem. Soc.* **1995**, *117*, 6382. (b) Fickes, M. G.; Davis, W. M.; Cummins, C. C. *J. Am. Chem. Soc.* **1995**, *117*, 6384. (c) Guillemot, G.; Solari, E.; Floriani, C.; Rizzoli, C. *Organometallics* **2001**, *20*, 607. (d) Hanna, T. A.; Baranger, A. M.; Bergman, R. G. *Angew. Chem. Int. Ed.* **1996**, *35*, 653. (e) Albertin, G.; Antoniutti, S.; Bacchi, A.; Celebrin, A.; Pelizzi, G.; Zanardo, G. *Dalton Trans.* **2007**, 661. (f) Barz, M.; Herdtweck, E.; Thiel, W. R. *Angew. Chem. Int. Ed.* **1998**, *37*, 2262. (g) Albertin, G.; Antoniutti, S.; Baldan, D.; Castro, J.; Garcia-Fontan, S. *Inorg. Chem.* **2008**, *47*, 742.
67. Kwart, H.; Kahn, A. A. *J. Am. Chem. Soc.* **1967**, *89*, 1950.
68. Margosian, D.; Kovacic, P. *J. Org. Chem.* **1981**, *46*, 877.
69. (a) Gambarotta, S.; Chiesivilla, A.; Guastini, C. *J. Organometal. Chem.* **1984**, *270*, C49. (b) Osborne, J. H.; Trogler, W. C. *Inorg. Chem.* **1985**, *24*, 3098. (c) Osborne, J. H.; Rheingold, A. L.; Trogler, W. C. *J. Am. Chem. Soc.* **1985**, *107*, 7945.
70. (a) Himo, F.; Lovell, T.; Hilgraf, R.; Rostovtsev, V. V.; Noodleman, L.; Sharpless, K. B.; Fokin, V. V. *J. Am. Chem. Soc.* **2005**, *127*, 210. (b) Bock, V. D.; Hiemstra, H.; van Maarseveen, J. H. *Eur. J. Org. Chem.* **2006**, 51.
71. Proulx, G.; Bergman, R. G. *Organometallics* **1996**, *15*, 684.
72. (a) Cundari, T. R.; Morello, G. R. *J. Org. Chem.* **2009**, *74*, 5711. (b) Waterman, R.; Hillhouse, G.L. *J. Am. Chem. Soc.* **2008**, *130*, 12628.

73. Ison, E. A.; Cessarich, J. E.; Travia, N. E.; Fanwick, P. E.; Abu-Omar, M. M. *J. Am. Chem. Soc.* **2007**, *129*, 1167.
74. Wu, H.; Hall, M. B. *J. Am. Chem. Soc.* **2008**, *130*, 16452.
75. Travia, N. E.; Xu, Z.; Keith, J. M.; Ison, E. A.; Fanwick, P. E.; Hall, M. B.; Abu-Omar, M. M., *Inorg. Chem.* **2011**, *50*, 10505.
76. Hammett, L. P. *J. Am. Chem. Soc.* **1937**, *59*, 96.
77. (a) Stephens, P. J.; Devlin, F. J.; Chabalowski, C. F.; Frisch, M. *J. Phys. Chem.* **1994**, *98*, 11623. (b) Becke, A. D. *J. Chem. Phys.* **1993**, *98*, 5648. (c) Lee, C.; Yang, W.; Parr, R. G. *Phys. Rev. B* **1988**, *37*, 785.
78. Peng, C.; Ayala, P. Y.; Schlegel, H. B.; Frisch, M. J. *J. Comput. Chem.* **1996**, *17*, 49.
79. Hay, P. J.; Wadt, W. R. *J. Chem. Phys.* **1985**, *82*, 299.
80. Couty, M.; Hall, M. B. *J. Comp. Chem.* **1996**, *17*, 1359.
81. Ehlers, A. W.; Böhme, M.; Dapprich, S.; Gobbi, A.; Höllwarth, A.; Jonas, V.; Köhler, K. F.; Stegmann, R.; Veldkamp, A.; Frenking, G. *Chem. Phys. Lett.* **1993**, *208*, 111.
82. (a) Petersson, G. A.; Al-Laham, M. A. *J. Chem. Phys.* **1991**, *94*, 6081. (b) Petersson, G. A.; Bennett, A.; Tensfeldt, T. G.; Al-Laham, M. A.; Shirley, W. A.; Mantzaris, J. *J. Chem. Phys.* **1988**, *89*, 2193. (c) Foresman, J. B. and Frisch, M. *Exploring Chemistry with Electronic Structure Methods*, 2nd Ed. Gaussian, Inc, Pittsburgh, PA **1996**, p. 110. The 6-31G(d') basis set has the d polarization functions for C, N, O, and F taken from the 6-311G basis set, instead of the original arbitrarily assigned value of 0.8 used in the 6-31G(d) basis set.
83. Marenich, A. V.; Cramer, C. J.; Truhlar, D. G. *J. Phys. Chem. B* **2009**, *113*, 6378.
84. (a) Manson, J.; Webster, C. E.; Hall, M. B. JIMP2, Version 0.091, a free program for visualizing and manipulating molecules; Texas A&M University: College Station, TX, **2006**. (b) Hall, M. B.; Fenske, R. F.; *Inorg. Chem.* **1972**, *11*, 768.
85. (a) Espenson, J. H. *Chem. Commun.* **1999**, 479. (b) Owens, G. S.; Aries, J.; Abu-Omar, M. M. *Catal. Today* **2000**, *55*, 317. (c) Romao, C. C.; Kuhn, F. E.; Herrmann, W. A. *Chem. Rev.* **1997**, *97*, 3197. (d) Nugent, W. A. M., J. M. *Metal-Ligand Multiple Bonds*; Wiley: New York, NY **1988**. (e) Wigley, D. E. *Prog. Inorg. Chem.* **1994**, *42*, 239.

86. (a) Borden, W. T.; Gritsan, N. P.; Hadad, C. M.; Karney, W. L.; Kemnitz, C. R.; Platz, M. S. *Acc. Chem. Res.* **2000**, *33*, 765. (b) Carl Lineberger, W.; Thatcher Borden, W. *Phys. Chem. Chem. Phys.* **2011**, *13*, 11792.
87. (a) Gritsan, N. P.; Platz, M. S., *Chem. Rev.* **2006**, *106*, 3844. (b) Travers, M. J.; Cowles, D. C.; Clifford, E. P.; Ellison, G. B. *J. Am. Chem. Soc.* **1992**, *114*, 8699. (c) McDonald, R. N.; Davidson, S. J. *J. Am. Chem. Soc.* **1993**, *115*, 10857.
88. Mankad, N. P.; Müller, P.; Peters, J. C. *J. Am. Chem. Soc.* **2010**, *132*, 4083.
89. Takaoka, A.; Moret, M.-E.; Peters, J. C. *J. Am. Chem. Soc.* **2012**, *134*, 6695.
90. Harman, W. H.; Lichterman, M. F.; Piro, N. A.; Chang, C. J. *Inorg. Chem.* **2012**, *51*, 10037.
91. Dolg, M.; Wedig, U.; Stoll, H.; Preuss, H. *J. Chem. Phys.* **1987**, *86*, 866.
92. Martin, J. M. L.; Sundermann, A. *J. Chem. Phys.* **2001**, *114*, 3408.
93. Harvey, J. N.; Aschi, J. N.; M.; Schwarz, H.; Koch, W. *Theor. Chem. Acc.* **1998**, *99*, 95.
94. (a) Yamaguchi, K.; Jensen, F.; Dorigo, A.; Houk, K. N. *Chem. Phys. Lett.* **1988**, *149*, 537. (b) Soda, T.; Kitagawa, Y.; Onishi, T.; Takano, Y.; Shigeta, Y.; Nagao, H.; Yoshioka, Y.; Yamaguchi, K. *Chem. Phys. Lett.* **2000**, *319*, 223. (c) Ertem, M. Z.; Gagliardi, L.; Cramer, C. J. *Chem. Sci.* **2012**, *3*, 1293.